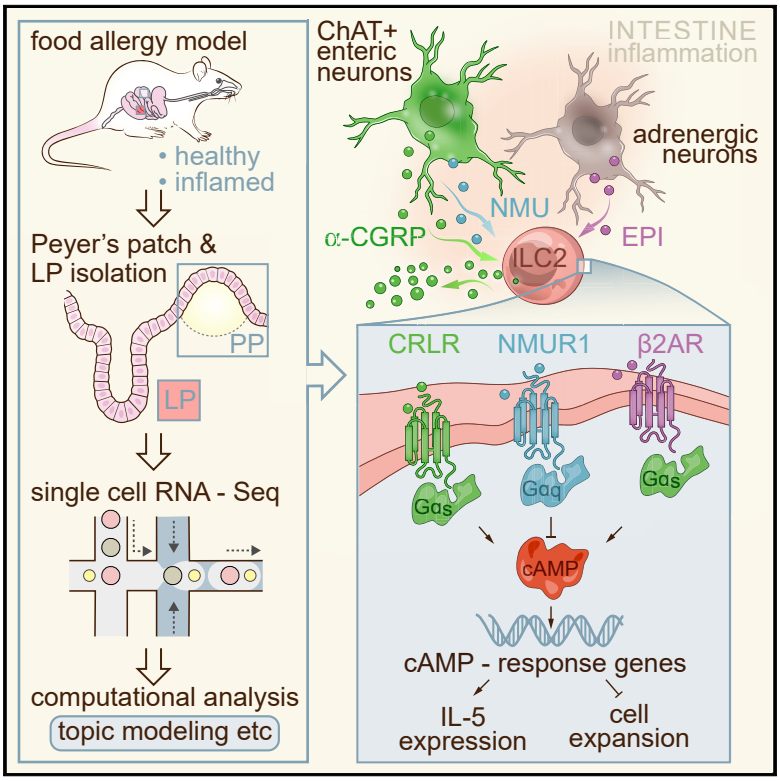
Article

Immunity

Transcriptional Atlas of Intestinal Immune Cells Reveals that Neuropeptide α-CGRP Modulates Group 2 Innate Lymphoid Cell Responses

Graphical Abstract



Highlights

- scRNA-seq reveals intestinal immune cell programs in allergic inflammation
- Intestinal KLRG1$^+$ ILC2s express α-CGRP and its receptors
- α-CGRP regulates type 2 cytokine production of KLRG1$^+$ ILC2s
- α-CGRP maintains KLRG1$^+$ ILC2 homeostasis and the type 2 immune machinery

Authors

Heping Xu, Jiarui Ding, Caroline B.M. Porter, ..., Vijay K. Kuchroo, Aviv Regev, Ramnik J. Xavier

Correspondence

xuheping@westlake.edu.cn (H.X.), aregev@broadinstitute.org (A.R.), xavier@molbio.mgh.harvard.edu (R.J.X.)

In Brief

Allergic inflammation involves the interaction of multiple immune cell types, as well as their crosstalk with other physiological systems, such as neurons. By establishing intestinal immune cell atlas at different states, Xu et al. identify that neuropeptide α-CGRP modulates group 2 innate lymphoid cell responses and the allergic reaction.

Xu et al., 2019, Immunity *51*, 696–708
October 15, 2019 © 2019 Elsevier Inc.
https://doi.org/10.1016/j.immuni.2019.09.004

CellPress

CellPress

Immunity
Article

Transcriptional Atlas of Intestinal Immune Cells Reveals that Neuropeptide α-CGRP Modulates Group 2 Innate Lymphoid Cell Responses

Heping Xu,[1,2,3,11,12,*] Jiarui Ding,[1,11] Caroline B.M. Porter,[1] Antonia Wallrapp,[4] Marcin Tabaka,[1] Sai Ma,[1] Shujie Fu,[2,3] Xuanxuan Guo,[2,3] Samantha J. Riesenfeld,[1] Chienwen Su,[5] Danielle Dionne,[1] Lan T. Nguyen,[1] Ariel Lefkovith,[1] Orr Ashenberg,[1] Patrick R. Burkett,[4] Hai Ning Shi,[5] Orit Rozenblatt-Rosen,[1] Daniel B. Graham,[1,6,7,8] Vijay K. Kuchroo,[1,4] Aviv Regev,[1,9,12,*] and Ramnik J. Xavier[1,6,7,8,10,13,*]

[1]Broad Institute of MIT and Harvard, Cambridge, MA 02142, USA
[2]Key Laboratory of Structural Biology of Zhejiang Province, School of Life Sciences, Westlake University, Hangzhou 310024, Zhejiang Province, China
[3]Laboratory of Systems Immunology, Institute of Basic Medical Sciences, Westlake Institute for Advanced Study, Hangzhou 310024, Zhejiang Province, China
[4]Evergrande Center for Immunologic Diseases, Harvard Medical School and Brigham and Women's Hospital, Boston, MA 02114, USA
[5]Mucosal Immunology and Biology Research Center, Massachusetts General Hospital and Harvard Medical School, Charlestown, MA 02129, USA
[6]Department of Molecular Biology, Massachusetts General Hospital, Harvard Medical School, Boston, MA 02114, USA
[7]Gastrointestinal Unit and Center for the Study of Inflammatory Bowel Disease, Massachusetts General Hospital, Harvard Medical School, Boston, MA 02114, USA
[8]Center for Microbiome Informatics and Therapeutics, Massachusetts Institute of Technology, Cambridge, MA 02114, USA
[9]Howard Hughes Medical Institute and Koch Institute for Integrative Cancer Research, Department of Biology, Massachusetts Institute of Technology, Cambridge, MA 02142, USA
[10]Center for Computational and Integrative Biology, Massachusetts General Hospital, Harvard Medical School, Boston, MA 02114, USA
[11]These authors contributed equally
[12]Senior author
[13]Lead Contact
*Correspondence: xuheping@westlake.edu.cn (H.X.), aregev@broadinstitute.org (A.R.), xavier@molbio.mgh.harvard.edu (R.J.X.)
https://doi.org/10.1016/j.immuni.2019.09.004

SUMMARY

Signaling abnormalities in immune responses in the small intestine can trigger chronic type 2 inflammation involving interaction of multiple immune cell types. To systematically characterize this response, we analyzed 58,067 immune cells from the mouse small intestine by single-cell RNA sequencing (scRNA-seq) at steady state and after induction of a type 2 inflammatory reaction to ovalbumin (OVA). Computational analysis revealed broad shifts in both cell-type composition and cell programs in response to the inflammation, especially in group 2 innate lymphoid cells (ILC2s). Inflammation induced the expression of exon 5 of *Calca*, which encodes the alpha-calcitonin gene-related peptide (α-CGRP), in intestinal KLRG1$^+$ ILC2s. α-CGRP antagonized KLRG1$^+$ ILC2s proliferation but promoted IL-5 expression. Genetic perturbation of α-CGRP increased the proportion of intestinal KLRG1$^+$ ILC2s. Our work highlights a model where α-CGRP-mediated neuronal signaling is critical for suppressing ILC2 expansion and maintaining homeostasis of the type 2 immune machinery.

INTRODUCTION

The immune system in the small intestine is composed of a complex network of innate and adaptive components that sense and respond to antigens from the diet, commensal microbiota, and pathogens. Dysregulated immune reactions often lead to chronic inflammatory responses, including type 2 inflammation (Gieseck et al., 2018; Hammad and Lambrecht, 2015; Pulendran and Artis, 2012), which in turn plays a key underlying role in several unrelenting inflammatory diseases, including food allergy (Locksley, 2010; Tordesillas et al., 2017).

Several hallmarks of type 2 inflammation, including the production of immunoglobulin E (IgE) antibodies and type 2 cytokines, such as interleukin-13 (IL-13) and IL-5, rely on tightly regulated and coordinated immune responses across different cell types, such as T helper 2 (Th2) cells, mast cells, and group 2 innate lymphoid cells (ILC2s). In particular, ILC2s have emerged as key regulators of tissue homeostasis and type 2 inflammation (Artis and Spits, 2015; Kotas and Locksley, 2018) and form the prominent source of type 2 cytokines at the early stages of inflammatory responses (Molofsky et al., 2015; Neill et al., 2010; Price et al., 2010).

While the core transcriptional program of ILC2s maintains their cellular identity and homeostatic type 2 cytokine competence (Ricardo-Gonzalez et al., 2018), their activity in the intestines is shaped by tissue-specific signals, including activation by IL-25 produced by tuft cells (von Moltke et al., 2016) and suppression

by micronutrients (Spencer et al., 2014). Recent studies show that neuronal signals orchestrate intestinal ILC2 activity. For example, the neuropeptide neuromedin U (NMU), secreted from cholinergic neurons, amplifies ILC2 activation and proliferation, thereby promoting type 2 inflammation (Cardoso et al., 2017; Klose et al., 2017; Wallrapp et al., 2017). In contrast, β-adrenergic-receptor-mediated signaling suppresses ILC2 activity in intestinal infection models (Moriyama et al., 2018).

Despite these substantial advances, we still have an incomplete understanding of the cellular participants in type 2 inflammation, the mechanisms that maintain homeostasis, and which additional cell types besides immune cells may participate in this cellular circuit in the small intestine. Single-cell RNA sequencing (scRNA-seq) can dissect cellular diversity on a large scale (Tanay and Regev, 2017; Wagner et al., 2016) and identify cell states of individual cell types in response to different stimuli (Bielecki et al., 2018; Haber et al., 2017).

Here, we combine scRNA-seq with physiological and genetic perturbations to dissect the cellular circuit of type 2 intestinal inflammation. To uncover key responding cellular components, we profiled individual immune cells from the lamina propria (LP) and Peyer's patches (PPs) in homeostasis and in an intestinal type 2 inflammatory model. Computational analysis showed that both cell compositions and cell programs shifted in response to inflammation, and highlighted the prominent induction of alpha-calcitonin gene-related peptide (α-CGRP) transcription in ILC2s. In inflammatory conditions, α-CGRP suppressed activation of ILC2s, but induced IL-5 expression. α-CGRP stimulation *in vitro* increased the intracellular concentration of cyclic AMP (cAMP), induced the expression of a cAMP-response gene module and suppressed cell proliferation. At homeostasis *in vivo*, choline acetyltransferase ($ChAT^+$) enteric neurons were the predominant source of α-CGRP and constitutively interacted with ILC2s. Genetic perturbation of α-CGRP increased the proportion of intestinal $KLRG1^+$ ILC2s and the number of tuft cells. Our study reveals a neuro-immune cellular circuit that modulates type 2 inflammation, highlighting critical functions of α-CGRP-mediated neuronal signaling in maintaining homeostasis of ILC2s and the type 2 immune machinery.

RESULTS

A Mouse Immune Cell Atlas of the Small Intestine Provides a Reference Map of Homeostatic and Type 2 Inflammatory Conditions

To comprehensively characterize immune cells in the small intestine, we generated scRNA-seq profiles for 58,067 immune cells collected from LP and PP regions at steady state and after induction of a type 2 inflammatory reaction to ovalbumin (OVA) (Brandt et al., 2003; Figures 1A and S1A). To ensure sufficient representation of rare cell types, we combined two experimental normalization strategies (using flow sorting to remove either a portion of IgD^+ naive B cells—the most abundant cell type in PPs—or all $CD19^+$ B and $CD3^+$ T cells) (Figure S1B; STAR Methods) with profiling of a sufficiently large number of cells (probability >0.99 in recovering at least 15 cells from each of an expected 30 clusters, the rarest estimated at 0.1%; STAR Methods) by massively parallel scRNA-seq (Haber et al., 2017; STAR Methods). After combining cells from both normalization processes, we obtained 36,797 and 21,270 high-quality cells passing initial filtering (STAR Methods) from PP and LP regions, respectively.

Overall, we annotated 27 cell subsets across the two compartments, spanning T cells, B cells, ILCs, dendritic cells (DCs), myeloid cells, and stromal cells, in frequencies ranging from 0.07% to 14%. We corrected experimental batch effects via a robust reference-projection approach (STAR Methods) and visualized the data with scvis (Ding et al., 2018), a deep generative model-based method for modeling and visualizing scRNA-seq data (Figures 1B and S1C; STAR Methods). Our batch correction approach had equal or better concordance and mixing compared to three recently published methods (LIGER, Welch et al., 2019; Harmony, Korsunsky et al., 2018; and scVI, Lopez et al., 2018; Figures S1D and S1E; STAR Methods). Next, we elucidated identities of similar cell types based on genes that were differentially expressed between the cells in each cluster and the remaining cells (Table S1; STAR Methods), as well as between pairs of clusters (Table S2). We excluded from downstream analysis clusters mostly consisting of contaminants from epithelium, likely doublets, cells with a small number of unique molecular identifiers (UMIs) (Figure S1F), and cells lacking distinct markers (Figure S1G; STAR Methods). Altogether, we retained 27 clusters spanning 85% of the cells and each associated with distinct marker genes (Figures S1G and S1H; STAR Methods).

Importantly, known distinct cell types with highly similar expression profiles were correctly distinguished by our analysis. For example, $NKp46^+$ ILC3s and $CCR6^+$ lymphoid tissue inducer (LTi) cells were recovered as separate clusters, even though they both require RORγt-controlled expression programs for their fate determination (Robinette et al., 2015). Nevertheless, LTi cells were distinguished by significantly higher expression of major histocompatibility complex (MHC) class II antigen presentation modules (Figure S1I; $p < 0.05$, likelihood ratio test), whose expression on ILCs has been shown to regulate intestinal homeostasis (Hepworth et al., 2013).

The atlas highlighted expected differences in cellular composition between the LP and PP regions in the homeostatic state (Figures 1C, S1J, and S1K). We used a negative binomial regression model to account for cell counts from individual mice at the steady state (PBS, 6 PP and 4 LP) to address mouse-to-mouse differences in overall cell numbers that can impact the reliability of cell proportion estimates (Haber et al., 2017; STAR Methods). For example, resting and IgD^-GL7^+ germinal center (GC) B cells were exclusively found in PPs (Figure S1K). Conversely, although $CD138^+$ antibody-producing plasma cells differentiate from GC B cells, they were predominantly found in LP samples (Figure S1K) and confirmed in LP regions *in situ* (Figure S1L), highlighting their potential requirement for antibody secretion adjacent to microbes and other antigens in the intestinal mucosa. In another example, LTi cells were significantly enriched ($p = 4.5 \times 10^{-4}$, Wald test) in PP versus LP regions (Figure 1C), which we confirmed by flow cytometry (Figure 1D). The LTi cell distribution is consistent with their critical function in supporting lymphoid tissue development. ILC1s and natural killer (NK) cells were also significantly enriched in PP regions (Figure 1C; $p = 2.5 \times 10^{-9}$ and $p = 7.9 \times 10^{-24}$, respectively, Wald test), suggesting they have unique functions in PPs. Indeed, NK cells suppress affinity maturation of GC B cells (Rydyznski et al., 2018), which probably requires their localization in B cell follicles.

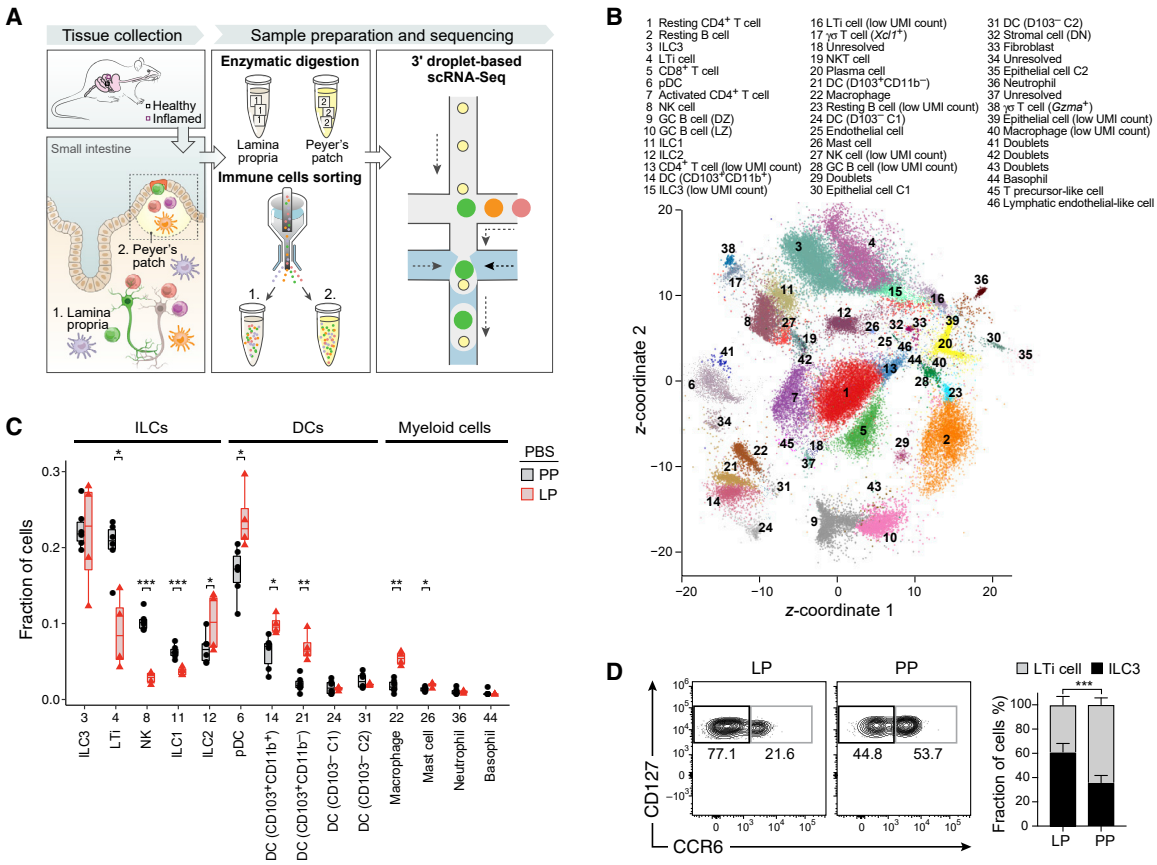


Figure 1. A Single-Cell Expression Atlas of Intestinal Immune Cells

(A) Experimental overview.

(B) Cell subsets in the intestinal immune cell atlas. scvis-learned two-dimensional (2D) representation of cell profiles (dots) from both PP and LP regions, colored and numbered by cluster membership. Clusters are rank ordered by size. DZ, dark zone; LZ, light zone; DN, double negative; C1, cluster 1; C2, cluster 2.

(C) Tissue distribution of non-T and non-B immune cells in homeostasis. Proportion (y axis) of each cell type in LP (red) and PP (black) regions of mice treated with PBS only. Points represent independent mice; boxplots show medians and interquartile ranges (IQRs). Whiskers show the lowest datum within 1.5 IQR of the lower quartile and the highest datum within 1.5 IQR of the upper quartile. *$p < 5 \times 10^{-2}$, **$p < 3 \times 10^{-8}$, and ***$p < 3 \times 10^{-9}$, Wald test.

(D) LTi cells are enriched in PP regions. Shown is flow cytometry analysis gated on $CD45^+Lin^-CD90.2^+IL7R^+ROR\gamma t^+$ cells. Data represent mean ± SEM; ***$p < 0.001$, Fisher's exact test.

Data are from seven (B), three (C), or two (D) independent experiments.

See also Figure S1 and Tables S1 and S2.

We further performed similar analyses to assess cell composition changes between the PP and LP regions using all data (Figure S1J), with the negative binomial regression model with both treatment (OVA or PBS) and location (PP or LP) as covariates. Generally, the results (Figure S1M) were consistent with the results in Figure 1C, with some minor exceptions; cluster 6 (plasmacytoid DCs [pDCs]) was not significantly different between regions, but cluster 24 ($CD103^-$ DCs) was significant. Thus, our comprehensive scRNA-seq dataset provides a reference map of immune cells in the small intestine, capturing rare immune cell types and their diversity across anatomical regions.

Increase in ILC2 Proportions and Changes in Their Expression Programs Are Prominent Features of OVA-Induced Type 2 Inflammation

Cell composition was remodeled in type 2 inflammation (Figures S1J, 2A, and 2B), when comparing inflammatory (OVA) and homeostatic (PBS) states, controlled for anatomical location by a negative binomial regression model when considering cells from all locations together, or when analyzing LP and PP data separately (Figure 2B; STAR Methods), highlighting both known and unique responses. In the combined analysis, mast cell expansion, a well-established feature of allergic reactions (Brandt et al., 2003), was observed in OVA-treated mice ($p = 4.9 \times 10^{-18}$, Wald test; Figure 2B) and validated by flow cytometry (Figure S2A). There was also an increase in ILC2 frequency in mice with type 2 immune reactions to OVA (Figure 2B; $p = 1.5 \times 10^{-2}$, Wald test), which we validated by flow cytometry (Figure S2B), highlighting their importance in this allergic inflammatory model (Burton et al., 2018). Macrophage and neutrophil frequencies also increased significantly in OVA-treated mice ($p = 2.6 \times 10^{-5}$ and $p = 9.5 \times 10^{-4}$, respectively, Wald test), reflecting immune cell infiltration. $CD11b^+CD103^+$ DCs, one of four different populations of DCs in the intestine (Mowat and Agace,

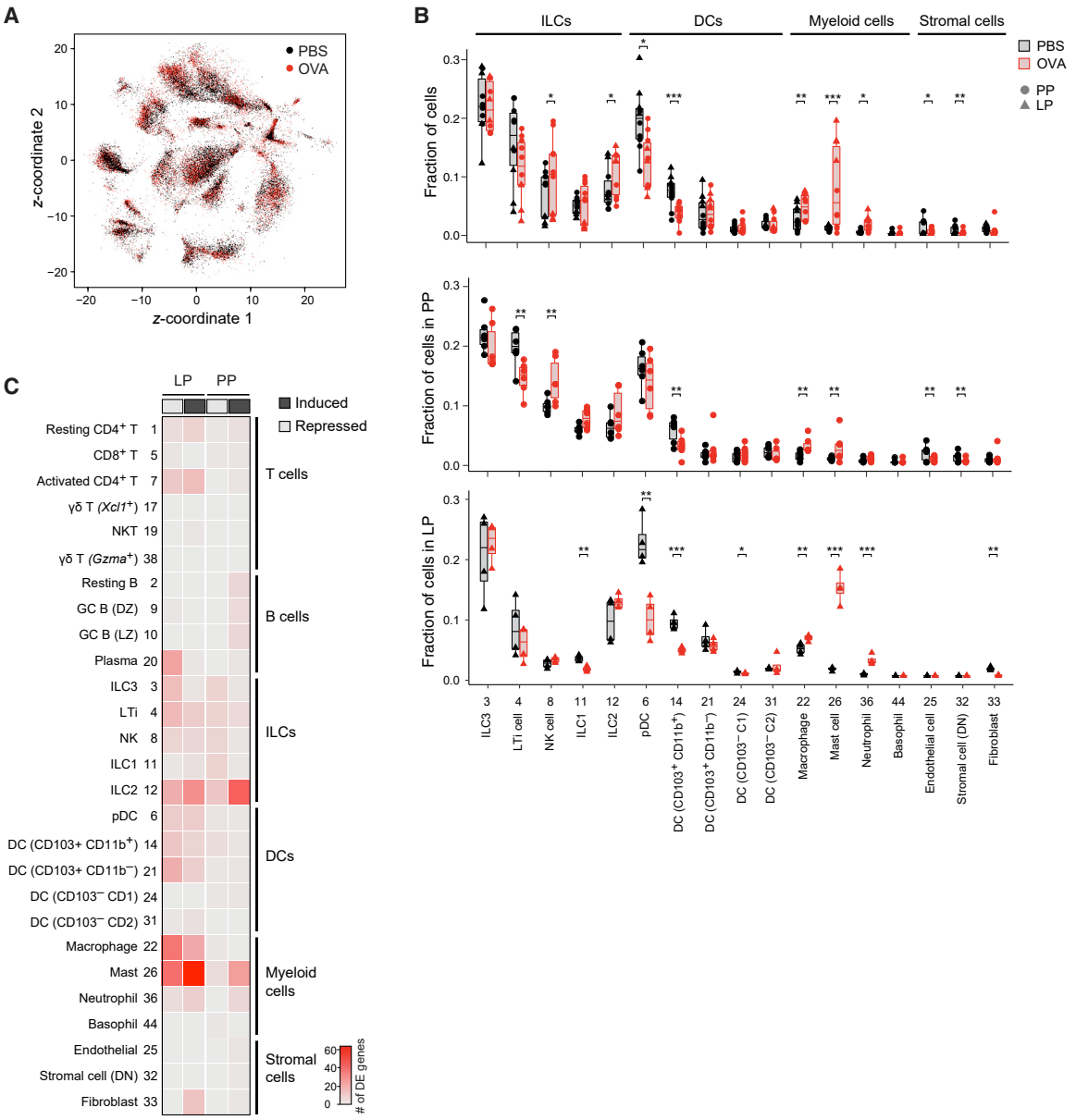


Figure 2. Increased ILC2 Proportions and Changes in ILC2 Programs Are Key Features in OVA-Induced Type 2 Inflammation

(A and B) Increased ILC2 and mast cell frequencies are prominent features in type 2 inflammation.

(A) A 2D embedding as in Figure 1B and colored by states (PBS or OVA).

(B) Distribution of cell type proportions (y axis) for each non-T and non-B cell subset (x axis) in the combined PP+LP dataset (top), PP (middle), or LP (bottom) in homeostatic (black) or OVA-induced inflammatory (red) conditions. Points represent independent mice; boxplots show IQR as in Figure 1C. *$p < 5 \times 10^{-2}$, **$p < 3 \times 10^{-5}$, and ***$p < 7 \times 10^{-11}$, Wald test (STAR Methods).

(C) ILC2s and mast cells show the most prominent changes in expression programs in type 2 inflammation. Number of genes significantly induced (black) or inhibited (gray) by OVA-induced type 2 inflammation in each cell subset (row) from the LP or PP regions.

Data are from seven independent experiments.

See also Figure S2 and Table S3.

2014), were the most significantly reduced by OVA-induced inflammation ($p = 6.4 \times 10^{-11}$, Wald test), suggesting that they are likely involved in the maintenance of gut homeostasis and suppressed during type 2 inflammation. The cellular compositions of T and B cell clusters were not significantly altered by the inflammation (data not shown).

Although most cell types changes (or lack thereof) were consistent between compartments and detected regardless of whether they were analyzed separately or jointly, there were some notable exceptions (Figure 2B). First, the proportion of ILC2s (cluster 12 cells) was significantly different between conditions only in the combined data ($p = 1.5 \times 10^{-2}$, Wald test) and

borderline otherwise, suggesting gained statistical power from analyzing the combined data. Conversely, the proportion of each of ILC1s (cluster 11) and fibroblasts (cluster 33) was changed in the two regions in opposite ways (enriched in one and depleted in the other), such that no significant change was detected when the two regions were considered together. The proportion of cells from several clusters was different in one region, but not the other (pDCs [cluster 6], neutrophils [cluster 36], endothelial cells [cluster 25], stromal cells [double negative (DN)] [cluster 32]), although this change was substantial enough to have been detected in the combined data. Thus, the negative binomial regression framework is a principled way of combining data from multiple regions (here, PP and LP) to quantify the significance of allergy on cell composition changes, simultaneously accounting for the influence of regions, and using raw count data instead of ratios.

The impact of type 2 inflammation on cell-intrinsic expression changes was most prominent in mast cells and ILC2s in both LP and PP regions (Figure 2C; Table S3). Genes associated with cell-type-specific activation were induced in mast cells (e.g., *Mcpt1* and *Mcpt4*) and ILC2s (e.g., *Il13* and *Il4*) (Figure S2C), suggesting an activation phenotype in both cell types. In addition, *Ighg1* and *Ighe* expression in plasma cells was significantly increased ($p = 1.45 \times 10^{-107}$ and 2.86×10^{-13}, respectively; likelihood ratio test) after the induction of allergic inflammation (Figure S2D), consistent with the fact that IL-4 induces class-switch recombination of the immunoglobulin heavy (Ig) chain toward IgG1 and IgE (Manis et al., 2002). Additionally, genes involved in the type 1 interferon pathway, such as *Irf1* and *Isg15* in macrophages and *Ifnar1* and *Ifitm3* in plasma cells, were suppressed during type 2 inflammation (Figure S2C), providing potential mechanistic explanations for the dampened antiviral immunity in allergic inflammation (Kloepfer et al., 2012; Rowe and Gill, 2015).

Topic Models Identify Cell-Type-Specific Programs that Are Increased with Inflammation in Mast Cells, ILC2s, Th2 Cells, and Fibroblast Subsets

To identify more nuanced changes in expression programs in response to type 2 inflammation, we relied on topic modeling using latent Dirichlet allocations (Blei et al., 2003), which has recently been applied to scRNA-seq data (Bielecki et al., 2018; duVerle et al., 2016). Originally developed to discover semantic topics reflected by words in documents (Dumais et al., 1990), topic modeling can be used to explore gene programs (“topics”) in each cell (“document”) based on the distribution of genes (“words”) expressed in the cell (STAR Methods). One gene can belong to multiple topics (programs) and its relative relevance in the topic is reflected by a weight. A cell is represented as a weighted mixture of topics, where the weights reflect the importance of the topic in the cell. We learned topic models for each cell lineage or group separately (Figures 3A-3E and S3A–S3F; Table S4), recovering both cell-type-specific programs (e.g., topic 1 of myeloid cells; Figure 3A) and ones that do not merely conform to cluster boundaries (e.g., topic 4 of B cells; Figure S3B). We focused on topics whose cell scores were differentially weighted between homeostasis and inflammation in a given cell lineage or group.

Topics characterizing activation programs had higher weights in mast cells and ILC2s from the inflammatory condition. In myeloid cells, topic 1 (“mast cell activation program”) was heavily weighted in the mast cell cluster, characterized by *Cpa3* and *Mcpt4* expression, and was significantly more prominent in mast cells from mice treated with OVA than controls ($p = 2.84 \times 10^{-67}$, Mann-Whitney *U* test; Figure 3A). In ILCs, topic 2 (“ILC2 activation program”) was heavily weighted in the ILC2 cluster, composed of type 2 genes such as *Il13* and *Il4*, and was significantly more prominent after induction of inflammation ($p = 8.01 \times 10^{-12}$, Mann-Whitney *U* test; Figure 3B).

Gene programs related to inflammatory responses were more heavily weighted in Th2 cells under inflammatory conditions, whereas those related to T regulatory cells were unchanged between inflammation and homeostasis. Specifically, in the topic model for T cells, topic 5 (“Th2 inflammatory program”) was heavily weighted in only the subset of cells from the activated $CD4^+$ T cell cluster that are likely Th2 cells (Figure 3C). This topic consisted of type 2 inflammatory genes (e.g., *Il13*, *Gata3*, *Il6*, *Areg*, and *Il1rl1*) and the cell weights were significantly higher in cells from OVA-treated mice than from controls ($p = 2.73 \times 10^{-5}$, Mann-Whitney *U* test; Figure 3C). Topic 9 (“T regulatory program”) included *Foxp3*, *Lag3*, *Il10*, and other Th cell regulatory genes and was present in a different subset of $CD4^+$ T cells (Figure 3D). The cell weights for this topic, however, showed only a minor change with inflammation ($p = 0.002$, Mann-Whitney *U* test; Figure 3D). Thus, activation of type 2 inflammation in the OVA allergy model may not have significantly interfered with the activity of regulatory T cells.

In stromal cells, topic 4, defined by the expression of the type 2 inflammatory cytokine *Il33* and key chemokines such as *Ccl21a*, was uniquely associated with the fibroblast cluster, and the cell weights were higher in the inflammatory condition (Figure 3E; $p = 2.69 \times 10^{-5}$, Mann-Whitney *U* test). We confirmed that IL-33 and CCL21 were co-expressed in $PDPN^+$ stromal cells by immunofluorescence (Figure S3G). Moreover, the number of $IL\text{-}33^+PDPN^+$ intestinal fibroblasts was significantly increased in mice under type 2 inflammation induced by OVA (Figure 3F), indicating that stromal-cell-derived IL-33 may play critical roles in promoting intestinal type 2 inflammation.

Calca-Encoded α-CGRP Expression Is a Key Feature of the ILC2 Activation Program Induced by Inflammation, but Its Receptor Is Repressed by Inflammation

Calca was the highest and most uniquely scoring gene in the ILC2 activation program (Figure 3B), and *Calca* transcript amounts were higher in ILC2s than in other cell types in our dataset (Figure 4A and S4A). Exons 4 and 5 of *Calca* encode the neuropeptides calcitonin (CT) and α-CGRP, respectively, via alternative splicing (Amara et al., 1982). qPCR revealed that while CT-encoding exon 4 was expressed in intestinal $KLRG1^+$ ILC2s at steady state (Figure S4B), α-CGRP-encoding exon 5 was detectable only following intragastric administration of OVA (Figures 4B and S4C). Conversely, the corresponding transcripts of α-CGRP receptor components (a G-protein-coupled receptor complex consisting of CRLR and RAMP1) was expressed in ILC2s at steady state (Figure 4B and S4A) but significantly repressed by intestinal type 2 inflammation (Figure 4B and S4C). The *Calcr* transcript, encoding the CT receptor, was not detectable by either scRNA-seq or qPCR (data not shown). Taken together, these results are consistent with a negative

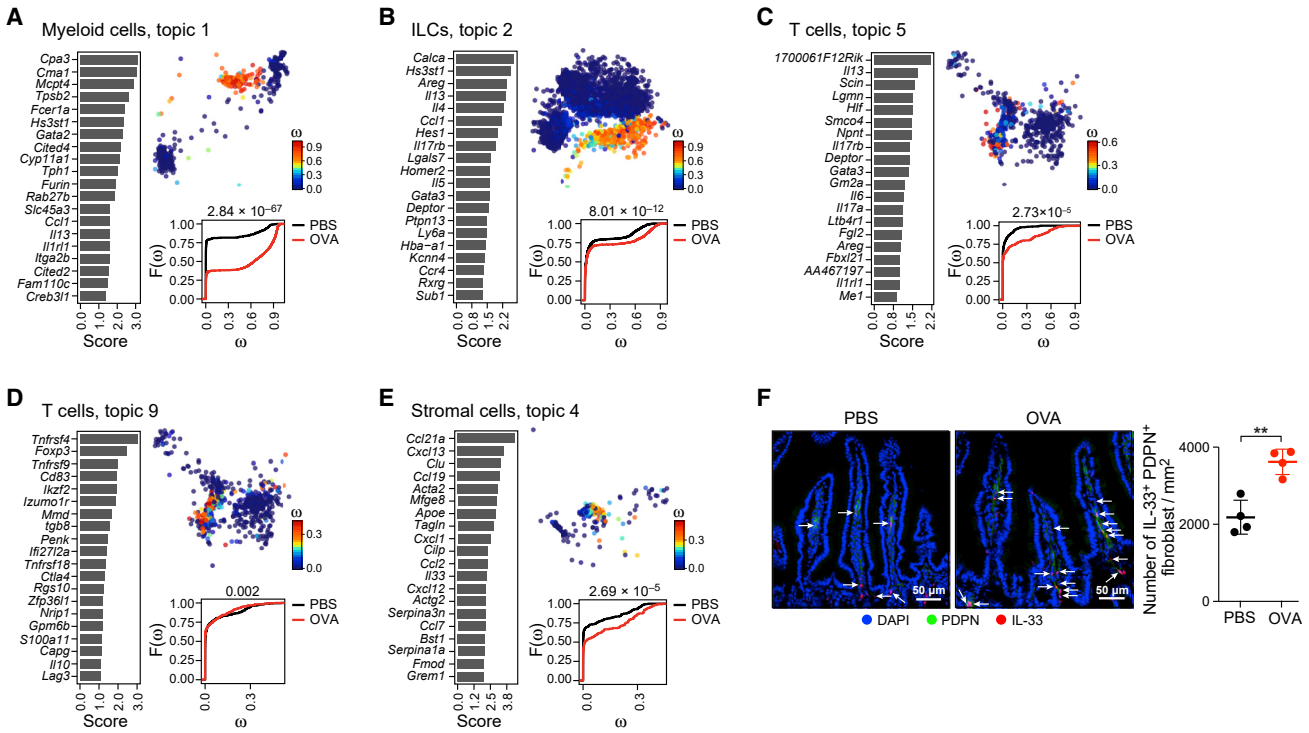


Figure 3. Topic Modeling of Cell-Type-Specific Programs in Response to Intestinal Type 2 Inflammation Predicts *Calca* as a Top Gene in ILC2s

(A–E) Inflammation associated programs in specific cell subsets. Shown are some of the topics that have differential scores between steady-state (PBS) and inflammatory conditions (OVA) for myeloid cells (A), ILCs (B) and T cells (C and D) in LP, or stromal cells (E) in PP. Left: bar plot showing the scores (x axis) of top ranked genes for this topic (y axis). Top right: a portion of the 2D embedding in Figure 1B, showing only cells from the noted subset cells, colored by the topic's weight in the cell (top right). Bottom right: empirical cumulative density function (y axis) of topic weights (x axis) for cells from mice treated with PBS (black curve) or OVA (red curve). p values were determined using a Mann-Whitney *U* test.

(F) Increased number of IL-33$^+$PDPN$^+$ fibroblasts in inflammation. Left: representative immunofluorescence (IF) images of the small intestines. Arrow shows IL-33$^+$PDPN$^+$ fibroblasts; scale bars, 50 μm. Points show individual mice. Data represent mean and SEM; **$p < 0.01$, Student's t test.

Data are from seven (A–E) or two (F) independent experiments. See also Figure S3 and Table S4.

feedback model where signaling through α-CGRP to ILC2s suppresses expression of its receptor in the cells and suggest that an α-CGRP-mediated signaling pathway may regulate intestinal ILC2 activity in type 2 immune responses.

α-CGRP Suppresses Type 2 Inflammation-Induced Activation and Expansion of ILC2s *In Vitro* and *In Vivo*

To determine if α-CGRP can directly trigger signaling in ILC2s and impact their transcriptional states under inflammatory conditions, we performed bulk RNA-seq of KLRG1$^+$ ILC2s isolated from the small intestine and stimulated *in vitro* with IL-25 alone or together with α-CGRP for 3 h. As expected, IL-25 alone induced the expected activation phenotype, including expression of key mitotic genes, such as *Myc*, and type 2 cytokines, such as *Il13* and *Il5* (Figure 4C). We confirmed IL-5 and IL-13 induction at the protein level (Figure 4D).

Continuous exposure to IL-25 was required for the induction of α-CGRP expression in intestinal ILC2s. While *in vitro* stimulation with IL-25 for 3 h did not alter expression of the α-CGRP exon (data now shown), extended stimulation for 24 h significantly induced the exon expression (>6-fold; Figure S4D), consistent with the *in vivo* chronic inflammation model (Figure 4B).

The IL-25-induced activation signature was significantly suppressed when cells were treated with both IL-25 and α-CGRP (Figures 4C and S4E), with the exception of a few genes, notably *Il5*, which was further significantly induced (Figures 4C and D). Moreover, α-CGRP co-treatment significantly suppressed IL-25-induced cell division (Figure 4E). Thus, α-CGRP inhibits proliferation and activation of intestinal KLRG1$^+$ ILC2s but induces expression of key genes, including *Il5* and *Areg* (Figure S4F), highlighting its dual regulatory roles in intestinal ILC2s in the context of IL-25-induced activation.

We next used an IL-25-induced *in vivo* activation model (Huang et al., 2015; Figure 5A) to show that α-CGRP suppresses expansion of ILC2s responding to inflammation. Intraperitoneal administration of α-CGRP into wild-type mice impaired IL-25-induced expansion of KLRG1$^+$ ILC2s (Figures 5B and S5A), consistent with our *in vitro* results. Recent work has shown that intestinal inflammatory ILC2s (KLRG1$^+$ST2$^-$) can migrate to mesenteric lymph nodes (mLNs) and other tissues during inflammation via sphingosine 1-phosphate (S1P)-mediated chemotaxis (Huang et al., 2018). To determine whether α-CGRP primarily impacts intestinal or mLN ILC2s, we relied on the fact that ~90% of intestinal KLRG1$^+$ ILC2s are phenotypically ST2$^-$ (Figure S5B), whereas mLN ILC2s are mainly ST2$^+$ at

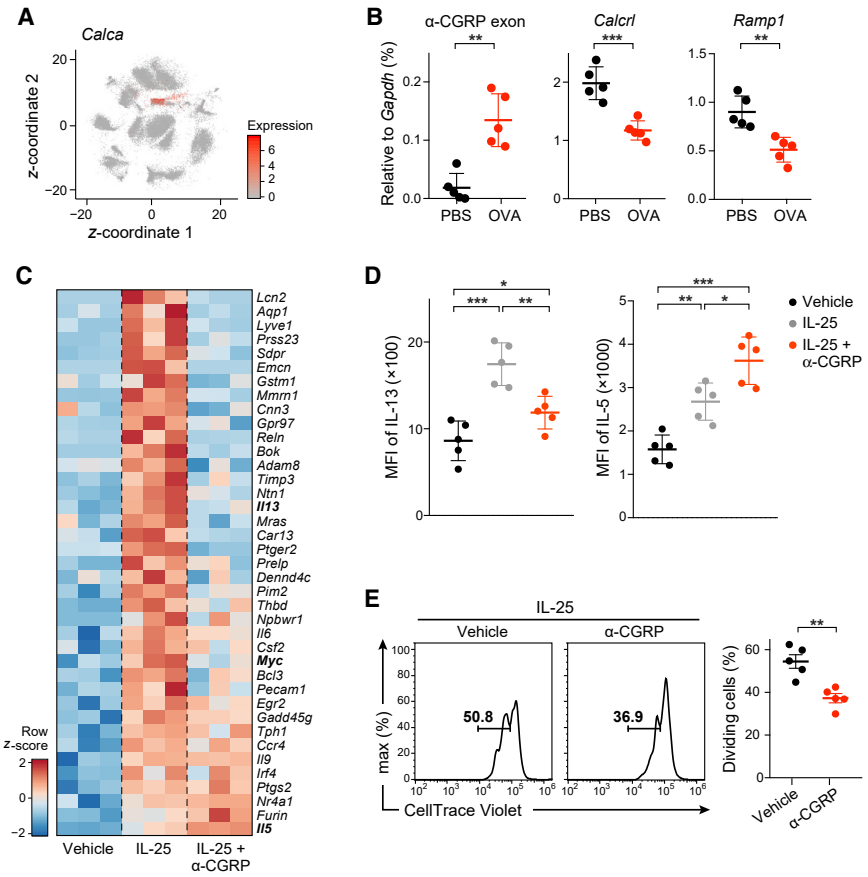


Figure 4. α-CGRP Suppresses IL-25-Induced Activation and Expansion of Intestinal KLRG1$^+$ ILC2s *In Vitro*

(A) Cells expressing the *Calca* gene. 2D embedding as in Figure 1B where cells (dots) are colored by relative expression of *Calca* (log_2(TP10K+1)), where TP10K represents transcripts per 10,000.

(B) α-CGRP exon specifically induced in inflammation. Expression amounts (y axis) of α-CGRP exon of *Calca*, *Calcrl*, and *Ramp1* in LP ILC2s isolated from control (black) or OVA-treated (red) mice on day 36 (Figure S1A). Points represent individual experiments.

(C and D) α-CGRP co-treatment abrogates most of the IL-25-induced response in LP ILC2s *in vitro*. (C) Expression (color bar, *Z* score) of genes (rows) significantly induced in ILC2s (fold change ≥2, $p < 0.05$) by IL-25 compared to control, across different conditions. (D) Intracellular amounts (mean fluorescence intensity [MFI], y axis) of IL-13 and IL-5 in ILC2s following indicated stimulations for 12 h. Points represent individual experiments.

(E) α-CGRP suppresses IL-25-indcued proliferation of LP ILC2s. Left: distribution of the number of cell divisions (y axis, percentage of maximum observed number) monitored by flow cytometry. Right: percentage of dividing cells (y axis) in each treatment (x axis). Points represent individual experiments. Data represent mean ± SEM; *$p < 0.05$, **$p < 0.01$, and ***$p < 0.001$, Student's t test (B, D, and E).

Data are from seven (A) or five (B, D, and E) independent experiments, or representative of two (C) independent experiments.

See also Figure S4.

steady state (Figure 5C). IL-25 administration increased the frequency of both KLRG1$^+$ST2$^-$ inflammatory ILC2s and ST2$^+$ ILC2s in mLNs (Figure 5C—5E and S5C), but co-administration with α-CGRP only reduced the frequency of KLRG1$^+$ST2$^-$ ILC2s (Figures 5C, 5D, and S5C), which are cells that migrated from the small intestine to the mLNs (Huang et al., 2018), but not of ST2$^+$ ILC2s (Figure 5E). Thus, α-CGRP preferentially regulates the response of intestinal KLRG1$^+$ST2$^-$ ILC2s. Furthermore, α-CGRP also significantly suppressed the expansion of intestinal ILC2s in a food allergy model (Figures 5F, 5G, and S5D), where we intragastrically administrated α-CGRP together with OVA into pre-sensitized mice. Importantly, mast cell expansion, the main phenotypic marker of allergic inflammation in this model (Brandt et al., 2003), was significantly suppressed in the presence of α-CGRP (Figure 5H), whereas the frequencies of other major immune cell types remained unchanged (Figure S5E). Taken together, α-CGRP antagonized expansion of intestinal KLRG1$^+$ ILC2s and type 2 inflammation *in vivo*.

At Homeostasis, α-CGRP Is Predominantly Expressed *In Vivo* in Two Subsets of ChAT$^+$ Enteric Neurons

Without inflammation, intestinal KLRG1$^+$ ILC2s expressed CGRP receptors (Figure 4B), but not CGRP, leading us to search for neighboring cell types that potentially produce CGRP at homeostasis. To this end, we analyzed *Calca* gene expression across multiple intestinal scRNA-seq datasets, including our previous epithelial atlas for the mouse small intestine epithelium (Haber et al., 2017; Figure S6A), our intestinal immune atlas here (Figure 1), and scRNA-seq of enteric neurons from Wnt1-Cre:R26Tomato mice (Zeisel et al., 2018; Figures 6A, S6B, and S6C). *Calca* expression was detected in two subsets of ChAT$^+$ enteric neurons (Figures 6B and S6C). These ChAT$^+$ enteric neurons also expressed (Figure 6B): (1) the CGRP receptor genes; (2) the *Calcb* gene, encoding β-CGRP peptide, which differs by two amino acids from α-CGRP but has not been substantially studied for its function in immune cells; and (3) the *Nmu* gene, which we and others have shown amplifies the activity of ILC2s under type 2 inflammation in the lung and small intestine (Cardoso et al., 2017; Klose et al., 2017; Wallrapp et al., 2017).

We confirmed by immunofluorescence staining that ChAT$^+$ enteric neurons expressed CGRP (Figure 6C), and that ILC2s contact with CGRP-expressing neurons at the steady state (Figure S6D), consistent with previous reports that ILC2s are closely associated with neurons in the intestine (Klose et al., 2017). Thus, CGRP from these ChAT$^+$ enteric neurons may regulate ILC2 homeostasis.

α-CGRP Suppresses ILC2 Proliferation through Activating a cAMP Response Module

The presence at homeostasis of α-CGRP receptors on ILC2s and α-CGRP's expression on ChAT$^+$ intestinal neurons led us to hypothesize that α-CGRP has an effect on ILC2s during homeostasis. To test this hypothesis, we next measured the expression profiles of intestinal KLRG1$^+$ ILC2s stimulated

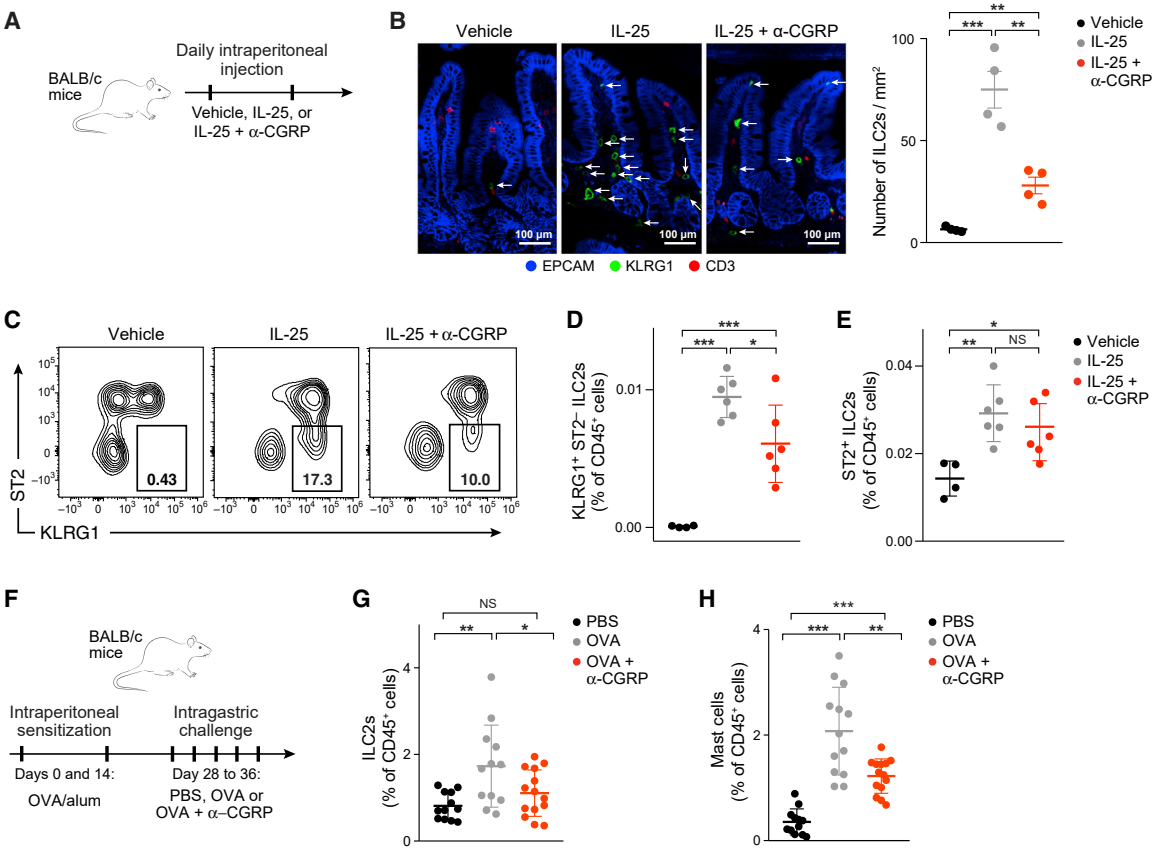


Figure 5. α-CGRP Antagonizes Expansion of Intestinal KLRG1⁺ ILC2s *In Vivo*

(A) Experimental design.

(B) α-CGRP co-treatment antagonizes ILC2 expansion *in vivo*. Representative IF images (left, scale bars, 100 μm) and cell densities (number of cells/mm^2) of CD3$^-$KLRG1$^+$ ILC2 (left, arrows) in the small intestines of mice treated as in (A). Points represent individual mice.

(C–E) α-CGRP antagonizes the expansion of ST2$^-$KLRG1$^+$ ILC2s specifically. (C) Flow cytometry analysis of ILC2s in mLNs gated on CD45$^+$Lin$^-$CD90.2$^+$IL7R$^+$ from mice treated as in (A). (D) Frequency (y axis) of ST2$^-$KLRG1$^+$ ILC2s in total CD45$^+$ cells in mLNs of mice treated as in (A). Points represent individual mice. (E) Frequency (y axis) of ST2$^+$ ILC2s in total CD45$^+$ cells in mLNs of mice treated as in (A). Points represent individual mice.

(F and G) α-CGRP treatment antagonizes LP ILC2 expansion in OVA-induced type 2 inflammatory model. (F) Experimental overview. (G) Percentage of ILC2s (y axis) in total CD45$^+$ cells in mice treated as in (F) on day 36. Points represent individual mice.

(H) α-CGRP treatment suppresses expansion of mast cells in LP in OVA-induced type 2 inflammatory model. Percentage of FceRIa$^+$SiglecF$^{low/-}$Lin^{low} mast cells (y axis) in total CD45$^+$ cells in mice treated as in (F) on day 36. Data represent mean ± SEM; *p < 0.05, **p < 0.01, ***p < 0.001, and NS, p > 0.05, Student's t test (B, D, E, G, and H).

Data are from two (B), three (C–E), or four (G and H) independent experiments.

See also Figure S5.

in vitro by α-CGRP alone and identified genes differentially expressed under this signal (Figure 6D; STAR Methods).

Analyzing the gene expression suggested that α-CGRP activated a cAMP response module. First, α-CGRP stimulation induced expression of key genes involved in adenylate-cyclase-mediated GPCR signaling, including *Adrb2*, *Adora2a*, and *Pde4b* (Figure 6D), as well as cAMP response genes, including *Areg* (Shao and Sheng, 2010), *Crem*, and *Il5* (Figure 6D). Previous studies showed that cAMP directly induces IL-5 expression in ILC2s (Nussbaum et al., 2013). Moreover, assay for transposase-accessible chromatin using sequencing (ATAC-seq) profiling of ILC2s revealed that regions of increased chromatin accessibility following α-CGRP stimulation were enriched for gene loci involved in the adenylate cyclase pathway (Figure 6E; Table S5). Consistently, α-CGRP stimulation alone induced the accumulation of intracellular cAMP in ILC2s (Figure 6F).

α-CGRP stimulation *in vitro* negatively regulated ILC2 proliferation, and this effect may be mediated by induction of genes involved in cell-cycle arrest in the cAMP response module. In our KLRG1$^+$ ILC2 cells, α-CGRP induced expression of genes involved in cell-cycle arrest, such as *Cdkn1a*, *Gadd45a*, and *Akap12*, as well as key negative regulators of ILC2 expansion, *Adrb2* and *Pdcd1* (Moriyama et al., 2018; Taylor et al., 2017; Figure 6D). cAMP and its principal target, cAMP-dependent protein kinase (PKA), have been previously shown to suppress proliferation via negatively regulating mitogen-activated protein (MAP) kinase cascade in a cell-context-dependent manner (Stork and Schmitt, 2002). Indeed, the adenylate cyclase activator forskolin, which increases intracellular cAMP concentrations (Rodriguez

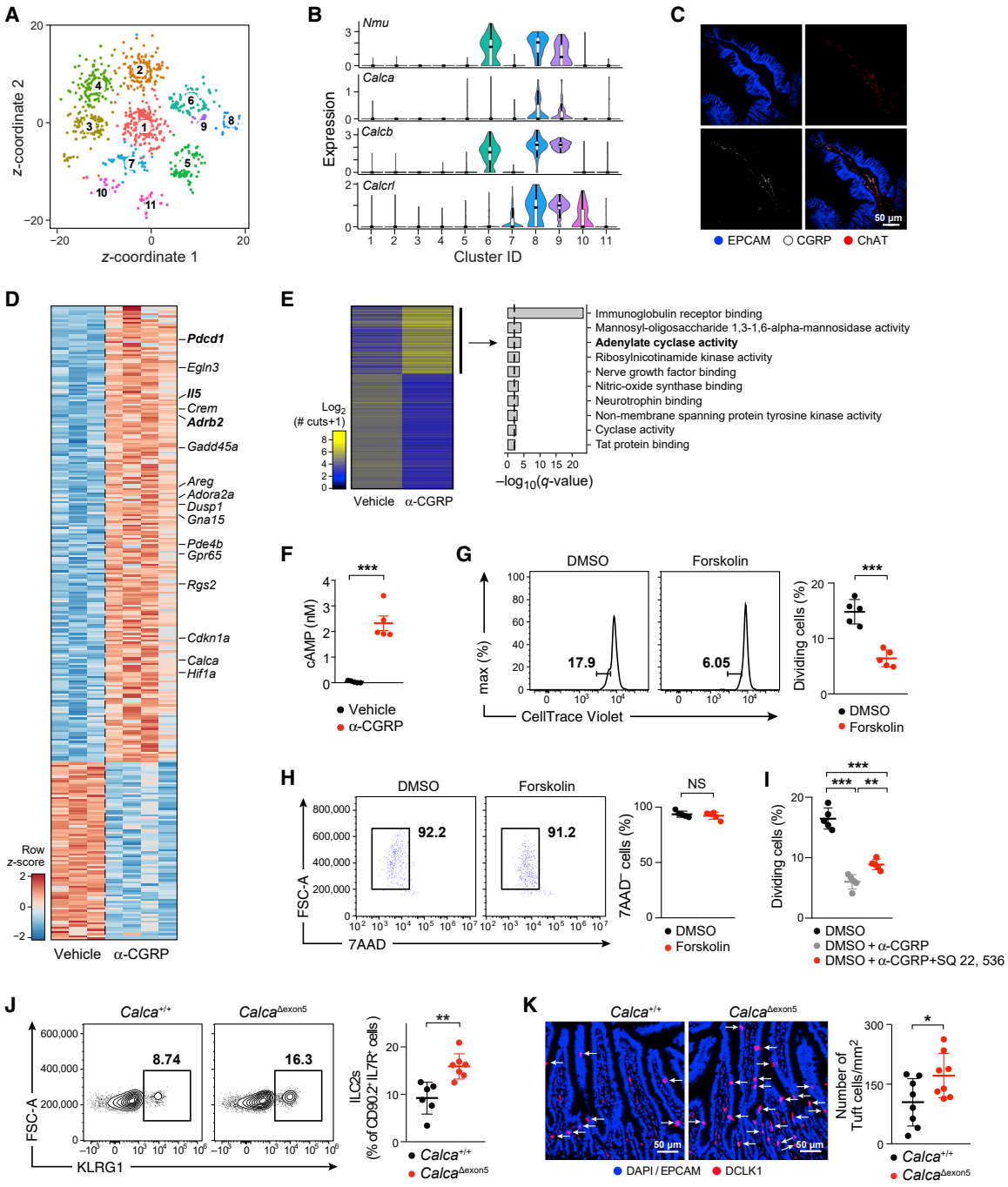


Figure 6. α-CGRP Is Produced by ChAT$^+$ Enteric Neurons in Steady States and Maintains Intestinal KLRG1$^+$ ILC2 Homeostasis *In Vivo*

(A and B) ChAT$^+$ enteric neurons express α-CGRP. (A) t-SNE plot of 1,105 enteric neuron profiles from Wnt1-Cre:R26Tomato mice (Zeisel et al., 2018), where each neuron (dot) is colored by cluster assignment. (B) Distribution of expression amounts (y axis, $\log_2$(TP10K+1)) of *Nmu*, *Calca*, *Calcb*, and *Calcrl* gene in the enteric neurons in each cluster in (A; x axis).

(C) Co-localization of ChAT and CGRP in the small intestines of WT mice. Scale bar, 50 μm.

(D) Expression program induced by α-CGRP in LP ILC2s. Relative expression (row-wise *Z* score of $\log_2$(TPM + 1)) of genes (rows) significantly induced or suppressed by α-CGRP stimulation for 3 h. Key genes are highlighted.

(E) α-CGRP stimulation in ILC2s *in vitro* reprograms chromatin accessibility especially at loci of a cAMP response module. Left: chromatin accessibility ($\log_2$(#cuts+1); STAR Methods) of loci (rows) with differential accessibility in LP ILC2s treated by α-CGRP versus control *in vitro* for 3 h. Right: statistical significance (x axis, $-\log_{10}$(q-value)) of molecular functions (y axis) whose associated genes are enriched in proximity to these differentially accessible ATAC-seq peaks. Dashed line, q value = 0.01.

(legend continued on next page)

et al., 2013), suppressed the proliferation of ILC2s (Figure 6G), but not their viability (Figure 6H). Furthermore, short treatment of ILC2s with a low concentration of adenylate cyclase inhibitor (Klein et al., 2012) preserved cell viability and partially rescued the cell proliferation defect mediated by α-CGRP (Figure 6I). Taken together, our data demonstrate that increased concentration of intracellular cAMP, potentially cooperating with other additional pathways, supports the inhibitory role of α-CGRP in intestinal ILC2 proliferation.

At Homeostasis, α-CGRP Maintains ILC2 and Type 2 Responses *In Vivo*

Finally, we used *Calca*$^{\Delta exon5}$ mice, in which the α-CGRP exon is deficient but the CT exon remains intact (Oh-hashi et al., 2001), as a loss-of-function model to demonstrate α-CGRP-mediated signaling constrains intestinal KLRG1$^+$ ILC2s. The frequency of intestinal ILC2s in *Calca*$^{\Delta exon5}$ mice was increased in the IL-25 induced inflammatory condition (Figure S6E), in line with our observations in gain-of-function models (Figures 5A and 5B). Moreover, the absence of α-CGRP already significantly increased the frequency of intestinal KLRG1$^+$ ILC2s at steady state (Figure 6J). Type 2 cytokines promote differentiation of tuft cells (Biton et al., 2018; Gerbe et al., 2016; Howitt et al., 2016; von Moltke et al., 2016), and consistently, the number of tuft cells, which lack detectable transcription of CGRP receptors (Figure S6A), was significantly increased in *Calca*$^{\Delta exon5}$ mice (Figure 6K). Thus, α-CGRP-mediated signaling helped maintain the homeostasis of KLRG1$^+$ ILC2s and type 2 immunity in the small intestine.

DISCUSSION

Our atlas and analysis revealed a role for α-CGRP in suppressing the expansion of intestinal ILC2s in both IL-25-induced acute inflammation and OVA-induced allergic inflammation models. In acute inflammation, ILC2s are still robustly expanded under co-administration of α-CGRP, likely due to IL-25's exceptional potency as an activator. Previous studies showed that CGRP signaling can generate both pro- and anti-inflammatory immune responses, depending on cell type, tissue, and model (Assas et al., 2014). α-CGRP increases IL-5 expression in lung ILC2s co-stimulated with IL-33 (Sui et al., 2018). Mice with deficiency in CRLR in IL-5-expressing cells manifest a normal frequency of ST2$^+$ ILC2s in lungs exposed to house dust mite (HDM) (Sui et al., 2018), consistent with our finding that ST2$^+$ ILC2s in mLNs are not significantly affected by α-CGRP administration. However, we further revealed that α-CGRP reduced the expansion of intestinal KLRG1$^+$ ILC2s. Thus, our work highlights dual regulatory roles of α-CGRP, which promotes IL-5 production but inhibits expansion of intestinal KLRG1$^+$ ILC2s. Although differences in cell states between lung ST2$^+$ and intestinal ST2$^-$ KLRG1$^+$ ILC2s (Ricardo-Gonzalez et al., 2018) might contribute to their differential reactions to CGRP signaling, additional studies in animal models where CRLR is specifically deleted in intestinal KLRG1$^+$ ILC2s will be needed to elucidate the full molecular mechanism. In addition, it will be important to compare the effects of α-CGRP versus β-CGRP binding to CRLR in ILC2s.

We revealed that two subsets of ChAT$^+$ enteric neurons are the predominant source of CGRP in the small intestine at steady state. In addition to multiple neuropeptides, these ChAT$^+$ neurons expressed *Il13ra1* and *Il4ra* (Figure S6C), which encode the components of the receptor complex for the type 2 cytokine IL-13. Thus, these ChAT$^+$ neurons may be specialized for cross-talk with the immune system. Future studies are needed to determine if cytokine signaling from immune cells during inflammation further boosts the secretion of neuropeptides.

CGRP signaling is an additional key axis of neuro-immune interaction with implications for inflammation, including food allergy. The nervous system exercises dual functions to either activate or inhibit ILC2s via different GPCRs (Cardoso et al., 2017; Klose et al., 2017; Moriyama et al., 2018; Wallrapp et al., 2017). We propose a model for how ILC2s integrate and balance such diverse neural signaling cues, involving different Gα proteins and their downstream signaling. The amplifier NMUR1 mainly signals through $G\alpha_{q/11}$ and inhibits cAMP concentrations (Martinez and O'Driscoll, 2015), whereas the negative regulators CRLR and β_2AR are both coupled with $G\alpha_s$ proteins that activate adenylate cyclase and the cAMP pathway (Chatterjee et al., 1993; Madamanchi, 2007). Intracellular cAMP accumulation induced expression of the cAMP response module, including IL-5, but suppressed ILC2 proliferation. Thus, selective activation of different subgroups of α subunits of G proteins coupled with variable downstream effects, including the concentration of cAMP, might be utilized by ILC2s to fine-tune the response to neuronal signaling.

Our work underscores the importance of α-CGRP modulating ILC2 activity, which may serve as a therapeutic target for treating diseases like food allergy. Since monoclonal antibodies against CGRP have been recently approved to treat migraine

(F) α-CGRP induces intracellular cAMP accumulation in ILC2s. cAMP concentration (μM, y axis) in LP ILC2s stimulated *in vitro* for 30 min as measured by ELISA. Points represent individual mice.

(G and H) Forskolin suppresses ILC2 proliferation but does not impact cell viability.

(G) Left: the number of cell divisions (y axis, percentage of maximum observed number) monitored by flow cytometry in LP ILC2s. Points represent individual experiments.

(H) Cell viability monitored by flow cytometry in cells in (G) stained with 7AAD. Points represent individual experiments.

(I) Adenylate cyclase inhibitor (SQ22, 536) treatment partially rescues α-CGRP inhibition of ILC2 proliferation. Percentage of divided cells (y axis) as assayed as in (F). LP ILC2s treated *in vivo* for 40 h. Points represent individual experiments.

(J and K) The deficiency of α-CGRP affects ILC2 expansion *in vivo*. (J) Left: flow cytometry analysis of LP ILC2s in WT and *Calca*$^{\Delta exon5}$ mice in homeostasis. Points represent individual mice. (K) Left: representative IF images of tuft cells (arrows) in the small intestine of WT or *Calca*$^{\Delta exon5}$ mice. Scale bars, 50 μm. Right: density of tuft cells (y axis, number per mm^2) in WT and *Calca*$^{\Delta exon5}$ mice. Points represent individual mice.

Data represent mean ± SEM; *$p < 0.05$, **$p < 0.01$, ***$p < 0.001$, and NS, $p > 0.05$, Student's t test (F–K). Data are representative of three (C) or two (D) independent experiments or are from one (E), three (F, J, and K), or five (G–I) independent experiments.

See also Figure S6 and Table S5.

(Edvinsson, 2018), it will be important to monitor the incidence of allergic diseases in treated patients. More broadly, our work provides a resource for understanding the intestinal immune system in response to type 2 inflammation in the context of each specific cell type. Further exploration of the atlas can lead to additional hypotheses on circuits within and between additional cell types that contribute to type 2 immune responses.

STAR★METHODS

Detailed methods are provided in the online version of this paper and include the following:

- KEY RESOURCES TABLE
- LEAD CONTACT AND MATERIALS AVAILABILITY
- METHOD DETAILS
  - Mice
  - Isolation of cells from Peyer's patches (PPs)
  - Isolation of cells from the lamina propria (LP)
  - Flow cytometry and cell sorting
  - Droplet-based scRNA-seq
  - Quantitative real-time PCR
  - ILC2 culture
  - Immunofluorescence staining and imaging
  - Bulk RNA-seq
  - Overall Expression analysis
  - Bulk ATAC-seq
  - scRNA-seq data QC and pre-processing
  - Benchmarking different batch correction approaches
  - scRNA-seq clustering of PP cells
  - Clustering cross-validation of PP cells
  - Cluster annotation and filtering of PP cells
  - Clustering LP cells
  - Cellular composition changes
  - Cell sampling frequencies
  - Topic modeling
  - Statistical analysis
- DATA AND CODE AVAILABILITY

SUPPLEMENTAL INFORMATION

Supplemental Information can be found online at https://doi.org/10.1016/j.immuni.2019.09.004.

ACKNOWLEDGMENTS

We thank Leslie Gaffney and Anna Hupalowska for help with figures, Tim Tickle for help with the Single Cell Portal, Miao Xu and Chao Huang for help with tissue harvest, Yan Wang for help with qPCR, Hans Oettgen for discussions, Hiroki Kurihara for donating the B6.129S6-Calca < tm1Hku > strain to a publicly available repository, the Broad Flow Cytometry Facility, and the Flow Cytometry Core and Laboratory Animal Resources Center in Westlake University. Work was supported by the Food Allergy Science Initiative, NIH grant DK114784 (A.R. and R.J.X.), NIH grant DK 043351, the Crohn's & Colitis Foundation (R.J.X.), the National Natural Science Foundation of China (grant 31970842; H.X.), the Westlake Education Foundation of Westlake University (H.X.), and the Klarman Cell Observatory and HHMI (A.R.).

AUTHOR CONTRIBUTIONS

H.X., R.J.X., and A.R. conceived and supervised this study. H.X. designed and performed all experiments. J.D. performed computational analysis with contributions from C.B.M.P., H.X., O.A., M.T., and R.J.X. and guidance from A.R.. A.W., X.G., S.F., C.S., P.R.B., H.N.S., and V.K.K. helped with animal work. S.M. assisted with ATAC-seq. D.D., L.T.N., and O.R.-R. assisted with scRNA-seq. A.L. assisted with bulk RNA-seq. H.X., J.D., A.R., and R.J.X. wrote the manuscript with input from all authors.

DECLARATION OF INTERESTS

A.R. is a scientific advisory board member of ThermoFisher Scientific, Neogene Therapeutics, and Syros Pharmaceuticals. A.R. and R.J.X. are co-founders of and equity holders in Celsius Therapeutics. H.X., R.J.X., and A.R. are co-inventors on US provisional patent application no. 62/667,381 filed by The Broad Institute relating to the subject matter of this manuscript. A.R., H.X., J.D., and R.J.X. are co-inventors on US provisional patent application no 62/818,404 filed by the Broad Institute relating to CGRP signaling modulation.

Received: May 29, 2019
Revised: August 6, 2019
Accepted: September 6, 2019
Published: October 15, 2019

REFERENCES

Amara, S.G., Jonas, V., Rosenfeld, M.G., Ong, E.S., and Evans, R.M. (1982). Alternative RNA processing in calcitonin gene expression generates mRNAs encoding different polypeptide products. Nature *298*, 240–244.

Artis, D., and Spits, H. (2015). The biology of innate lymphoid cells. Nature *517*, 293–301.

Assas, B.M., Pennock, J.I., and Miyan, J.A. (2014). Calcitonin gene-related peptide is a key neurotransmitter in the neuro-immune axis. Front. Neurosci. *8*, 23.

Bielecki, P., Riesenfeld, S.J., Kowalczyk, M.S., Amezcua Vesely, M.C., Kroehling, L., Yaghoubi, P., Dionne, D., Jarret, A., Steach, H.R., McGee, H.M., et al. (2018). Skin inflammation driven by differentiation of quiescent tissue-resident ILCs into a spectrum of pathogenic effectors. bioRxiv. bioRxiv. https://doi.org/10.1101/461228.

Biton, M., Haber, A.L., Rogel, N., Burgin, G., Beyaz, S., Schnell, A., Ashenberg, O., Su, C.W., Smillie, C., Shekhar, K., et al. (2018). T helper cell cytokines modulate intestinal stem cell renewal and differentiation. Cell *175*, 1307–1320.e1322.

Blei, D.M., Ng, A.Y., and Jordan, M.I. (2003). Latent Dirichlet allocation. J. Mach. Learn. Res. *3*, 993–1022.

Blondel, V.D., Guillaume, T.J., Lambiotte, R., and Lefebvre, E. (2008). Fast unfolding of communities in large networks. J. Stat. Mech. *2008*, 10008.

Brandt, E.B., Strait, R.T., Hershko, D., Wang, Q., Muntel, E.E., Scribner, T.A., Zimmermann, N., Finkelman, F.D., and Rothenberg, M.E. (2003). Mast cells are required for experimental oral allergen-induced diarrhea. J. Clin. Invest. *112*, 1666–1677.

Buenrostro, J.D., Giresi, P.G., Zaba, L.C., Chang, H.Y., and Greenleaf, W.J. (2013). Transposition of native chromatin for fast and sensitive epigenomic profiling of open chromatin, DNA-binding proteins and nucleosome position. Nat. Methods *10*, 1213–1218.

Burton, O.T., Medina Tamayo, J., Stranks, A.J., Miller, S., Koleoglou, K.J., Weinberg, E.O., and Oettgen, H.C. (2018). IgE promotes type 2 innate lymphoid cells in murine food allergy. Clin. Exp. Allergy *48*, 288–296.

Butler, A., Hoffman, P., Smibert, P., Papalexi, E., and Satija, R. (2018). Integrating single-cell transcriptomic data across different conditions, technologies, and species. Nat. Biotechnol. *36*, 411–420.

Cardoso, V., Chesné, J., Ribeiro, H., García-Cassani, B., Carvalho, T., Bouchery, T., Shah, K., Barbosa-Morais, N.L., Harris, N., and Veiga-Fernandes, H. (2017). Neuronal regulation of type 2 innate lymphoid cells via neuromedin U. Nature *549*, 277–281.

Chatterjee, T.K., Moy, J.A., Cai, J.J., Lee, H.C., and Fisher, R.A. (1993). Solubilization and characterization of a guanine nucleotide-sensitive form of the calcitonin gene-related peptide receptor. Mol. Pharmacol. *43*, 167–175.

Chen, C., Grennan, K., Badner, J., Zhang, D., Gershon, E., Jin, L., and Liu, C. (2011). Removing batch effects in analysis of expression microarray data: an evaluation of six batch adjustment methods. PLoS ONE *6*, e17238.

Dey, K.K., Hsiao, C.J., and Stephens, M. (2017). Visualizing the structure of RNA-seq expression data using grade of membership models. PLoS Genet. *13*, e1006599.

Ding, J., Condon, A., and Shah, S.P. (2018). Interpretable dimensionality reduction of single cell transcriptome data with deep generative models. Nat. Commun. *9*, 2002.

Ding, J., Shah, S., and Condon, A. (2016). densityCut: an efficient and versatile topological approach for automatic clustering of biological data. Bioinformatics *32*, 2567–2576.

Dobin, A., Davis, C.A., Schlesinger, F., Drenkow, J., Zaleski, C., Jha, S., Batut, P., Chaisson, M., and Gingeras, T.R. (2013). STAR: ultrafast universal RNA-seq aligner. Bioinformatics *29*, 15–21.

Dumais, S.T., Furnas, G.W., Landauer, T.K., and Harshman, R. (1990). Indexing by latent semantic analysis. J. Am. Soc. Inf. Sci. *41*, 391–407.

duVerle, D.A., Yotsukura, S., Nomura, S., Aburatani, H., and Tsuda, K. (2016). CellTree: an R/bioconductor package to infer the hierarchical structure of cell populations from single-cell RNA-seq data. BMC Bioinformatics *17*, 363.

Edvinsson, L. (2018). CGRP antibodies as prophylaxis in migraine. Cell *175*, 1719.

Finak, G., McDavid, A., Yajima, M., Deng, J., Gersuk, V., Shalek, A.K., Slichter, C.K., Miller, H.W., McElrath, M.J., Prlic, M., et al. (2015). MAST: a flexible statistical framework for assessing transcriptional changes and characterizing heterogeneity in single-cell RNA sequencing data. Genome Biol. *16*, 278.

Gerbe, F., Sidot, E., Smyth, D.J., Ohmoto, M., Matsumoto, I., Dardalhon, V., Cesses, P., Garnier, L., Pouzolles, M., Brulin, B., et al. (2016). Intestinal epithelial tuft cells initiate type 2 mucosal immunity to helminth parasites. Nature *529*, 226–230.

Gieseck, R.L., 3rd, Wilson, M.S., and Wynn, T.A. (2018). Type 2 immunity in tissue repair and fibrosis. Nat. Rev. Immunol. *18*, 62–76.

Haber, A.L., Biton, M., Rogel, N., Herbst, R.H., Shekhar, K., Smillie, C., Burgin, G., Delorey, T.M., Howitt, M.R., Katz, Y., et al. (2017). A single-cell survey of the small intestinal epithelium. Nature *551*, 333–339.

Haghverdi, L., Lun, A.T.L., Morgan, M.D., and Marioni, J.C. (2018). Batch effects in single-cell RNA-sequencing data are corrected by matching mutual nearest neighbors. Nat. Biotechnol. *36*, 421–427.

Hammad, H., and Lambrecht, B.N. (2015). Barrier epithelial cells and the control of Type 2 immunity. Immunity *43*, 29–40.

Heng, T.S., and Painter, M.W.; Immunological Genome Project Consortium (2008). The Immunological Genome Project: networks of gene expression in immune cells. Nat. Immunol. *9*, 1091–1094.

Hepworth, M.R., Monticelli, L.A., Fung, T.C., Ziegler, C.G., Grunberg, S., Sinha, R., Mantegazza, A.R., Ma, H.L., Crawford, A., Angelosanto, J.M., et al. (2013). Innate lymphoid cells regulate CD4+ T-cell responses to intestinal commensal bacteria. Nature *498*, 113–117.

Howitt, M.R., Lavoie, S., Michaud, M., Blum, A.M., Tran, S.V., Weinstock, J.V., Gallini, C.A., Redding, K., Margolskee, R.F., Osborne, L.C., et al. (2016). Tuft cells, taste-chemosensory cells, orchestrate parasite type 2 immunity in the gut. Science *351*, 1329–1333.

Huang, Y., Guo, L., Qiu, J., Chen, X., Hu-Li, J., Siebenlist, U., Williamson, P.R., Urban, J.F., Jr., and Paul, W.E. (2015). IL-25-responsive, lineage-negative KLRG1(hi) cells are multipotential 'inflammatory' type 2 innate lymphoid cells. Nat. Immunol. *16*, 161–169.

Huang, Y., Mao, K., Chen, X., Sun, M.A., Kawabe, T., Li, W., Usher, N., Zhu, J., Urban, J.F., Jr., Paul, W.E., and Germain, R.N. (2018). S1P-dependent interorgan trafficking of group 2 innate lymphoid cells supports host defense. Science *359*, 114–119.

Jerby-Arnon, L., Shah, P., Cuoco, M.S., Rodman, C., Su, M.J., Melms, J.C., Leeson, R., Kanodia, A., Mei, S., Lin, J.R., et al. (2018). A cancer cell program promotes T cell exclusion and resistance to checkpoint blockade. Cell *175*, 984–997.e924.

Klein, M., Vaeth, M., Scheel, T., Grabbe, S., Baumgrass, R., Berberich-Siebelt, F., Bopp, T., Schmitt, E., and Becker, C. (2012). Repression of cyclic adenosine monophosphate upregulation disarms and expands human regulatory T cells. J. Immunol. *188*, 1091–1097.

Kloepfer, K.M., Olenec, J.P., Lee, W.M., Liu, G., Vrtis, R.F., Roberg, K.A., Evans, M.D., Gangnon, R.E., Lemanske, R.F., Jr., and Gern, J.E. (2012). Increased H1N1 infection rate in children with asthma. Am. J. Respir. Crit. Care Med. *185*, 1275–1279.

Klose, C.S.N., Mahlakõiv, T., Moeller, J.B., Rankin, L.C., Flamar, A.L., Kabata, H., Monticelli, L.A., Moriyama, S., Putzel, G.G., Rakhilin, N., et al. (2017). The neuropeptide neuromedin U stimulates innate lymphoid cells and type 2 inflammation. Nature *549*, 282–286.

Korsunsky, I., Fan, J., Slowikowski, K., Zhang, F., Wei, K., Baglaenko, Y., Brenner, M., Loh, P.-R., and Raychaudhuri, S. (2018). Fast, sensitive, and accurate integration of single cell data with Harmony. bioRxiv. https://doi.org/10.1101/461954.

Kotas, M.E., and Locksley, R.M. (2018). Why innate lymphoid cells? Immunity *48*, 1081–1090.

Langmead, B., and Salzberg, S.L. (2012). Fast gapped-read alignment with Bowtie 2. Nat. Methods *9*, 357–359.

Levine, J.H., Simonds, E.F., Bendall, S.C., Davis, K.L., Amir, A.D., Tadmor, M.D., Litvin, O., Fienberg, H.G., Jager, A., Zunder, E.R., et al. (2015). Data-driven phenotypic dissection of AML reveals progenitor-like cells that correlate with prognosis. Cell *162*, 184–197.

Li, B., and Dewey, C.N. (2011). RSEM: accurate transcript quantification from RNA-seq data with or without a reference genome. BMC Bioinformatics *12*, 323.

Liao, Y., Smyth, G.K., and Shi, W. (2014). featureCounts: an efficient general purpose program for assigning sequence reads to genomic features. Bioinformatics *30*, 923–930.

Locksley, R.M. (2010). Asthma and allergic inflammation. Cell *140*, 777–783.

Lopez, R., Regier, J., Cole, M.B., Jordan, M.I., and Yosef, N. (2018). Deep generative modeling for single-cell transcriptomics. Nat. Methods *15*, 1053–1058.

Madamanchi, A. (2007). Beta-adrenergic receptor signaling in cardiac function and heart failure. McGill J. Med. *10*, 99–104.

Manis, J.P., Tian, M., and Alt, F.W. (2002). Mechanism and control of class-switch recombination. Trends Immunol. *23*, 31–39.

Martinez, V.G., and O'Driscoll, L. (2015). Neuromedin U: a multifunctional neuropeptide with pleiotropic roles. Clin. Chem. *61*, 471–482.

McLean, C.Y., Bristor, D., Hiller, M., Clarke, S.L., Schaar, B.T., Lowe, C.B., Wenger, A.M., and Bejerano, G. (2010). GREAT improves functional interpretation of cis-regulatory regions. Nat. Biotechnol. *28*, 495–501.

Molofsky, A.B., Savage, A.K., and Locksley, R.M. (2015). Interleukin-33 in tissue homeostasis, injury, and inflammation. Immunity *42*, 1005–1019.

Moriyama, S., Brestoff, J.R., Flamar, A.L., Moeller, J.B., Klose, C.S.N., Rankin, L.C., Yudanin, N.A., Monticelli, L.A., Putzel, G.G., Rodewald, H.R., and Artis, D. (2018). β_2-adrenergic receptor-mediated negative regulation of group 2 innate lymphoid cell responses. Science *359*, 1056–1061.

Mowat, A.M., and Agace, W.W. (2014). Regional specialization within the intestinal immune system. Nat. Rev. Immunol. *14*, 667–685.

Neill, D.R., Wong, S.H., Bellosi, A., Flynn, R.J., Daly, M., Langford, T.K., Bucks, C., Kane, C.M., Fallon, P.G., Pannell, R., et al. (2010). Nuocytes represent a new innate effector leukocyte that mediates type-2 immunity. Nature *464*, 1367–1370.

Nussbaum, J.C., Van Dyken, S.J., von Moltke, J., Cheng, L.E., Mohapatra, A., Molofsky, A.B., Thornton, E.E., Krummel, M.F., Chawla, A., Liang, H.E., and Locksley, R.M. (2013). Type 2 innate lymphoid cells control eosinophil homeostasis. Nature *502*, 245–248.

Oh-hashi, Y., Shindo, T., Kurihara, Y., Imai, T., Wang, Y., Morita, H., Imai, Y., Kayaba, Y., Nishimatsu, H., Suematsu, Y., et al. (2001). Elevated sympathetic nervous activity in mice deficient in alphaCGRP. Circ. Res. *89*, 983–990.

Painter, M.W., Davis, S., Hardy, R.R., Mathis, D., and Benoist, C.; Immunological Genome Project Consortium (2011). Transcriptomes of the

B and T lineages compared by multiplatform microarray profiling. J. Immunol. *186*, 3047–3057.

Picelli, S., Björklund, A.K., Faridani, O.R., Sagasser, S., Winberg, G., and Sandberg, R. (2013). Smart-seq2 for sensitive full-length transcriptome profiling in single cells. Nat. Methods *10*, 1096–1098.

Price, A.E., Liang, H.E., Sullivan, B.M., Reinhardt, R.L., Eisley, C.J., Erle, D.J., and Locksley, R.M. (2010). Systemically dispersed innate IL-13-expressing cells in type 2 immunity. Proc. Natl. Acad. Sci. USA *107*, 11489–11494.

Pulendran, B., and Artis, D. (2012). New paradigms in type 2 immunity. Science *337*, 431–435.

Ricardo-Gonzalez, R.R., Van Dyken, S.J., Schneider, C., Lee, J., Nussbaum, J.C., Liang, H.E., Vaka, D., Eckalbar, W.L., Molofsky, A.B., Erle, D.J., and Locksley, R.M. (2018). Tissue signals imprint ILC2 identity with anticipatory function. Nat. Immunol. *19*, 1093–1099.

Robinette, M.L., Fuchs, A., Cortez, V.S., Lee, J.S., Wang, Y., Durum, S.K., Gilfillan, S., and Colonna, M.; Immunological Genome Consortium (2015). Transcriptional programs define molecular characteristics of innate lymphoid cell classes and subsets. Nat. Immunol. *16*, 306–317.

Robinson, M.D., McCarthy, D.J., and Smyth, G.K. (2010). edgeR: a Bioconductor package for differential expression analysis of digital gene expression data. Bioinformatics *26*, 139–140.

Rodriguez, G., Ross, J.A., Nagy, Z.S., and Kirken, R.A. (2013). Forskolin-inducible cAMP pathway negatively regulates T-cell proliferation by uncoupling the interleukin-2 receptor complex. J. Biol. Chem. *288*, 7137–7146.

Rowe, R.K., and Gill, M.A. (2015). Asthma: the interplay between viral infections and allergic diseases. Immunol. Allergy Clin. North Am. *35*, 115–127.

Rydyznski, C.E., Cranert, S.A., Zhou, J.Q., Xu, H., Kleinstein, S.H., Singh, H., and Waggoner, S.N. (2018). Affinity maturation is impaired by natural killer cell suppression of germinal centers. Cell Rep. *24*, 3367–3373.e3364.

Schep, A.N., Wu, B., Buenrostro, J.D., and Greenleaf, W.J. (2017). chromVAR: inferring transcription-factor-associated accessibility from single-cell epigenomic data. Nat. Methods *14*, 975–978.

Schneider, C.A., Rasband, W.S., and Eliceiri, K.W. (2012). NIH Image to ImageJ: 25 years of image analysis. Nat. Methods *9*, 671–675.

Shao, J., and Sheng, H. (2010). Amphiregulin promotes intestinal epithelial regeneration: roles of intestinal subepithelial myofibroblasts. Endocrinology *151*, 3728–3737.

Soneson, C., and Robinson, M.D. (2018). Bias, robustness and scalability in single-cell differential expression analysis. Nat. Methods *15*, 255–261.

Spencer, S.P., Wilhelm, C., Yang, Q., Hall, J.A., Bouladoux, N., Boyd, A., Nutman, T.B., Urban, J.F., Jr., Wang, J., Ramalingam, T.R., et al. (2014). Adaptation of innate lymphoid cells to a micronutrient deficiency promotes type 2 barrier immunity. Science *343*, 432–437.

Stork, P.J., and Schmitt, J.M. (2002). Crosstalk between cAMP and MAP kinase signaling in the regulation of cell proliferation. Trends Cell Biol. *12*, 258–266.

Sui, P., Wiesner, D.L., Xu, J., Zhang, Y., Lee, J., Van Dyken, S., Lashua, A., Yu, C., Klein, B.S., Locksley, R.M., et al. (2018). Pulmonary neuroendocrine cells amplify allergic asthma responses. Science *360*, eaan8546.

Tanay, A., and Regev, A. (2017). Scaling single-cell genomics from phenomenology to mechanism. Nature *541*, 331–338.

Taylor, S., Huang, Y., Mallett, G., Stathopoulou, C., Felizardo, T.C., Sun, M.A., Martin, E.L., Zhu, N., Woodward, E.L., Elias, M.S., et al. (2017). PD-1 regulates KLRG1^{+} group 2 innate lymphoid cells. J. Exp. Med. *214*, 1663–1678.

Tordesillas, L., Berin, M.C., and Sampson, H.A. (2017). Immunology of food allergy. Immunity *47*, 32–50.

von Moltke, J., Ji, M., Liang, H.E., and Locksley, R.M. (2016). Tuft-cell-derived IL-25 regulates an intestinal ILC2-epithelial response circuit. Nature *529*, 221–225.

Wagner, A., Regev, A., and Yosef, N. (2016). Revealing the vectors of cellular identity with single-cell genomics. Nat. Biotechnol. *34*, 1145–1160.

Wallrapp, A., Riesenfeld, S.J., Burkett, P.R., Abdulnour, R.E., Nyman, J., Dionne, D., Hofree, M., Cuoco, M.S., Rodman, C., Farouq, D., et al. (2017). The neuropeptide NMU amplifies ILC2-driven allergic lung inflammation. Nature *549*, 351–356.

Welch, J.D., Kozareva, V., Ferreira, A., Vanderburg, C., Martin, C., and Macosko, E.Z. (2019). Single-cell multi-omic integration compares and contrasts features of brain cell identity. Cell *177*, 1873–1887.e1817.

Wolock, S.L., Lopez, R., and Klein, A.M. (2019). Scrublet: computational identification of cell doublets in single-cell transcriptomic data. Cell Syst. *8*, 281–291.e289.

Zeisel, A., Hochgerner, H., Lonnerberg, P., Johnsson, A., Memic, F., van der Zwan, J., Haring, M., Braun, E., Borm, L.E., La Manno, G., et al. (2018). Molecular architecture of the mouse nervous system. Cell *174*, 999–1014.e1022.

Zhang, Y., Liu, T., Meyer, C.A., Eeckhoute, J., Johnson, D.S., Bernstein, B.E., Nusbaum, C., Myers, R.M., Brown, M., Li, W., and Liu, X.S. (2008). Model-based analysis of ChIP-Seq (MACS). Genome Biol. *9*, R137.

STAR★METHODS

KEY RESOURCES TABLE

REAGENT or RESOURCE	SOURCE	IDENTIFIER
Antibodies		
rat anti-CD16/CD32 (2.4G2)	BD Biosciences	Cat# 553141; RRID: AB_394656
armenian hamster anti-CD3ε (145-2C11), APC	BioLegend	Cat# 100312; RRID: AB_312677
rat anti-CD5 (53-7.3), APC	BioLegend	Cat# 100626; RRID: AB_2563929
rat anti-CD19 (6D5), APC	BioLegend	Cat# 115512; RRID: AB_313647
rat anti-CD11b (M1/70), APC	BioLegend	Cat# 101212; RRID: AB_312795
rat anti-CD8 (53-6.7), APC	BioLegend	Cat# 100712; RRID: AB_312751
armenian hamster anti-CD11c (N418), APC	BioLegend	Cat# 117310; RRID: AB_313779
rat anti-Gr-1 (RB6-8C5), APC	BioLegend	Cat# 108412; RRID: AB_313377
armenian hamster anti-TCRγδ (eBioGL3), APC	Thermo Fisher Scientific	Cat# 17-5711-82; RRID: AB_842756
rat anti-CD170 (1RNM44N), eFluor 660	Thermo Fisher Scientific	Cat# 50-1702-80; RRID: AB_2574186
syrian hamster anti-KLRG1 (2F1), FITC	BioLegend	Cat# 138410; RRID: AB_10643582
rat anti-CD45 (30-F11), Alexa Fluor 594	BioLegend	Cat# 103128; RRID: AB_493715
rat anti-CD127 (A7R34), PE/CY7	BioLegend	Cat# 135014; RRID: AB_1937265
rat anti-CCR6 (29-2L17), BV421	BD Biosciences	Cat# 564736; RRID: AB_2738926
armenian hamster anti-TCRβ (H57-597), APC	Thermo Fisher Scientific	Cat# 17-5961-82; RRID: AB_469481
rat anti-NKp46 (29A1.4), PerCP/Cyanine5.5	BioLegend	Cat# 137609; RRID: AB_10642684
rat anti-CD90.2 (53-2.1), Brilliant Violet 605	BioLegend	Cat# 105343; RRID: AB_2632889
armenian hamster anti-FcεRI (Mar-1), Alexa Fluor 488	BioLegend	Cat# 134330; RRID: AB_2687239
rat anti-IgD (11-26c.2a), Alexa Fluor 594	BioLegend	Cat# 405740; RRID: AB_2565572
rat anti-GATA-3 (TWAJ), Alexa Fluor 488	Thermo Fisher Scientific	Cat# 53-9966-42; RRID: AB_2574493
rat anti-RORγt (B2D), PE	Thermo Fisher Scientific	Cat# 12-6981-82; RRID: AB_10807092
rat anti-IgD (11-26c.2a), Alexa Fluor 647	BioLegend	Cat# 405708; RRID: AB_893528
rat anti-IgD (11-26.2a), Alexa Fluor 594	BioLegend	Cat# 405740; RRID: AB_2565572
rat anti-CD138 (281-2), Alexa Fluor 647	BioLegend	Cat# 142525; RRID: AB_2566238
rat anti-GL7 (GL7), Alexa Fluor 488	Thermo Fisher Scientific	Cat# 53-5902-82; RRID: AB_2016717
rat anti-CD326 (EpCAM), eFluor 450	Thermo Fisher Scientific	Cat# 48-5791-82; RRID: AB_10717090
rat anti-CD3ε (17A2), Alexa Fluor 594	BioLegend	Cat# 152317; RRID: AB_2715809
rat anti-Podoplanin (eBio8.1.1), Alexa Fluor 488	BioLegend	Cat# 337005; RRID: AB_2161952
rat anti-CCL21/6Ckine (59106)	R&D Systems	Cat# MAB457; RRID: AB_2259799
rat anti-IL-13 (eBio13A), eFuor450	Thermo Fisher Scientific	Cat# 12-7133-41; RRID: AB_10852712
rat anti-IL-5 (TRFK5), eFuor450	BioLegend	Cat# 504311; RRID: AB_2563161
goat anti-IL-33	R&D Systems	Cat# AF3626; RRID: AB_884269
syrian hamster anti-KLRG1 (2F1)	BD Biosciences	Cat# 562190; RRID: AB_11154418
rat anti-CGRP	Sigma-Aldrich	Cat# C8198; RRID: AB_259091
rabbit anti-DCAMKL1	Abcam	Cat# ab31704; RRID: AB_873537
donkey anti-goat IgG, Alexa Fluor 647	Thermo Fisher Scientific	Cat# A-21447; RRID: AB_2535864
donkey Anti-Rat IgG, Cy3	Jackson ImmunoResearch	Cat# 712-166-153; RRID: AB_2340669
goat anti-syrian hamster IgG, Alexa Fluor 488	Jackson ImmunoResearch	Cat# 107-546-142; RRID: AB_2337479
goat anti-rabbit IgG, Alexa Fluor 647	Jackson ImmunoResearch	Cat# 111-606-144; RRID: AB_2338083
rat anti-T1/ST2 (DJ8), PE	mdbioproducts	Cat# 101001PE
goat anti-ChAT	Sigma-Aldrich	Cat# AB144P
Chemicals, Peptides, and Recombinant Proteins		
DAPI	Sigma-Aldrich	Cat# D9542
7-AAD	BD Biosciences	Cat# 559925

(*Continued on next page*)

Continued

REAGENT or RESOURCE	SOURCE	IDENTIFIER
Fixable Viability Dye eFluor 780	Thermo Fisher Scientific	Cat# 65-0865-14
UltraPure 0.5M EDTA, pH 8.0	Thermo Fisher Scientific	Cat# 15575020
Ovalbumin	Sigma-Aldrich	Cat# A5503
aluminum potassium sulfate dodecahydrate	Sigma-Aldrich	Cat# A7210-500G
α-CGRP	AnaSpec	Cat# AS-20681
Recombinant Mouse IL-17E Protein	R&D Systems	Cat# 1399-IL-025
DNase I, grade II, from bovine pancreas	Sigma-Aldrich	Cat# 10104159001
RPMI-1640	Thermo Fisher Scientific	Cat# 72400-047
Liberase TM	Sigma-Aldrich	Cat# 5401127001
Percoll Plus	Sigma-Aldrich	Cat# GE17-5445-01
10X Chromium Single Cell 3′ Kit	10X Genomics	Cat#120237
PicoPure RNA Isolation Kit	Thermo Fisher Scientific	Cat# KIT0204
iScript cDNA Synthesis Kit	Bio-Rad	Cat# 1708891
iTaq Universal SYBR® Green Supermix	Bio-Rad	Cat# 1725121
Recombinant Mouse IL-2 Protein	R&D Systems	Cat# 402-ML-020
Recombinant Mouse IL-7 Protein	R&D Systems	Cat# 407-ML-025
CellTrace Violet Cell Proliferation Kit	Thermo Fisher Scientific	Cat# C34557
O.C.T. Compound	Electron Microscopy Sciences	Cat# 62550-01
Triton X-100	Sigma-Aldrich	Cat# T8787
Normal Donkey Serum	Jackson ImmunoResearch	Cat# 017-000-001; RRID: AB_2337254
ProlongGold Antifade reagent	Thermo Fisher Scientific	Cat# P36930
TCL buffer (QIAGEN)	QIAGEN	Cat# 1031576
2-Mercaptoethanol	Sigma-Aldrich	Cat# M6250
GIBCO 2-Mercaptoethanol	Thermo Fisher Scientific	Cat# 21985023
Penicillin Streptomycin	Thermo Fisher Scientific	Cat# 15070063
Sodium Pyruvate	Thermo Fisher Scientific	Cat# 11360070
Nextera XT Sample Preparation Kit	Illumina	Cat#FC-131-1096
forskolin	STEMCELL technologies	Cat#72112
SQ22,536	TOCRIS	Cat# 1435
Cyclic AMP XP® Chemiluminescent Assay Kit	Cell Signaling technology	#8019
Deposited Data		
RNA-seq data	This paper	GEO: GSE124880
Experimental Models: Strains		
Mouse: BALB/cJ	Jackson Laboratory	Cat# JAX:000651; RRID: IMSR_JAX:000651
Mouse: B6.129S6-Calca < tm1Hku >	Brigham and Women's Hospital	Cat# RBRC04109; RRID: IMSR_RBRC04109
Oligonucleotides		
Reverse Transcription DNA oligonucleotide primer (RNase-free, 100 mM)	IDT	5′-AAGCAGTGGTATCAACGCAGAGTACT(30)VN-3′
SMARTER TSO (with LNA)	Exiqon	5′-AAGCAGTGGTATCAACGCAGAGTACrGrG+G-3′
PCR oligonucleotide primer	IDT	5′-AAGCAGTGGTATCAACGCAGAGT-3′
Calcrl-F	Sigma-Aldrich	5′-GCGTGAACCAAACAGACTTG-3′
Calcrl-R	Sigma-Aldrich	5′-TCATTCCAGCATAGCCATCC-3′
Ramp1-F	Sigma-Aldrich	5′-GGCTCTGCTTGCCATGG-3′
Ramp1-R	Sigma-Aldrich	5′-CCTTGAAGCGGCTGAGG-3′
Calca-F	Sigma-Aldrich	5′-TGCAGATGAAAGCCAGGG-3′
Calca-R-exon 5	Sigma-Aldrich	5′-CTTCACCACACCTCCTGATC-3′
Calca-R-exon 4	Sigma-Aldrich	5′-TGTTGAGGTCTTGTGTGTACG-3′
Calcr-F	Sigma-Aldrich	5′-CTACTTCTGGATGCTCTGCG-3′
Calcr-R	Sigma-Aldrich	5′-AGTGATGGCGTGGATAATGG-3′

(*Continued on next page*)

Continued

REAGENT or RESOURCE	SOURCE	IDENTIFIER
Gapdh-F	Sigma-Aldrich	5′-CTTTGTCAAGCTCATTTCCTGG-3′
Gapdh-R	Sigma-Aldrich	5′-TCTTGCTCAGTGTCCTTGC-3′
Software and Algorithms		
ImageJ	(Schneider et al., 2012)	https://imagej.nih.gov/ij/
GraphPad Prism	GraphPad Software	https://www.graphpad.com/scientific-software/prism/
FlowJo	TreeStar	https://www.flowjo.com/solutions/flowjo
STAR v2.6.0c	(Dobin et al., 2013)	https://github.com/alexdobin/STAR
10x Cell Ranger v2.1.1	10X Genomics	https://support.10xgenomics.com/single-cell/software/overview/welcome
RSEM v1.2.8	(Li and Dewey, 2011)	http://deweylab.github.io/RSEM/
edgeR v3.5.2	(Robinson et al., 2010)	https://gist.github.com/jdblischak/11384914
scvis v0.1.0	(Ding et al., 2018)	https://bitbucket.org/jerry00/scvis-dev/src/master/
LIGER v1.0	(Welch et al., 2019)	https://github.com/MacoskoLab/liger
Harmony v0.1.0	(Korsunsky et al., 2018)	https://github.com/immunogenomics/harmony
scVI v0.3.0	(Lopez et al., 2018)	https://github.com/YosefLab/scVI
Seurat v2.3.3	(Butler et al., 2018)	https://github.com/satijalab/seurat
Phenograph v0.99.1	(Levine et al., 2015)	https://github.com/JinmiaoChenLab/Rphenograph
densityCut v0.0.1	(Ding et al., 2016)	https://bitbucket.org/jerry00/densitycut_dev/src/master/
code for single-cell RNA-seq analysis	This paper	https://bitbucket.org/jerry00/mouse_small_intestine_immune_cell_atlas/src/master/

LEAD CONTACT AND MATERIALS AVAILABILITY

Further information and requests for resources and reagents should be directed to and will be fulfilled by the Lead Contact: Ramnik J. Xavier (xavier@molbio.mgh.harvard.edu).

This study did not generate new unique reagents.

METHOD DETAILS

Mice

BALB/cJ mice (Jax 000651) were obtained from the Jackson Laboratory. *Calca*$^{\Delta exon5}$ mice (B6.129S6-Calca < tm1Hku >) were kindly provided by Dr. Vijay K. Kuchroo (Brigham and Women's Hospital, Boston, Massachusetts, USA). Mice were housed in specific pathogen-free conditions and were used and maintained in accordance with the Institutional Animal Care and Use Committee (IACUC) protocol # 0055-05-15 (Broad Institute) and #18-001-XHP (Westlake University).

To induce allergic reaction to OVA, 6 to 7 weeks old mice were sensitized twice, two weeks apart, with 50 μg of OVA plus 1 mg of aluminum potassium sulfate adjuvant via intraperitoneal injection. Two weeks later, mice were orally administered with 50 mg of OVA on every other day for a total of five times. 1 μg of α-CGRP peptide was administered simultaneously when indicated. Mice were deprived of food for 3–4 hours in cages with wood chip bedding for limiting antigen degradation in the stomach before each intragastric challenge.

To activate ILC2s *in vivo*, 200 ng of IL-25 was intraperitoneally injected into 6-10 weeks old mice daily for two days. 1 μg α-CGRP was injected together as noted.

Isolation of cells from Peyer's patches (PPs)

Peyer's patches (PPs) were carefully dissected from the small intestine under a stereo microscope using a fine scissor, pierced once with a fine forcep. Tissues were digested in freshly made digestion buffer (RPMI-1640 containing 100 μg/ml Liberase TM and 50 μg/ml DNase I at 37°C on a roto-mixer. After 15 min, tissues were very gently mixed using a 1 mL pipette. The supernatant was collected and added to ice-cold MACS buffer (pH 7.4; PBS plus 2% FCS and 2mM EDTA). Pre-warmed (37°C) fresh digestion buffer was added to the remaining tissues. After rotation at 37°C for 15 min, the mixture was vigorously mixed using a 1ml pipette for 1 min. Supernatants from the two steps were combined and passed through 70 μm filters and stained for FACS (below).

Isolation of cells from the lamina propria (LP)

The small intestines were opened longitudinally and washed in ice-cold PBS. For scRNA-seq, roughly 0.5 cm of fragments from each of the distal, middle and proximal regions without visible PPs were collected. Epithelial cells were dissociated by tissue rotation in

pre-warmed (37°C) PBS containing 10 mM EDTA at 37°C for 15 min, followed by additional incubation on ice for 15 min. Tissues were then shaken vigorously. After washing twice with PBS containing 2% FCS, tissues were digested in pre-warned (37°C) digestion buffer at 37°C on a roto-mixer for 25 min. The supernatants were then passed through 70 μm filters and stained for FACS.

For experiments other than scRNA-seq, the entire small intestine was cut into 1 cm pieces after eliminating PPs. Epithelial cells dissociation was performed by stirring tissues in flasks containing PBS and 10 mM EDTA on a magnetic stirrer at 37°C two times for 15 min. After vortex, the tissue was stirred in pre-warmed (37°C) digestion buffer for 25 min at 37°C. The supernatant was passed through 100 μm filter. Leukocytes were further enriched by a 40%/70% Percoll gradient centrifugation before flow staining.

Flow cytometry and cell sorting

Cells were washed and suspended in MACS buffer (pH 7.4; PBS plus 2% FCS and 2 mM EDTA). Nonspecific antibody binding was blocked with CD16/CD32 (2.4G2) antibody for 15 min on ice. Cells were then stained with antibody cocktails for 30 min at 4°C. Lineage-positive cells were excluded for analyzing ILCs by staining for CD3ε (145-2C11), CD5 (53-7.3), CD19 (6D5), CD11b (M1/70), CD8 (53-6.7), CD11c (N418), Gr-1 (RB6-8C5), TCRγδ (eBioGL3 (GL-3, GL3)) and TCRβ (H57-597). To analyze mast cells, lineage-positive cells were excluded by staining for CD3ε, CD5, CD19, CD11c and SiglecF (E50-2440). For surface staining, antibodies for KLRG1 (2F1), CD45 (30-F11), CD127 (A7R34), CCR6 (29-2L17), NKp46 (29A1.4), CD90.2 (53-2.1), FcεRI (Mar-1), IgD (11-26c.2a) and ST2 (DJ8) were used. For intracellular staining, cells were fixed and permeabilized using the Foxp3 transcription factor staining buffer set, followed by staining with anti-GATA-3 (TWAJ) or anti-RORγt (B2D) antibodies. Dead cells were excluded with 7-AAD or Fixable Viability Dye eFluor 780. Flow cytometry was performed on Cytoflex (Beckman Coulter) and analyzed with FlowJo software. Sorting was performed with the SH800S Cell Sorter (Sony Biotechnology).

Droplet-based scRNA-seq

Single cells were captured via the GemCode Single Cell Platform using the GemCode Gel Bead, Chip and Library Kits (10X Genomics), according to the manufacturer's protocol. Briefly, flow-sorted cells were suspended in PBS containing 0.4% BSA, and loaded at 7,000 cells per channel. The cells were then partitioned into GemCode instrument, where individual cells were lysed and mixed with beads carrying unique barcodes in individual oil droplets. The products were subjected to reverse transcription, emulsion breaking, cDNA amplification, shearing, 5′ adaptor and sample index attachment. Libraries were sequenced on a HiSeq 2500 (Illumina).

Quantitative real-time PCR

RNA was isolated from 10,000 cells per sample using PicoPure RNA Isolation Kit, according to the manufacturer's protocol and reverse transcribed to cDNA with iScript cDNA Synthesis Kit. Gene expression was analyzed by quantitative real-time PCR on a ViiA7 System (Thermo Fisher Scientific) using iTaq Universal SYBR® Green Supermix with the primers listed in the Key Resources Table. Expression values were calculated relative to *Gapdh* detected in the same sample by qPCR.

ILC2 culture

Sort-purified intestinal KLRG1$^+$ ILC2s were incubated in complete RPMI medium (10% FCS, 10mM HEPES, 1mM sodium pyruvate, 10% FBS, 80 μm 2-mercaptoethanol, 2mM glutamine, 100U/ml penicillin, 100 μg/ml streptomycin), supplemented with 100 ng/ml IL-2 and 100 ng/ml IL-7 in 96-well round bottom plate at 37°C and 5% CO_2. If indicated, the culture was supplemented with 100 ng/ml IL-25. For the *in vitro* proliferation assay, cells from different mice were pooled and labeled with CellTrace Violet, and then cultured at 1,000-1,500 cells per well with 10 μg/ml α-CGRP for 60 hours. When indicated, 10 μM forskolin in DMSO was supplied and cells were cultured for 40 hours, or 1 μM SQ 22, 536 was added to cells for 1 hour before adding IL-25 for another 40 hours. For bulk RNA-seq, cells from individual mice were stimulated at 200 cells per well with 0.4 μg/ml α-CGRP for 3 hours. For bulk ATAC-seq, cells were stimulated with 0.4 μg/ml α-CGRP for 2 hours.

For assays that require large numbers of cells, intestinal ILC2s sorted from each of two mice were cultured in each well of 96-well plates with complete RPMI medium supplemented with 100 ng/ml IL-2 and 100 ng/ml IL-7 for 2 weeks. The cells were washed and rested in fresh cRPMI for 3 hours before adding stimuli.

To determine intracellular concentration of cAMP, 100,000 cells were stimulated with 100 ng/ml IL-25 or vehicle for 30 minutes and lysed with 50 μL lysis buffer (20mM Tris-HCl (pH 7.5), 100mM NaCl, 1mM Na2EDTA, 1mM EGTA, 0.8% Triton, 2mM sodium pyrophosphate, 1mM β-glycerophosphate, 1mM Na3VO4 and 1 μg/ml leupeptin). The concentrations of cAMP were determined via a chemiluminescent assay kit according to the manufacturer's protocol (Cell Signaling Technology).

To measure intracellular concentration of cytokines, 50,000 cells were stimulated with 10 ng/ml IL-25 for 8 hours before adding protein transport inhibitor cocktail for another 4 hours. The cells were then fixed and analyzed according to the intracellular flow staining protocol above.

Immunofluorescence staining and imaging

The small intestines were fixed in 2% PFA, embedded in O.C.T. Compound and sliced into 10 μm by frozen section. The slides were blocked with 0.1% Triton X-100, 2% FCS and donkey serum. The staining reagents incudes Alexa Fluor 594 anti-IgD (11-26.2a), Alexa Fluor 647 anti-CD138 (281-2), eFluor 450 anti EPCAM (G8.8), Alexa Fluor 594 anti-CD3ε (17A2), Alexa Fluor 488 anti-Podoplanin (eBio8.1.1 (8.1.1)), rat anti-CCL21/6 (59106), goat anti-IL-33 (polyclonal), hamster anti-KLRG1 (2F1), rat anti-CGRP (polyclonal), goat anti-ChAT (polyclonal), rabbit anti-DCAMKL1 (polyclonal), Alexa Fluor 647-donkey anti-goat IgG, Alexa Fluor 647 donkey

anti-goat IgG, Cy3 donkey anti-rat IgG, Alexa Fluor 488 goat anti-syrian hamster IgG (H+L), Alexa Fluor 647 goat anti-rabbit IgG (H+L) and DAPI. Slides were mounted with the ProlongGold Antifade reagent and examined with a ZEISS LSM 710 upright microscope using × 10, × 20 air or × 60 oil immersion lens. The images were analyzed with ImageJ.

Bulk RNA-seq

200 ILC2s from each condition were lysed in 10 ul TCL buffer plus 0.5% 2-Mercaptoethanol. Libraries were processed with SMART-Seq2 (Picelli et al., 2013) with at least three replicates per condition, and paired-end sequenced (38 bp × 2) with a 75 cycle Nextseq 500 high output V2 kit.

Reads were aligned to the mouse reference genome (NCBI 38, mm10) using STAR v2.6.0c (Dobin et al., 2013) with parameter '–twopassMode Basic' and otherwise default parameters, the number of reads mapped to each gene were calculated using featureCounts (Liao et al., 2014) from the Subread package, v1.6.2, and expression abundances were estimated using RSEM v1.2.8 (Li and Dewey, 2011). Differential gene expression analysis was performed on the count matrices output from featureCounts with edgeR R package v3.5.2 (Robinson et al., 2010) with default parameters.

Overall Expression analysis

We computed the Overall Expression (OE) of gene signatures in each sample as previously described (Jerby-Arnon et al., 2018). The procedure is based on the notion that the measured expression of a specific gene is correlated with its true expression (signal), but also contains a technical (noise) component. The latter may be due to various stochastic processes in the capture and amplification of the gene's transcripts, sample quality, as well as variation in sequencing depth. The OE of a gene signature is computed in a way that accounts for the variation in the signal-to-noise ratio across genes and cells.

Given a gene signature and a gene expression matrix E, where $E_{i,j} = \log2(TPM_{i,j}+1)$ and $TPM_{i,j}$ denotes the transcripts per million value of gene i in sample j, we first binned the genes into 50 expression bins according to their average expression across the samples. The average expression of a gene across a set of N samples was defined as: $\mathbb{E}_j[E_{ij}] = \sum_j(E_{ij}/N)$. Given a gene signature S that consists of K genes, with k_b genes in bin b, we sample 100 random S-compatible signatures for normalization. A random signature is S-compatible with a signature S if it consists of overall K genes, such that in each bin b it has exactly k_b genes. The OE of signature S in cell or sample j is then defined as:

$$OE_j = \frac{\sum_{i\in S} C_{ij}}{\mathbb{E}_{\tilde{S}}\left[\sum_{i\in \tilde{S}} C_{ij}\right]}$$

Where $\tilde{S}$ is a random S-compatible signature, and C_{ij} is the centered expression of gene i in sample j, defined as $C_{ij} = E_{ij} - \mathbb{E}[E_{ij}]$. Because the computation is based on the centered gene expression matrix C, genes that generally have a higher expression compared to other genes will not skew or dominate the signal. We used the software in https://github.com/livnatje/ImmuneResistance to compute the OE of gene signatures of interest.

Bulk ATAC-seq

ATAC-seq experiment was performed using a published protocol (Buenrostro et al., 2013) with minor modifications. Briefly, 2, 000 cells in 5 μL PBS, 17.3 μL H_2O and 25 μL of transposition buffer (66 mM Tris-acetate, 132 mM K-acetate, 20 mM Mg-acetate, 32% DMF, and 0.2% NP-40) were mixed and incubated at room temperature for 10 min. After adding 2.5 μL of Tn5 transposase to the reaction, the transposition was carried out at 37°C for 30 min with gentle shaking at 300 rpm and then purified with Zymo DNA Clean and Concentrator (Zymo Research). The library was amplified for 11 cycles, purified with Zymo DNA clean (Zymo Research), and sequenced on an Illumina Next-seq platform using 75 cycle Nextseq 500 high output V2 kit (Read 1: 38 cycles, Index 1: 8 cycles, Index 2: 8 cycles, Read 2: 38 cycles).

The reads were trimmed and aligned to the mouse reference genome (mm9) with Bowtie2 aligner (Langmead and Salzberg, 2012) using the option -X2000. Then, we discarded reads with alignment quality < Q30, improperly paired, mapped to the unmapped contigs, chrY, and mitochondria. Duplicates were removed using Picard tools (function MarkDuplicates, http://broadinstitute.github.io/picard/). MACSv2 peak caller (Zhang et al., 2008) (version: 2.1.1) was used to call accessible regions of open chromatin regions (ATAC-Seq peaks) with the following parameters (–nomodel –nolambda –keep-dup -call-summits). Peaks overlapping with ENCODE blacklisted regions were filtered out using BEDtools (function itersectBed). Peak summits were extended by ± 250 bp, and fragment counts in peaks were calculated using chromVAR (Schep et al., 2017) (version: 1.1.1). Peaks were allocated to genes using GREAT (McLean et al., 2010) (version: 3.0.0) with ''basal plus extension'' association rule with default parameters. Functional enrichment analysis was performed using GREAT (version: 3.0.0).

scRNA-seq data QC and pre-processing

Reads demultiplexing, alignment to the mm10 genome, unique molecular identifier (UMI) counting and collapsing were performed using Cell Ranger v2.1.1 (10x Genomics) to generate cell by gene UMI count matrices. After removing cells with less than 500 UMIs and high mitochondrial RNA UMIs (more than four times of the median number of mitochondrial UMIs across cells), we

obtained 36,797 cells from PP regions (15,939 cells from OVA-allergic mice and 20,858 cells from controls), and 21,270 cells from LP (11,405 cells from OVA-allergic mice and 9,865 cells from controls). 19,221 genes were retained after filtering genes expressed in less than five cells.

We expected batch effects in the data, because libraries were prepared and sequenced at different times, and because we used two sorting strategies to remove either IgD^+ Naive B cells or $CD19^+CD3^+$ cells. Moreover, the number of recovered cells varied across experiments; for example, we recovered 10,567, 6,439, 5,016, 4,571, and 10,204 cells from each of the five experiments for cells from PPs. We explored several possibilities to address these confounders. Two recent methods have been developed to align scRNA-seq data from different batches (Butler et al., 2018; Haghverdi et al., 2018). However, a cell type must be shared by all datasets for Seurat's CCA approach to correctly align cells (Butler et al., 2018), which is not appropriate for our case. mnnCorrect (Haghverdi et al., 2018) can merge datasets with private (distinct) cell types, but in our datasets where there were dozens of cell types, mnnCorrect successfully merged only some of these clusters, and failed to align cells from other clusters.

Principal Component Analysis (PCA) is typically used to extract a small number of features (principal components (PCs)) from a normalized gene-cell count matrix. These feature vectors were used for clustering analysis or as inputs for visualization. Unfortunately, in the presence of batch effects, some of the top features typically captured batch effects (Chen et al., 2011). Therefore, batch effects could not be removed by discarding the features with small eigenvalues in PCA.

To help address these batch effects, we took an alternative approach, where we projected the scRNA-seq data to a reference dataset consisting of microarray measurements of immune cells from 276 samples (Heng et al., 2008). Specifically, we first did PCA on the microarray data and extracted the first 101 eigenvectors. We discarded the first eigenvector as the corresponding first PC was correlated with batch information in the microarray data. We next projected the scRNA-seq data to the 100-dimensional space spanned by the eigenvectors (PCs 2-101) from the microarray data. The coordinates of cells in the 100-dimensional space were used for clustering and as inputs of scvis. We named our batch-correction method reference-projection.

Benchmarking different batch correction approaches

We benchmarked reference-projection to three other recent proposed batch-correlation methods: LIGER (Welch et al., 2019), Harmony (Korsunsky et al., 2018), and scVI (Lopez et al., 2018). For LIGER, we followed the standard pipeline and choose 20 factors. For Harmony, we used a theta of four and 50 principal components. For scVI, we used ten dimensional latent variables and three hidden layers (each with 512 units) for both the encoders and decoders. Phenograph (Levine et al., 2015) clustering the batch-corrected data from each method produced 44, 34, and 28 clusters, respectively. We next quantitively and qualitatively compared the results produced by each method.

We assessed the performance of the methods by two criteria. **First**, for the data from a specific batch, we asked if the partitions from clustering this dataset in isolation and from clustering the merged dataset after batch-correction were similar, with similarity measured by normalized mutual information (NMI), with the maximum NMI = 1 if the two partitions are identical, and NMI = 0 if the two partitions were independent. **Second**, we asked if cells in each cluster were well-mixed across different datasets and batches. To measure the mixture, for each dataset from a batch, we first computed the fractions of cells in each cluster, and then computed the Pearson correlation coefficient between the cell fraction vectors from each dataset (batch). Here, we interpreted the results in the context of our experimental design, where the gating strategies and tissue sources (LP or PP) were chosen to alter cell compositions of obtained cells between some batches. Specifically, cells from experiment 1-3 were obtained using the same gating strategy (removing naive B cells) and cells from experiment 4-5 were obtained from removing $CD19^+$ B cells and $CD3^+$ T cells. Experiment 1-5 cells were from Payer's patches and experiment 6-7 cells were from lamina propria.

Based on the first clustering concordance measure, our reference-projection method consistently outperformed LIGER (Figure S1D), and outperformed Harmony and scVI for the first five datasets and performed slightly worse for the last two datasets. Based on the second mixing measure, the Pearson correlations between cell composition vectors from datasets of the same gating strategy were high (Figure S1E). Although the correlations between cell composition vectors from clustering the merged datasets using Harmony (Figure S1E) were generally the highest, these included those between datasets of different gating strategies, suggesting higher background noise in the Harmony results. The other three methods performed comparably on data from experiments 6 and 7 (Pearson correlation coefficients of 0.93), LIGER performed slightly worse on experiment 4 and 5 (Pearson correlation coefficients of 0.94), and for experiments 1-3, LIGER performs the best, followed by reference-projection, and scVI performed the worst.

Finally, we visually inspected the clustering results on the batch-corrected datasets. LIGER and Harmony tends to split big clusters, e.g., naive T cells (cluster 1 in Figure 1B) and naive B cells (cluster 2 in Figure 1B), while merging some small clusters (e.g., gamma-delta T cells, cluster 17 and 38 in Figure 1B) to other clusters. The results of scVI and reference-projection are more consistent with each other. We also compared the NMIs between the partitions from clustering datasets that were batch-corrected in different ways. scVI and reference-projection had the highest concordance (NMI = 0.8). However, as the clustering algorithm divided the scVI results into only 28 clusters, some similar clusters such as the two germinal cell B cells (cluster 9 and 10 in Figure 1B) were in the cell cluster, similarly for other cells such as ILC1 and NK cells (cluster 11 and 8 in Figure 1B).

In summary, compared to other state-of-the-art batch-correction methods, the reference-projection method retained the structures in individual datasets (with high concordance between the partitions from clustering the merged dataset and the partitions from clustering individual datasets independently) and ensured that cells from different datasets were well mixed (with high Pearson correlations). It helped us identify different types of cells from mouse small intestines for down-stream analyses.

scRNA-seq clustering of PP cells

We used the Louvain community detection algorithm (Blondel et al., 2008; Levine et al., 2015) to cluster cells from Peyer's patch regions. As the Louvain clustering algorithm tends to miss some small clusters, we used densityCut (Ding et al., 2016) to find the likely cluster centers. For each center, we changed the edge weights (w′) connecting the cluster center to its neighbors to (w′) = 2*kw*, where *k* is the number of nearest neighbors in the *k*-nearest neighbor (*k*-NN) graph, and *w* is the original edge weight of an edge. Louvain clustering on this edge re-weighed graph produced 46 clusters.

Next, we assessed the robustness of the cell to cluster assignment. For each cluster and each batch, we computed the 'bulk' gene expression profile of the cells from a given batch in the cluster. The 'bulk' gene expression profile for a set of cells is computed by first taking the sum of the gene expression vectors from these cells, where the gene expression vector of a cell was the raw UMI count vector, one element for a gene. The dimensionality of a gene expression vector was the number of genes. To make the bulk gene expression vectors from different sets of cells comparable, a bulk gene expression vector was normalized by dividing the total number of UMIs from all the cells used in computing that bulk gene expression vector, and further multiplying by 10^4 and finally taking the log transform (adding one before the log transformation to make all the elements of the bulk vector positive). Then, for each cell, we computed its Pearson correlation coefficient with the "bulk" profile for each cluster. We denote the maximum correlation between a cell *x* and the bulk profiles of cluster *i* (from different batches) as c_i. If cell *x* is originally assigned to cluster *j*, and $c_j < 0.9c_k$, then we reassign cell *x* to cluster *k*. Only ~0.26% (97 of 36,797) cells were re-assigned to clusters different from their original assignment. We also tested whether two clusters should be merged, if there are no more than 10 significantly differentially expressed genes between them (with differential expression estimated with the Wilcoxon rank-sum test in the package Seurat (Butler et al., 2018)). However, none of the 46 clusters required merging by this criterion.

Clustering cross-validation of PP cells

We performed a 10-fold cross validation analysis on the PP data to evaluate the quality of the clustering. We partitioned the PP data into ten approximately equal size sets, and trained a *k*-nearest neighbor (*k*-NN) classifier (we used a small $k = 11$ as some clusters are small, e.g., 17 cells in cluster 46) on nine folds of data, leaving one-fold of data for testing. We repeated this training and testing scheme ten times such that all the data points were used for testing only once.

The *k*-NN classifiers had a high overall accuracy of 97.2%. Classification accuracy varied for cells from different clusters, with those from cluster 39 having the lowest accuracy of 65.6%. Cluster 39 consisted of a mixture of low-quality plasma B cells and cell doublets (macrophage and epithelial cell doublets). A subgroup of cells expressed plasma B cell marker genes, such as *Jchain* and *Mzb1*, but had a relatively small number of UMIs per cell compared to the cells from the plasma cell Cluster 20 (Figure S1F). Some of these low-quality plasma B cells also had high mitochondrial UMI ratios. Another subset of cells in Cluster 39 expressed both epithelial cell markers (e.g., *Epcam* and *Krt8*) and macrophage marker genes (e.g., Lyz1 and Lyz2). These cells had a very large number of UMIs per cell (Figure S1F) and likely represented potential macrophage and epithelial cell doublets. Notably, although the number of cells in each cluster was extremely unbalanced (e.g., 6,948 cells in cluster 1 but only 17 cells in cluster 46), the classification accuracies were largely uncorrelated with the number of cells in each cluster.

Cluster annotation and filtering of PP cells

We next used MAST (Finak et al., 2015) to identify significantly upregulated marker genes for each of the 46 clusters, accounting for batch (experimental dates) and the scaled number of detected genes in each cell as covariants (Soneson and Robinson, 2018). Based on known function of the marker genes, we annotated 6 major cell lineages and groups: T cells, B cells, dendritic cells, ILCs, myeloid cells, and stromal cells.

We conservatively excluded from further analyses the smallest clusters (< 0.05% of all cells) and several ambiguous clusters that we could not confidently assign with cell identities. We note that the small clusters may be biologically valid, but the small number of cells limits our ability to further study them here. For example, the top markers of cluster 45 (18 cells) included *Dntt*, *Rag1, Chrna9*, *Tctex1d1*, *Arpp21*, which are highly expressed in progenitors of T cells at the double-positive stage in Immgen (Heng et al., 2008; Painter et al., 2011). Cluster 46 (17 cells) may consist of lymph node lymphatic endothelial cells, as they expressed their known marker genes such as *Lyve1*, *Prox1*, and *Cp*. Experimental validations are required for confidently including them in the downstream analyses. Cells in Cluster 34 (100 cells) from PP, expressed both pDC and myeloid gene markers. Only two marker genes (*Gtf2a1* and *2310001H17Rik*) overlapped between Cluster 34, and either of its adjacent clusters in scvis, clusters 6 and 22 (Figure 1B). *Gtf2a1* was expressed lowly in about 25% of the cluster 34 cells and *2310001H17Rik* was expressed in several other cell types, such as T cells and neutrophils. We annotated cluster 34 as 'Unresolved'. Cluster 18 and cluster 37 were also annotated as 'Unresolved' based on similar analysis. Cluster 40 cells expressed macrophages marker gene like *Lyz2*. Compared to the macrophage cluster (cluster 22), cluster 40 cells expressed higher amounts of *C1qa, C1qb*, and *C1qc*. However, Cluster 40 cells had less UMIs per cells (Figure S1F) than Cluster 22 cells. We also labeled Cluster 40 as 'Unresolved'.

We further removed clusters enriched for doublets. To this end, we analyzed PP cells with Scrublet (Wolock et al., 2019), identifying clusters 29, 41, and 43 cells with high doublet scores, together accounting for 0.63% (232 of 36,797) of the PP cells. Cluster 42 cells also had high doublet scores, albeit lower than these other three clusters, and may be further potential doublets.

Clustering LP cells

We used the 35,691 PP cells that were both confidently assigned to clusters in the cross-validation above and had a *k*-NN probability greater than 0.5, to train a *k*-NN classifier ($k = 11$), and used it to classify the 21,270 LP cells. The vast majority of LP cells (97.4%, 20,724 / 21,270) were assigned to 42 of the 46 clusters with *k*-NN probability greater than 0.5. We refined the clustering as done for the Peyer's patch data but only for the cells with *k*-NN probabilities less than 0.5. This reassigned only 0.12% (26 / 21,270) cells. 34 of the 42 clusters had > 15 cells. To find potential LP-specific clusters (cell types that were only observed in LP), we concatenated the data from PPs and LP and then clustered the merged data. Of the clusters enriched in cells from LP (more than three times the number of cells from LP than PPs), two consisted of mast cells and three of plasma B cells. One of these clusters had cells with a low number of UMIs per cell without apparent marker genes. One LP-enriched cluster consisted of fibroblasts that expressed marker genes, such as *Col15a1*, *Ecm1*, and *Col6a5*.

Ten-fold cross validation of the 21,223 LP cells in 34 clusters with > 15 cells showed 94.59% accuracy for all cells. Cells from three small clusters 5, 19, and 42 (32, 41, and 19 cells, respectively) had relatively low cross-validation accuracies of 0.41, 0.56, and 0.53, respectively. Overall, ~93.70% (19,886 / 21,223) were assigned robustly (correctly classified in cross-validation and with *k*-NN probabilities greater than 0.5).

Cellular composition changes

As different gating strategies (IgD^{low} or $CD3^{-}CD19^{-}$) directly influenced the frequencies of T and B cells, which subsequently affected the proportions of all other cell types, we separately quantified cell compositions in B cells, T cells, and other non-TB cell types. In addition, for analyzing changes in the composition of B cell subsets, we did not include cells from the experiments with $CD3^{-}CD19^{-}$ sorting.

Moreover, because of random sampling and unevenness of recovery of cells across mice, considering the number of cells (and not only fractions) is a critical part of the testing framework. The accuracy of estimating a cell type's proportion in the population increases as we have more cells. For mice with relatively few cells recovered overall, the estimates could be poor, and we want our test to be aware of these overall lower counts. Statistical tests based on ratios alone (proportions), discard the information about the total number of cells used in calculating the ratios and as a result treat the ratio from each mouse equally, irrespective of the underlying cell numbers. We thus used a framework based on the negative binomial regression model and the Wald test.

We used the negative binomial regression model to assess cell composition changes between PPs and LP using cells in homeostasis (Figure 1C). We used spatial information (PP or LP) as a covariate and the total number of analyzed cells from each mouse as an offset variable. The P value for the significance of location information (LP) on a cell type was also assessed using the Wald test on the regression coefficient.

We performed similar analyses to assess cell composition changes between PPs and LP using all data, with the negative binomial regression model with treatment (OVA or PBS) and location (PP or LP) as covariates (Figure S1M). The total number of analyzed cells (e.g., the total number of B cells when quantifying B cells variations) from each mouse was used as an offset variable. The P value for the significance of location (LP) on a cell type was assessed using the Wald test on the regression coefficient. Generally, the results for differences between LP and PP were consistent with those obtained for homeostasis data, with two minor exceptions: cluster 6 (pDCs) was not significantly different between regions when considering both OVA and PBS treated mice, but cluster 24 (DC ($CD103^{-}$ C1)) was significant.

To assess differences in composition due to treatment (Figure 2B, top), we used the same framework with treatment (OVA or PBS) and location information (PP or LP) as covariates. The total number of analyzed cells (e.g., the total number of T cells when quantifying T cells variations) from each mouse was used as an offset variable. The P value for the significance of treatment (OVA) on a cell type was assessed using the Wald test on the regression coefficient.

Finally, we also tested cell composition changes between PBS and OVA treated mice for each of the PP and LP datasets separately, using the negative binomial regression model with only treatment as the covariate (Figure 2B, middle and bottom).

Cell sampling frequencies

To estimate the number of required cells such that we have the power to recover rare cell types, we used the online tool: http://satijalab.org/howmanycells. The method assumes that the probability of observing at least N cells of a cell type in a sample of size K can be modeled by the cumulative distribution function of a negative binomial NBcdf(K; N, p), where p is the relative abundance of this cell type.

Topic modeling

In the topic modeling analysis, one gene can belong to multiple topics (programs), and its relative relevance in the topic is reflected by a weight. A cell is represented as a weighted mixture of topics, where the weights reflect the importance of the corresponding topic (program) in the cell. A single gene from a topic may not be sufficient to highlight the identified cellular program nor may its entire expression signal be relevant to the program. Thus, unlike the simple averaging or aggregation of expression for genes in an expression signature, in topic models we learn how different genes contribute differently to the topic, how a topic can contribute to cells to different extents, and (in contrast to cell type specific markers), how a topic can be relevant across cells of different types. As a result, topic modeling is more nuanced in how it handles both cells and genes.

To help guide LDA to find the informative topics, we learned multiple topic models for each subgroup of cells separately. (We had found that topic modeling of all subsets together mostly identifies cell type programs; data not shown.) Specifically, we used the FitGoM() function from the CountClust R package (Dey et al., 2017) to fit LDA topic models to the UMI counts (Bielecki et al., 2018) for cells belonging to each major identified cell type from the LP and PP regions. This resulted in 12 models, two for each of the following cell types: T cells (583 LP cells, 12,187 PP cells), DC cells (3,738 LP cells, 3,530 PP cells), B cells (5,648 LP cells, 7,376 cells), ILC cells (5,484 LP cells, 9,396 PP cells), myeloid cells (1,825 LP cells, 579 PP cells), and stromal cells (90 LP cells, 443 PP cells). Genes starting with 'Rpl' or 'Rps' were removed from the counts matrix prior to fitting the topic models, leaving a total of 19,108 genes included in each count matrix. The number of topics to fit and the tolerance value are required to run FitGoM() function. Thus, for each cell type and region, we fit a range of K and then used compGoM() to compute the Bayesian Information Criterion (BIC) the estimated likelihood, from which we calculated the Akaike Information Criterion (AIC). Our final choice of K value was primarily guided by the BIC curve; we aimed to choose a K at which the BIC was minimal, or decreasing less quickly. We set the tolerance value to 0.1. The top genes to highlight for each topic were selected using the ExtractTopFeatures() function.

Statistical analysis

Mice from which we failed to isolate a sufficient number of live cells for downstream analysis were excluded. Prism 7 (GraphPad Software) was used to perform two-tailed t test and Fisher's exact test as indicated (except for RNA-seq data for which we use R for statistical analysis). P values from multiple comparisons were FDR-adjusted in R.

DATA AND CODE AVAILABILITY

The scRNA-seq data and bulk RNA-Seq data generated during this study are available at NCBI Gene Expression Omnibus through accession number GEO: GSE124880. Processed scRNA-seq data are also available from Single Cell Portal: https://portals.broadinstitute.org/single_cell/study/fasi-immune-mouse-small-intestine

Custom code and software packages are available freely from Bitbucket: https://bitbucket.org/jerry00/mouse_small_intestine_immune_cell_atlas/src/master/

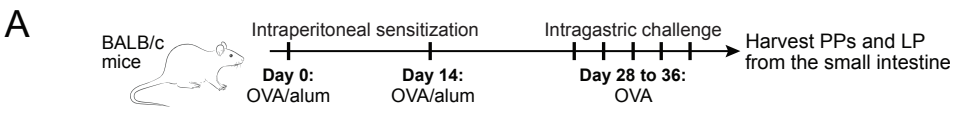
Immunity, Volume *51*

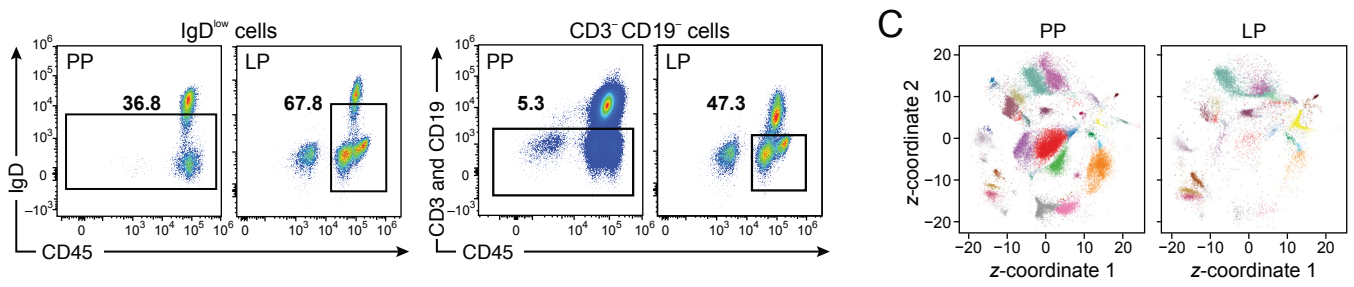
Supplemental Information

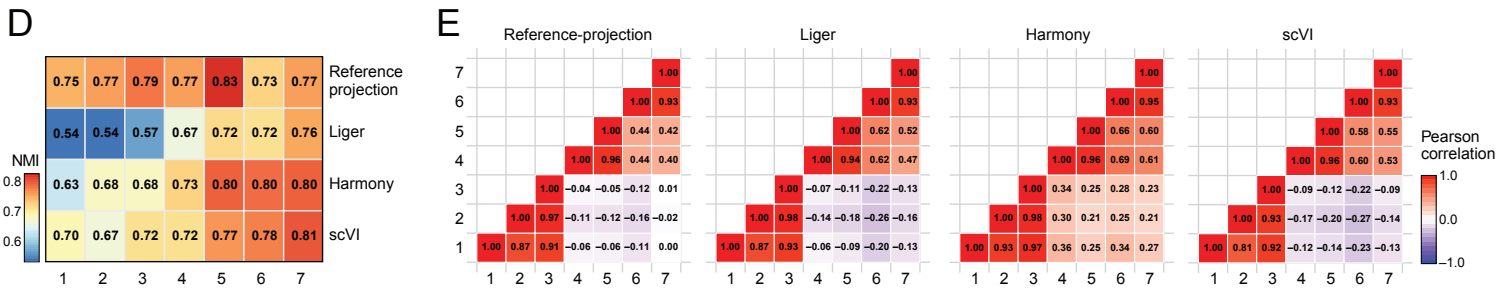
Transcriptional Atlas of Intestinal Immune Cells Reveals that Neuropeptide α-CGRP Modulates Group 2 Innate Lymphoid Cell Responses

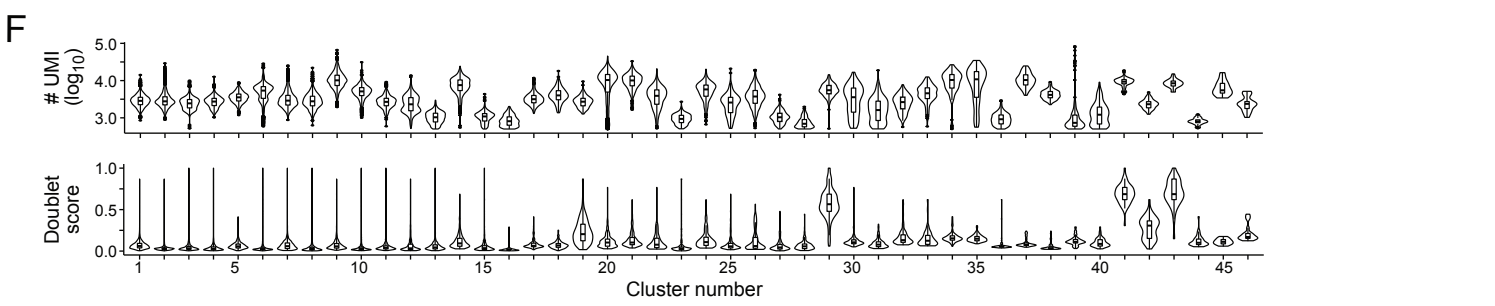
Heping Xu, Jiarui Ding, Caroline B.M. Porter, Antonia Wallrapp, Marcin Tabaka, Sai Ma, Shujie Fu, Xuanxuan Guo, Samantha J. Riesenfeld, Chienwen Su, Danielle Dionne, Lan T. Nguyen, Ariel Lefkovith, Orr Ashenberg, Patrick R. Burkett, Hai Ning Shi, Orit Rozenblatt-Rosen, Daniel B. Graham, Vijay K. Kuchroo, Aviv Regev, and Ramnik J. Xavier

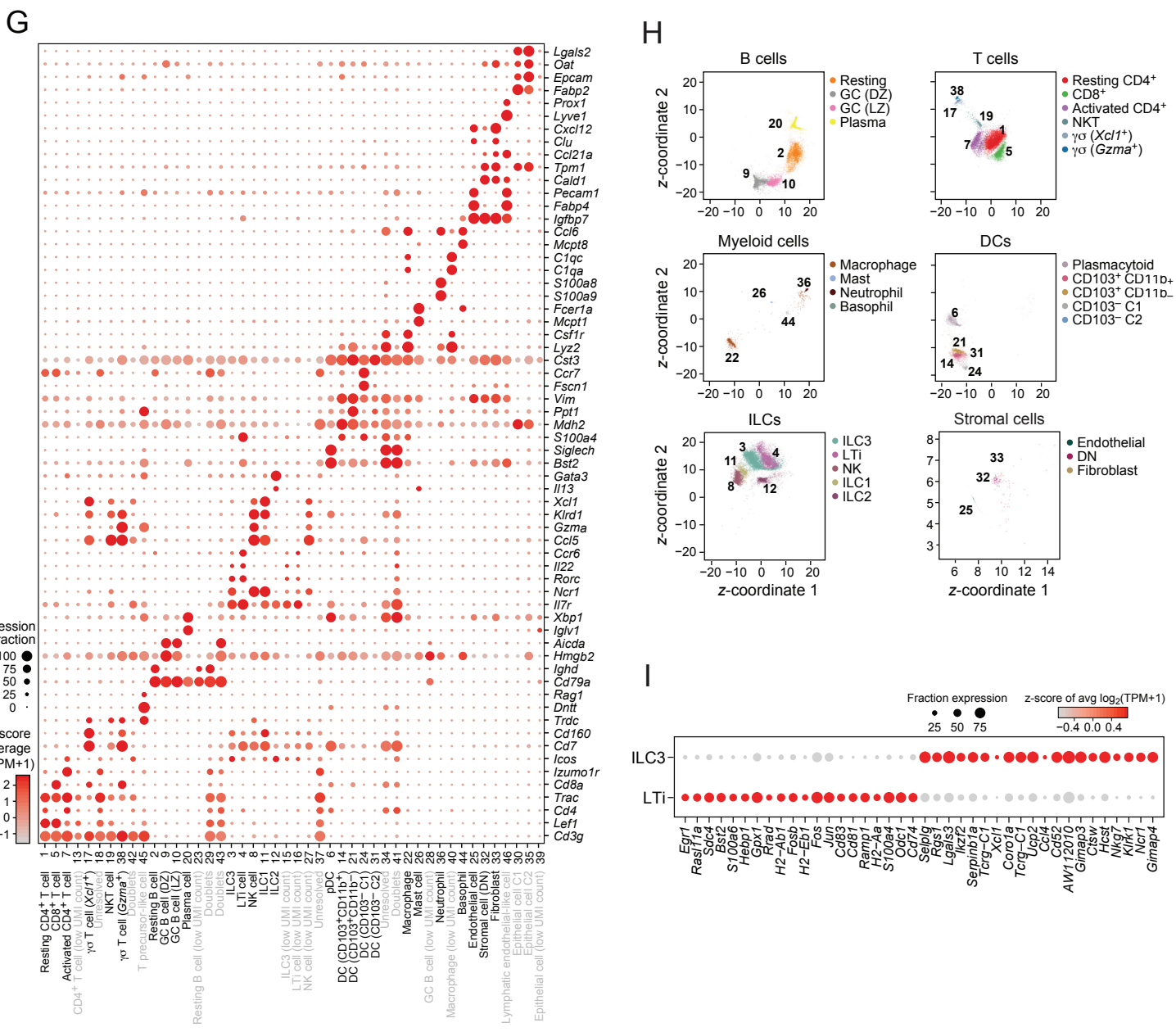
Figure S1

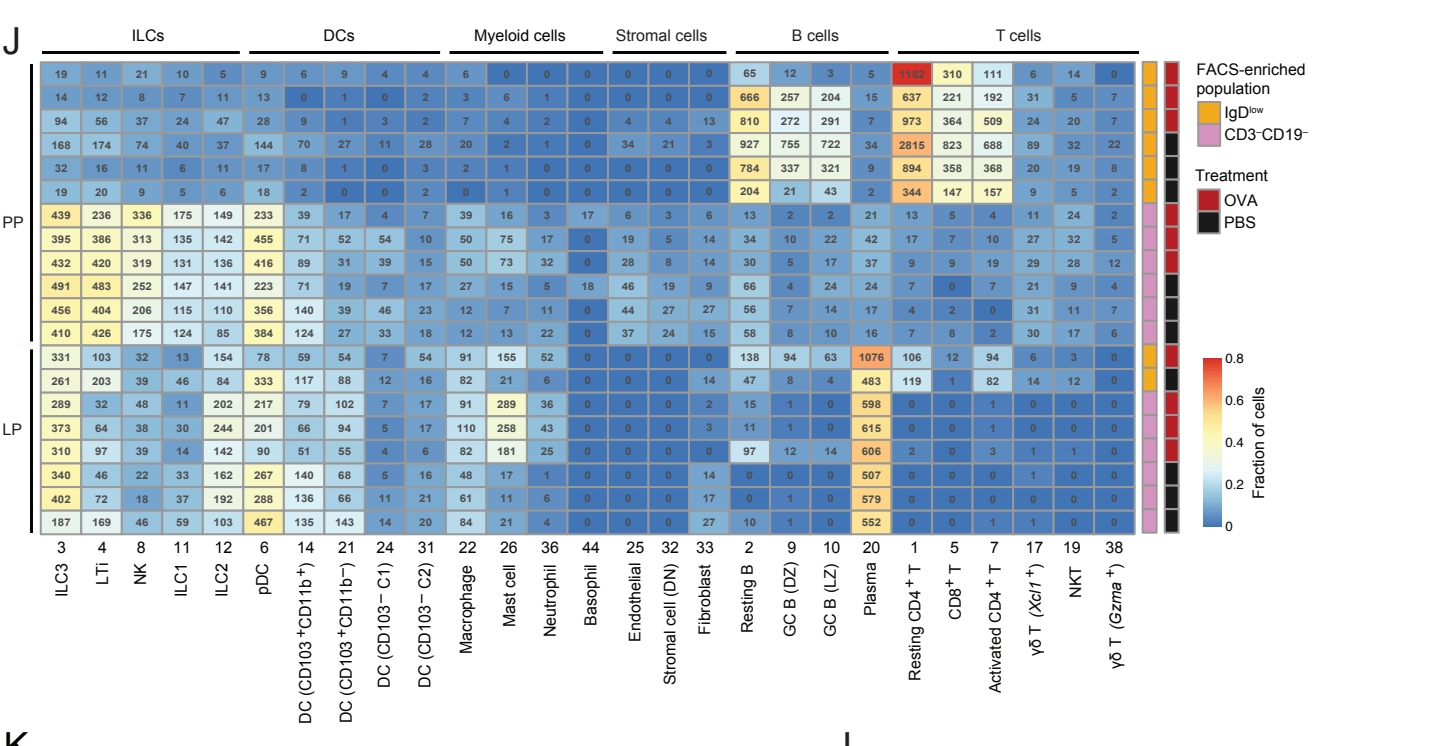

A
BALB/c mice
Intraperitoneal sensitization
Day 0: OVA/alum
Day 14: OVA/alum
Intragastric challenge
Day 28 to 36: OVA
Harvest PPs and LP from the small intestine

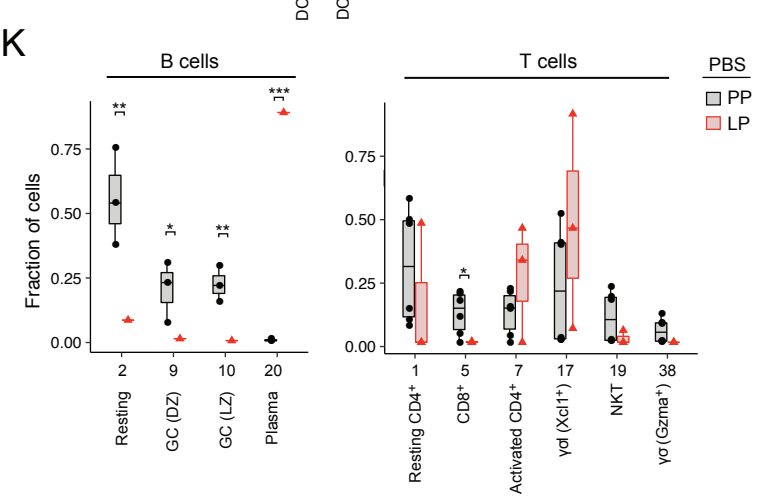

B
IgD^low cells
CD3⁻CD19⁻ cells
PP
LP
36.8
67.8
5.3
47.3
IgD
CD3 and CD19
CD45
C
PP
LP
z-coordinate 2
z-coordinate 1

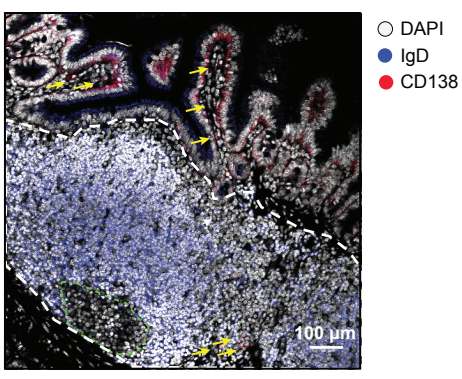

D
NMI
Reference projection
Liger
Harmony
scVI
E
Reference-projection
Liger
Harmony
scVI
Pearson correlation


F
UMI (log10)
Doublet score
Cluster number


G
H
B cells
Resting
GC (DZ)
GC (LZ)
Plasma
T cells
Resting CD4+
CD8+
Activated CD4+
NKT
γσ (Xcl1+)
γσ (Gzma+)
Myeloid cells
Macrophage
Mast
Neutrophil
Basophil
DCs
Plasmacytoid
CD103+ CD11b+
CD103+ CD11b−
CD103− C1
CD103− C2
ILCs
ILC3
LTi
NK
ILC1
ILC2
Stromal cells
Endothelial
DN
Fibroblast
Expression fraction
Z-score of average log2(TPM+1)
I
Fraction expression
z-score of avg log2(TPM+1)
ILC3
LTi


J
ILCs
DCs
Myeloid cells
Stromal cells
B cells
T cells
PP
LP
FACS-enriched population
IgD^low
CD3⁻CD19⁻
Treatment
OVA
PBS
Fraction of cells


K
B cells
T cells
PBS
PP
LP
Fraction of cells
Resting
GC (DZ)
GC (LZ)
Plasma
Resting CD4+
CD8+
Activated CD4+
γδ (Xcl1+)
NKT
γσ (Gzma+)


L
DAPI
IgD
CD138
100 μm

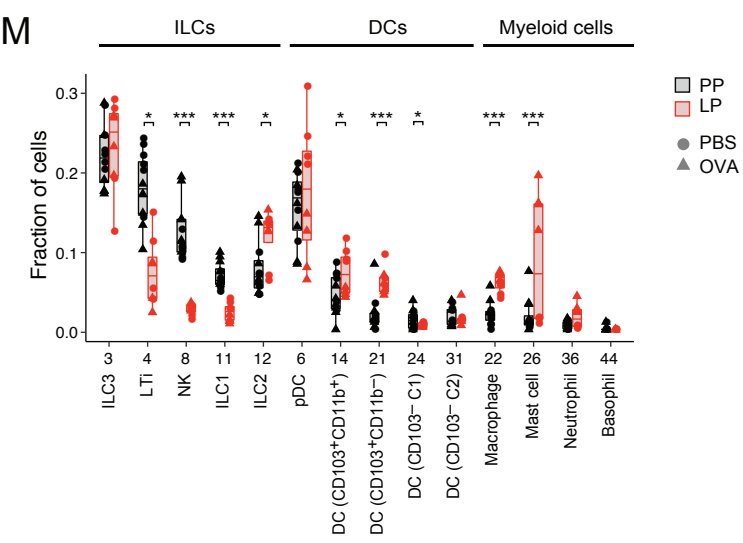

M
ILCs
DCs
Myeloid cells
PP
LP
PBS
OVA
Fraction of cells

Figure S1. FACS, single-cell expression and IF staining analysis of intestinal immune cells, related to Figure 1

(**A**) Experimental overview.

(**B**) Depletion of common cell types by FACS. Shown are representative FACS plots for sorting lgD^{low} cells (left) or $CD3^{-}CD19^{-}$ cells (right) from PP and LP regions. $CD45^{-}$ cells were not included in LP.

(**C**) An LP and PP cell atlas. A 2D embedding as in **Figure 1B**, but showing separately only the 36,797 cells from PP regions (left) or the 21,270 cells from LP (right).

(**D,E**) Comparison of batch correction methods. (D) Normalized mutual information (NMI, color bar) between clustering results from each dataset (columns) analyzed independently and the merged dataset generated using different batch-correction methods (rows) (**STAR Methods**). (E) Pearson correlation coefficients between the cell fraction vectors of the proportion of cells in clusters from two dataset (rows, columns, **STAR Methods**). Experiment 1-3: naive B cells were removed; Experiment 4-5: $CD19^{+}$ B cells and $CD3^{+}$ T cells were removed. The cells were collected from Peyer's patches (experiment 1–5) or lamina propria (experiment 6–7).

(**F**) Cluster quality measures. Top: distribution of number of UMIs (*y* axis, $\log_{10}$-transformed) in both LP and PP cells in each cluster from **Figure 1B** (x axis). Bottom: distribution of doublet scores (y axis, **STAR Methods**) of PP cells in each cluster from **Figure 1B** (x axis).

(**G**) Differentially expressed genes. For representative differentially expressed genes (rows) across clusters (columns), shown is the fraction of cells in the cluster that express a gene (dot size) and the z-score of the mean expression of that gene in the cluster (color; z-score of average $\log_2$(TPM+1)). The inferred identities were labeled at the bottom with those excluded from the downstream analyses are in grey.

(**H**) Clusters of specific cell types in the atlas. A 2D embedding as in **Figure 1B**, but showing separately only the cells in each cell lineage or group as labeled.

(**I**) Differentially expressed genes between ILC3 and LTi. Fraction of cells in the cluster that express a gene (dot size) and the z-score of the mean expression of that gene in those cells that express it in the cluster (color; z-score of average $\log_2$(TPM+1)).

(**J**) Number and proportion of cells detected in each mouse in the study. Fraction (color bar, out of all cells from that mouse) and number of cells from each of the 27 cell clusters (columns) in each individual mouse (rows), along with its treatment (Black/red: OVA/PBS) and enrichment strategy (purple/orange: IgD^{low}/$CD3^{-}CD19^{-}$).

(**K**) Tissue distribution of B (left) and T (right) cells between LP and PP in homeostasis. Proportion (*y* axis) of each cell type (*x* axis) in LP (red) and PP (black) regions of mice treated with PBS. Points: independent mice (n=3 for B cells, n=6 for T cells); Boxplots denote IQR as in **Figure 1C**.

(**L**) Differential distribution of plasma cells and GC B cells. Representative IF image of the small intestines of wild type mice. White dashed line: PP region; Green dashed line: GC area; arrow: $CD138^{+}$ plasma cell; scale bar, 100 μm.

(**M**) Tissue distribution of non-T and non-B immune cells in both homeostatic and inflammatory conditions. Proportion (*y* axis) of each cell type in LP (red, n=8 mice) and PP (black, n=12 mice) regions of mice treated with PBS (dots) or OVA (triangles). Points: independent mice; Boxplots: medians and interquartile ranges (IQR). Whiskers: lowest datum within 1.5 IQR of the lower quartile and the highest datum within 1.5 IQR of the upper quartile. *$p < 5\times10^{-2}$, **$p < 3\times10^{-8}$, ***$p < 3\times10^{-9}$, Wald test (K, M) for difference in cell composition accounting for cell counts (counts shown in **Figure S1J**). Data are representative of seven (B) or two (L) independent experiments, or are from seven (C, D, E, F, G, H, J, M) or three (I, K) independent experiments.

Figure S2

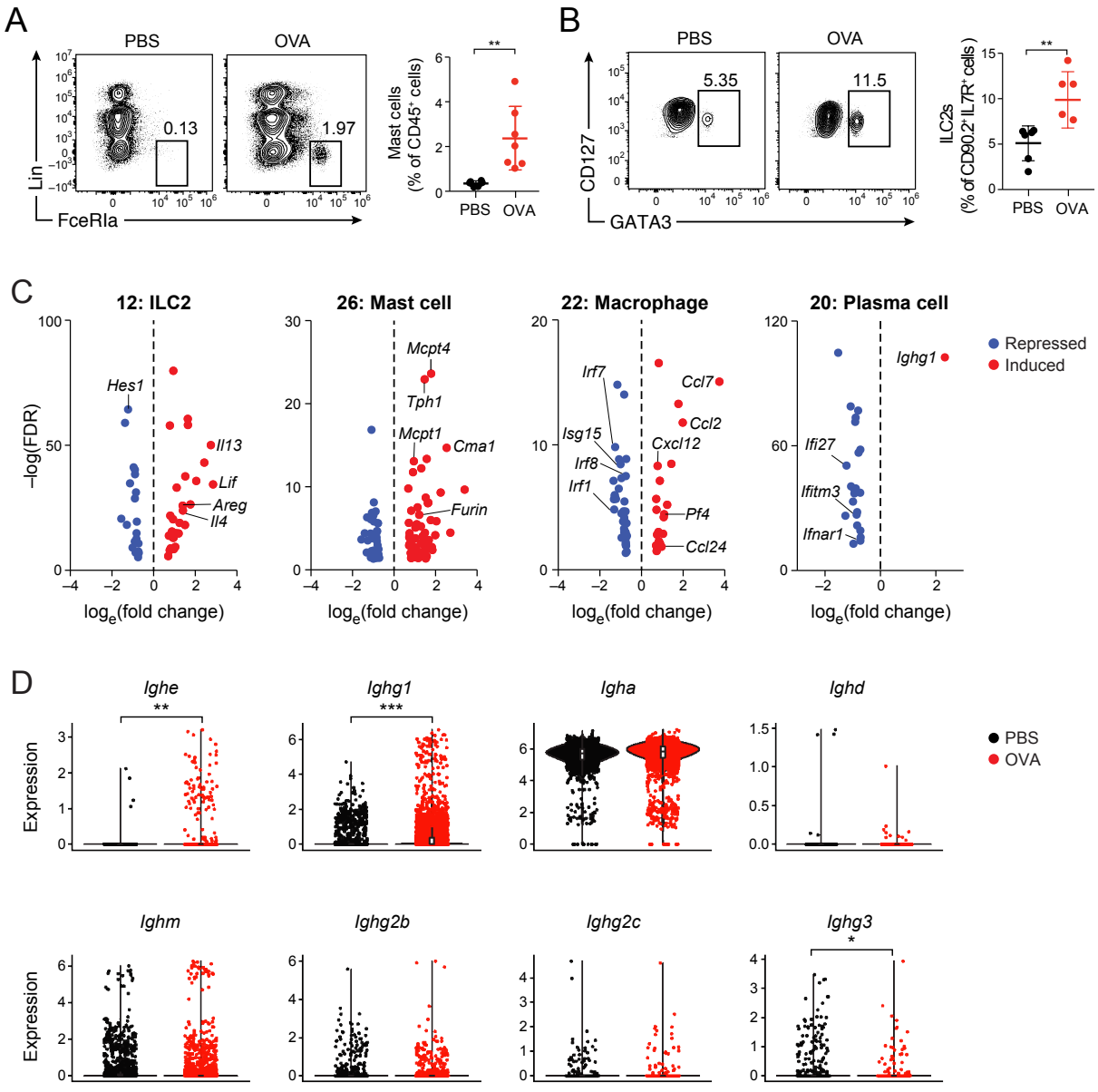

A
PBS
OVA
0.13
1.97
Lin
FceRIa
Mast cells (% of CD45+ cells)
**
PBS
OVA
B
PBS
OVA
5.35
11.5
CD127
GATA3
ILC2s (% of CD90.2+ IL7R+ cells)
**
PBS
OVA
C
12: ILC2
26: Mast cell
22: Macrophage
20: Plasma cell
–log(FDR)
Hes1
Il13
Lif
Areg
Il4
Mcpt4
Tph1
Mcpt1
Cma1
Furin
Irf7
Ccl7
Ccl2
Isg15
Cxcl12
Irf8
Irf1
Pf4
Ccl24
Ighg1
Ifi27
Ifitm3
Ifnar1
log_e(fold change)
Repressed
Induced
D
Ighe
Ighg1
Igha
Ighd
Ighm
Ighg2b
Ighg2c
Ighg3
Expression
**
***
*
PBS
OVA

Figure S2. Cell proportions in T, B, mast cells and ILC2s, and gene expression in mast cells, ILC2s, macrophages and plasma cells in OVA-induced type 2 inflammation, related to Figure 2

(**A,B**) Flow cytometry analysis of frequencies of mast cells (B) and ILC2s (C) in the LP of mice treated with PBS (black) or OVA (red). Left: representative FACS plots; Right: summary of results. Points: individual mice mean±SEM; **$p < 0.01$, *t* test.

(**C**) Differentially expressed genes in ILC2s, mast cells, macrophages and plasma cells in the LP. Shown are genes repressed (blue) or induced (red) ($|\text{fold change}| \geq 2$, $p < 0.05$, likelihood ratio test, frequency of expressing cells ≥ 25% at the up-regulation side) by OVA-induced inflammation in each labeled cell type. Dots: genes, with key ones labeled.

(**D**) Distribution of expression amounts (y axis, $\log_2(\text{TPM}+1)$) of *Igh* genes (labeled) in plasma cells in homeostatic (black) or OVA-induced inflammatory (red) conditions. *$p < 3\times10^{-5}$, **$p < 3\times10^{-13}$, ***$p < 2\times10^{-107}$, likelihood ratio test. Data are from two (A, B) or seven (C, D) independent experiments.

Figure S3

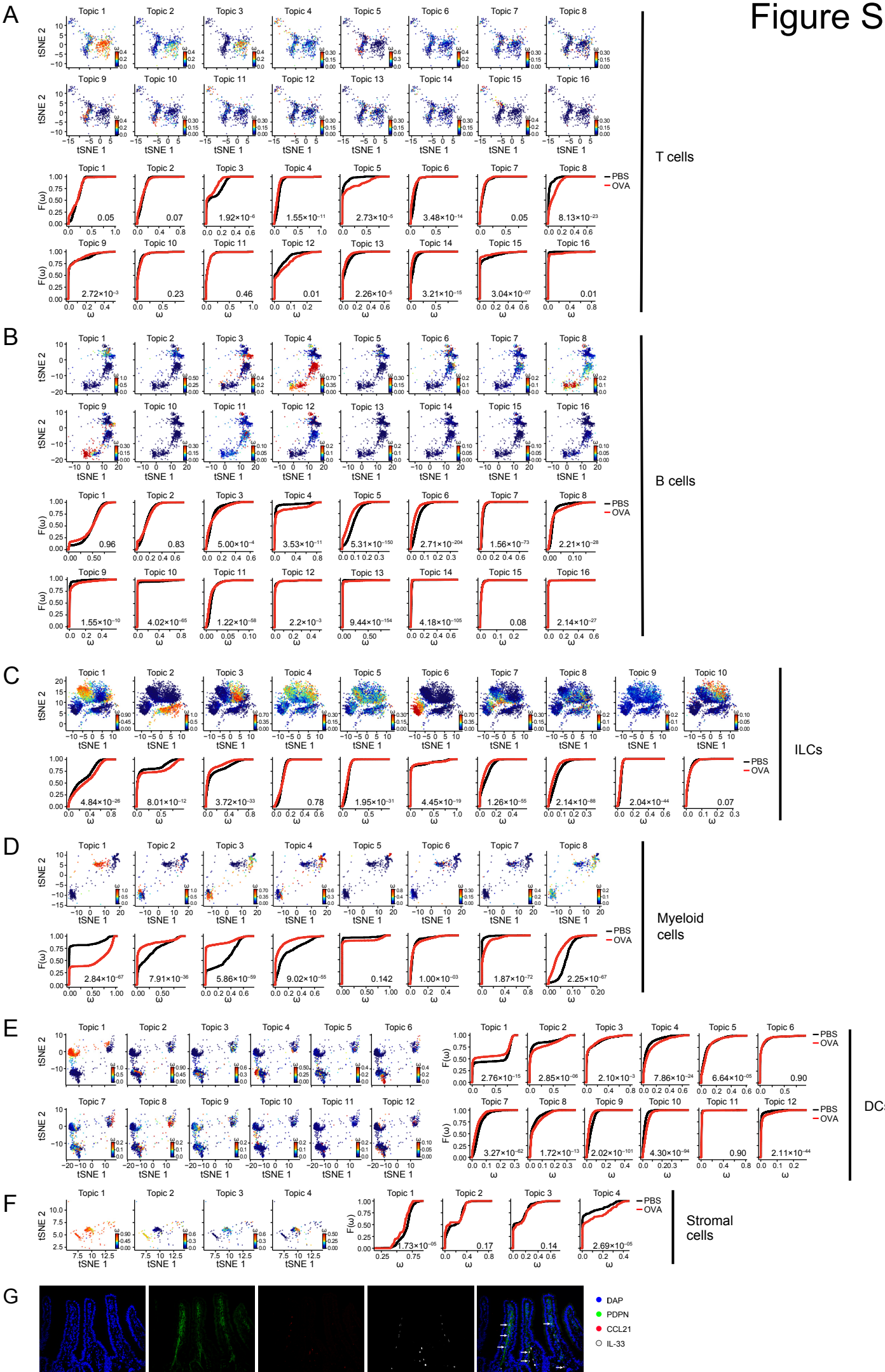
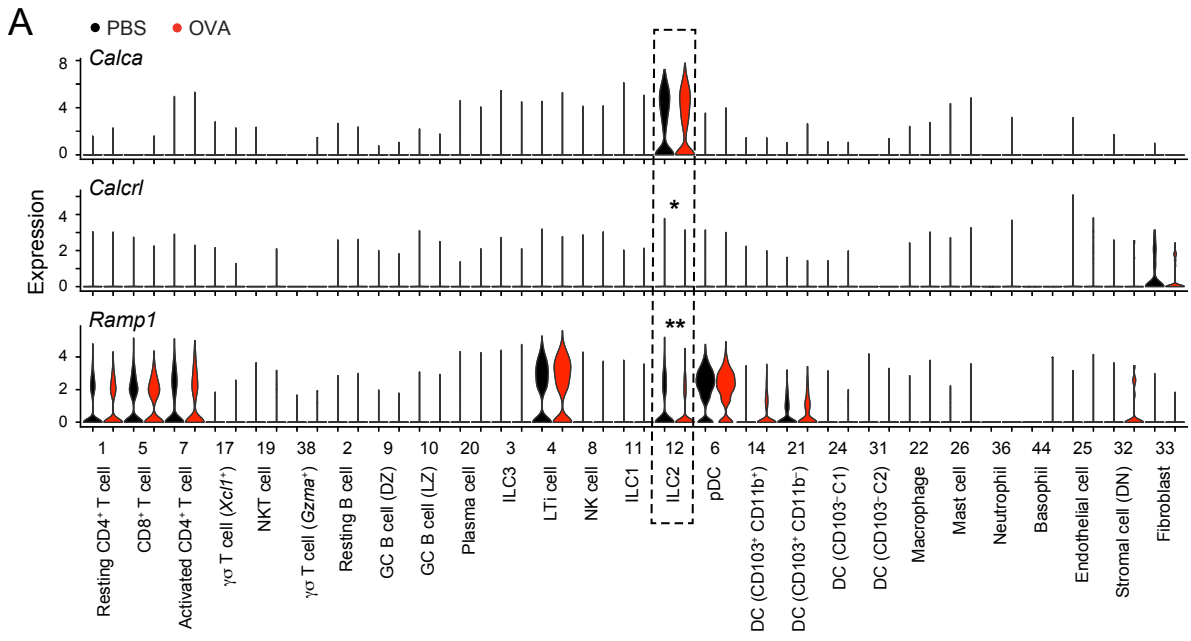

A
Topic 1
Topic 2
Topic 3
Topic 4
Topic 5
Topic 6
Topic 7
Topic 8
Topic 9
Topic 10
Topic 11
Topic 12
Topic 13
Topic 14
Topic 15
Topic 16
tSNE 1
tSNE 2
F(ω)
ω
PBS
OVA
0.05
0.07
1.92×10⁻⁶
1.55×10⁻¹¹
2.73×10⁻⁵
3.48×10⁻¹⁴
0.05
8.13×10⁻²³
2.72×10⁻³
0.23
0.46
0.01
2.26×10⁻⁵
3.21×10⁻¹⁵
3.04×10⁻⁰⁷
0.01
T cells
B
0.96
0.83
5.00×10⁻⁴
3.53×10⁻¹¹
5.31×10⁻¹⁵⁰
2.71×10⁻²⁰⁴
1.56×10⁻⁷³
2.21×10⁻²⁸
1.55×10⁻¹⁰
4.02×10⁻⁶⁵
1.22×10⁻⁵⁸
2.2×10⁻³
9.44×10⁻¹⁵⁴
4.18×10⁻¹⁰⁵
0.08
2.14×10⁻²⁷
B cells
C
Topic 10
4.84×10⁻²⁶
8.01×10⁻¹²
3.72×10⁻³³
0.78
1.95×10⁻³¹
4.45×10⁻¹⁹
1.26×10⁻⁵⁵
2.14×10⁻⁸⁸
2.04×10⁻⁴⁴
0.07
ILCs
D
2.84×10⁻⁶⁷
7.91×10⁻³⁶
5.86×10⁻⁵⁹
9.02×10⁻⁵⁵
0.142
1.00×10⁻⁰³
1.87×10⁻⁷²
2.25×10⁻⁶⁷
Myeloid cells
E
Topic 11
Topic 12
2.76×10⁻¹⁵
2.85×10⁻⁰⁶
2.10×10⁻³
7.86×10⁻²⁴
6.64×10⁻⁰⁵
0.90
3.27×10⁻⁶²
1.72×10⁻¹³
2.02×10⁻¹⁰¹
4.30×10⁻⁹⁴
0.90
2.11×10⁻⁴⁴
DCs
F
1.73×10⁻⁰⁵
0.17
0.14
2.69×10⁻⁰⁵
Stromal cells
G
DAP
PDPN
CCL21
IL-33
50 μm

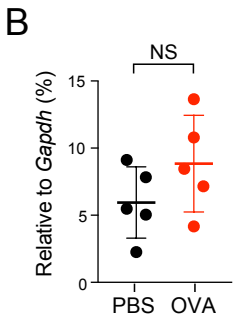
Figure S3. Topic modeling on T cells, B cells, DCs, ILCs, myeloid cells and stromal cells, and co-expression of CCL21 and IL-33 in PDPN$^+$ stromal cells in the small intestine, related to Figure 3

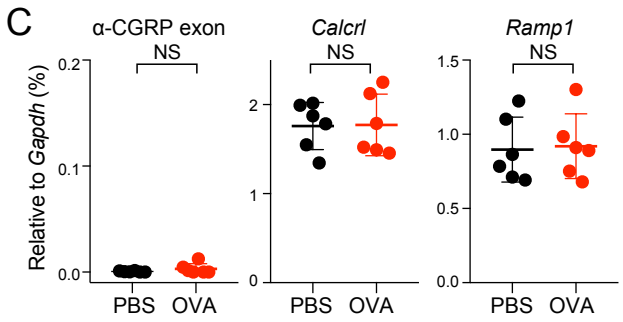
(**A-F**) Biological programs in each cell subset revealed by topic modeling. Shown are topics in T cells (A), B cells (B), ILCs (C), myeloid cells (D), DCs (E) and stromal cells (F). Top (A-D) and left (E and F): a portion of the 2D embedding in **Figure 1B**, only cells from the noted subset cells were shown, colored by the topic's weight in the cell. Bottom (A-D) and right (E and F): empirical cumulative density function (y axis) of topic weights (x axis) for cells from mice treated with PBS (black curve) or OVA (red curve). p values: Mann–Whitney U test.

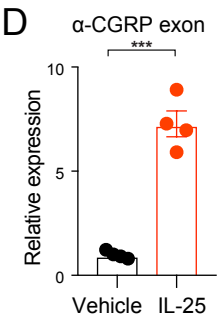
(**G**) co-localization of CCL21 and IL-33 in subsets of PDPN$^+$ stromal cells (arrow) in the small intestines of WT mice. Representative IF images of the small intestines of wild type mice. Scale bars, 50 μm. Data are from seven (A-F) independent experiments or are representative of three independent experiments.

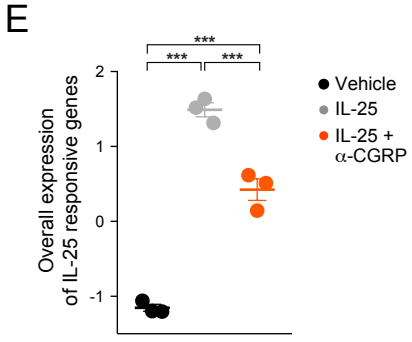
Figure S4


A
PBS
OVA
Calca
Calcrl
Ramp1
Expression
*
**
1 Resting CD4+ T cell
5 CD8+ T cell
7 Activated CD4+ T cell
17 γσ T cell (Xcl1+)
19 NKT cell
38 γσ T cell (Gzma+)
2 Resting B cell
9 GC B cell (DZ)
10 GC B cell (LZ)
20 Plasma cell
3 ILC3
4 LTi cell
8 NK cell
11 ILC1
12 ILC2
6 pDC
14 DC (CD103+ CD11b+)
21 DC (CD103+ CD11b-)
24 DC (CD103- C1)
31 DC (CD103- C2)
22 Macrophage
26 Mast cell
36 Neutrophil
44 Basophil
25 Endothelial cell
32 Stromal cell (DN)
33 Fibroblast


B
Relative to Gapdh (%)
NS
PBS
OVA


C
α-CGRP exon
Calcrl
Ramp1
Relative to Gapdh (%)
NS
PBS
OVA


D
α-CGRP exon
***
Relative expression
Vehicle
IL-25


E
***
Overall expression of IL-25 responsive genes
Vehicle
IL-25
IL-25 + α-CGRP

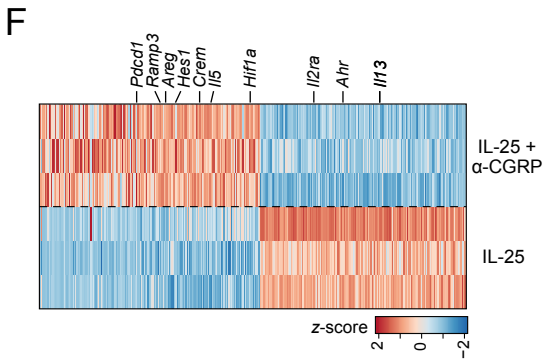

F
Pdcd1
Ramp3
Areg
Hes1
Crem
Il5
Hif1a
Il2ra
Ahr
Il13
IL-25 + α-CGRP
IL-25
z-score

Figure S4. Expression of *Calca*, *Calcrl*, *Ramp1* and *Il5* genes in intestinal KLRG1$^+$ ILC2s in homeostatic and inflammatory conditions, related to Figure 4

(**A**) Distribution of expression amounts (y axis, $\log_2$(TPM+1)) of *Calca* (top), *Calcrl* (middle), *Ramp1* (bottom) in each cell type (*x* axis) in mice treated with PBS (black) or OVA (red) as in **Figure S1A** on day 36. ILC2s are highlighted. *p < 0.05, **p < 2.3×10^{-06}, likelihood ratio test.

(**B**) Expression amounts (y axis, quantitative PCR normalized to *Gapdh*) of CT exon of *Calca* gene in LP ILC2s isolated from PBS or OVA-treated mice as in **Figure S1A** on day 36. Points: individual experiments (n=5); mean and SEM, NS: p > 0.05, *t* test.

(**C**) Expression amount (y axis, quantitative PCR normalized to *Gapdh*) of α-CGRP exon of *Calca*, *Calcrl,* and *Ramp1* in LP ILC2s isolated from control (black) or OVA-treated (red) mice as in **Figure S1A** on day 27. Points: individual experiments (n=6); mean and SEM, NS: p > 0.05, *t* test.

(**D**) The fold change of relative expression (y axis, quantitative PCR normalized to *Gapdh*) of α-CGRP exon in LP ILC2s stimulated with IL-25 or vehicle control for 24 hours *in vitro*. Points: individual experiments (n=4); mean and SEM, ***P < 0.001, *t* test.

(**E**) Overall Expression (OE) scores (**STAR Methods**) of the IL-25-induced genes in **Figure 4C**. Points: individual samples (n=3); mean and SEM, ***FDR < 0.001, *t* test.

(**F**) Expression (color bar, Z score) of genes (columns) significantly induced in LP ILC2s (Fold change ≥ 2, p < 0.05) by α-CGRP compared to control for 3 hours in the presence of IL-25. Key genes are highlighted. mean±SEM, ***p < 0.001, NS: p > 0.05, *t* test (B, C, D, E). Data are from seven (A), five (B), six (C), four (D) independent experiments, or are representative of two (E, F) independent experiments.

Figure S5

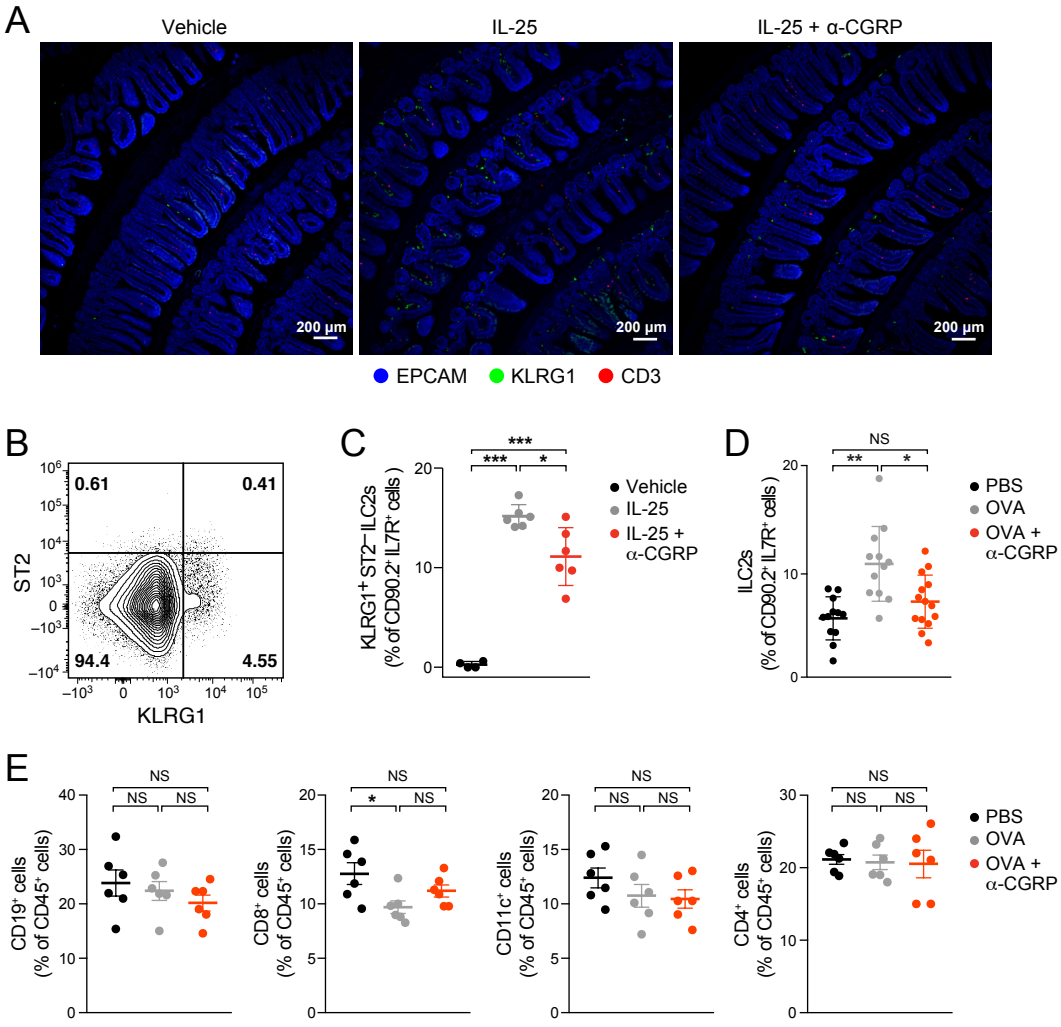

A
Vehicle
IL-25
IL-25 + α-CGRP
200 μm
EPCAM KLRG1 CD3
B
0.61
0.41
94.4
4.55
ST2
KLRG1
C
KLRG1+ ST2− ILC2s (% of CD90.2+ IL7R+ cells)
Vehicle
IL-25
IL-25 + α-CGRP
D
ILC2s (% of CD90.2+ IL7R+ cells)
PBS
OVA
OVA + α-CGRP
E
CD19+ cells (% of CD45+ cells)
CD8+ cells (% of CD45+ cells)
CD11c+ cells (% of CD45+ cells)
CD4+ cells (% of CD45+ cells)
NS

Figure S5. α-CGRP suppress expansion of intestinal KLRG1$^+$ ILC2s *in vivo* but does not affect other major immune cell types, related to Figure 5

(**A**) α-CGRP co-treatment antagonizes CD3$^-$KLRG1$^+$ ILC2 expansion *in vivo*. Representative IF images of CD3$^-$KLRG1$^+$ ILC2 in the small intestines of mice treated as in **Figure 5A**. Scale bars, 200 μm.

(**B**) Flow cytometry analysis of ST2 expression on LP ILCs (gated on CD45$^+$Lin$^-$ CD90.2$^+$IL7R$^+$) isolated from WT mice.

(**C**) Frequency (*y* axis) of KLRG1$^+$ ST2$^-$ cells in total ILCs in mLNs of mice treated as in **Figure 5A**. Points: individual mice (n=6).

(**D**) Frequency (*y* axis) of ILC2s in total ILCs in LP of the small intestines of mice treated as in **Figure 5F** on day 36. Point: individual mice (n=12).

(**E**) Frequency (*y* axis) of CD19$^+$, CD8$^+$, CD11c$^+$ or CD4$^+$ cells in total CD45$^+$ cells in LP of the small intestines of mice treated as in **Figure 5F** on day 36. Point: individual mice (n=6). mean±SEM, *p < 0.05, **p < 0.01, ***p < 0.001, NS: p > 0.05, *t* test (C, D, E). Data are representative of two (A, B) independent experiments, or are from three (C, D) or two (E) independent experiments.

Figure S6

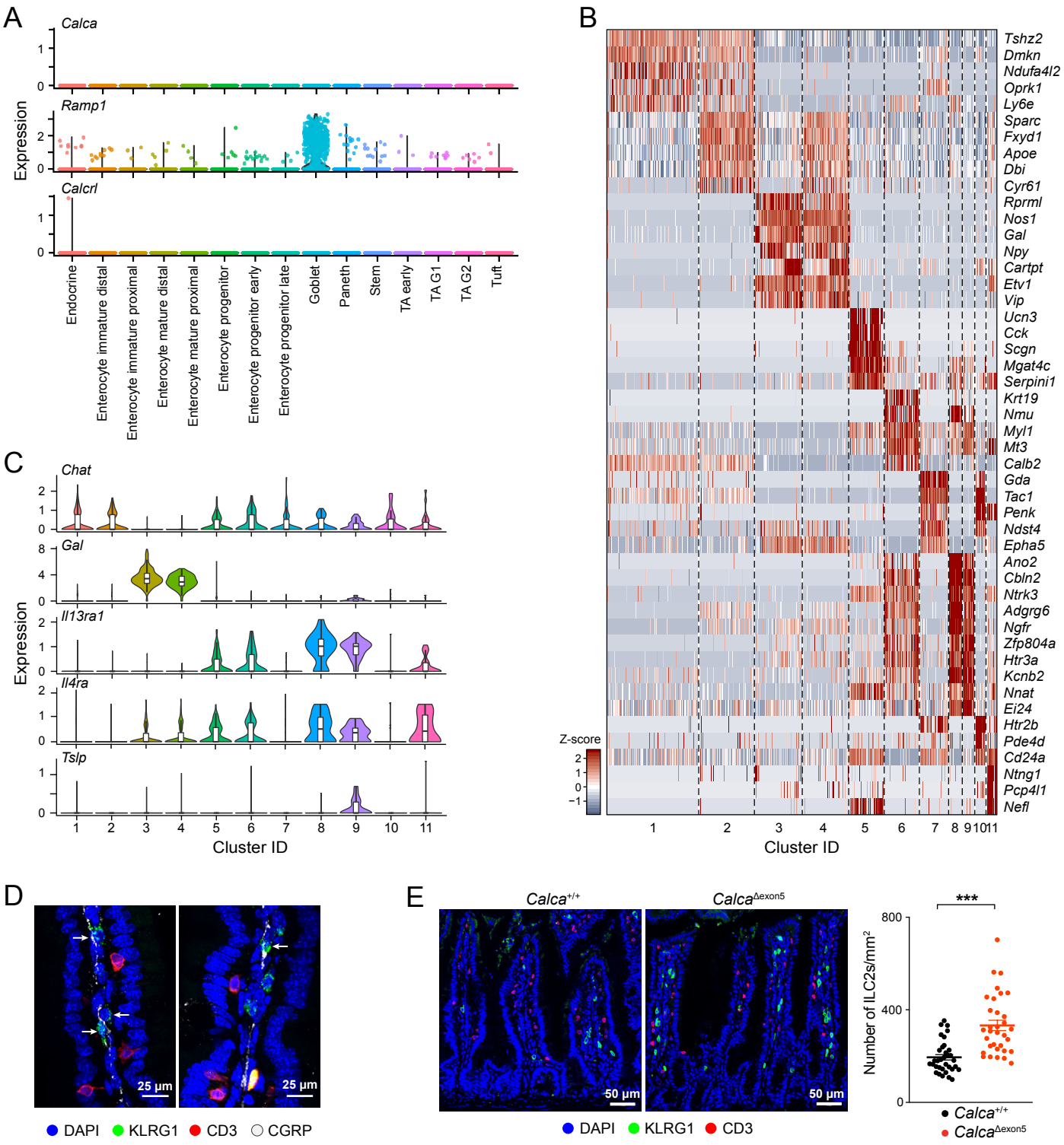

A
Calca
Ramp1
Calcrl
Expression
Endocrine
Enterocyte immature distal
Enterocyte immature proximal
Enterocyte mature distal
Enterocyte mature proximal
Enterocyte progenitor
Enterocyte progenitor early
Enterocyte progenitor late
Goblet
Paneth
Stem
TA early
TA G1
TA G2
Tuft
B
Tshz2
Dmkn
Ndufa4l2
Oprk1
Ly6e
Sparc
Fxyd1
Apoe
Dbi
Cyr61
Rprml
Nos1
Gal
Npy
Cartpt
Etv1
Vip
Ucn3
Cck
Scgn
Mgat4c
Serpini1
Krt19
Nmu
Myl1
Mt3
Calb2
Gda
Tac1
Penk
Ndst4
Epha5
Ano2
Cbln2
Ntrk3
Adgrg6
Ngfr
Zfp804a
Htr3a
Kcnb2
Nnat
Ei24
Htr2b
Pde4d
Cd24a
Ntng1
Pcp4l1
Nefl
Z-score
Cluster ID
C
Chat
Gal
Il13ra1
Il4ra
Tslp
Expression
Cluster ID
D
25 μm
DAPI KLRG1 CD3 CGRP
E
Calca+/+
CalcaΔexon5
50 μm
DAPI KLRG1 CD3
***
Number of ILC2s/mm2
Calca+/+
CalcaΔexon5

Figure S6. scRNA-seq analysis of intestinal epithelium and enteric neurons, ATAC-seq analysis of intestinal ILC2s and immunofluorescence staining analysis of the small intestine of *Calca*$^{\Delta exon5}$ mice, related to Figure 6

(**A**) Undetectable expression of *Calca* and *Calcrl* in epithelium of wild type mice (Haber et al, 2017). Distribution of expression amounts (y axis, log_2(TPM+1)) of *Calca* (top), *Ramp1* (middle), *Calcrl* (bottom) in each epithelial cell type as labeled.

(**B**) Marker genes of each enteric neuron clusters. Heatmap showing relative expression (Z score of log_2(TPM+1)) of top 5 marker genes (row) of each cluster (column) in **Figure 6A**.

(**C**) Distribution of expression amounts (y axis, log_2(TPM+1)) of *Chat*, *Gal*, *Il13ra1*, *Il4ra* and *Tslp* gene in each cluster (*x* axis) in **Figure 6A.**

(**D**) Interaction between ChAT-expressing neuron fibers and CD3$^-$KLRG1$^+$ ILC2s (arrow) in the small intestines of WT mice. Representative IF images of the small intestines of wild type mice. Scale bar, 25 μm.

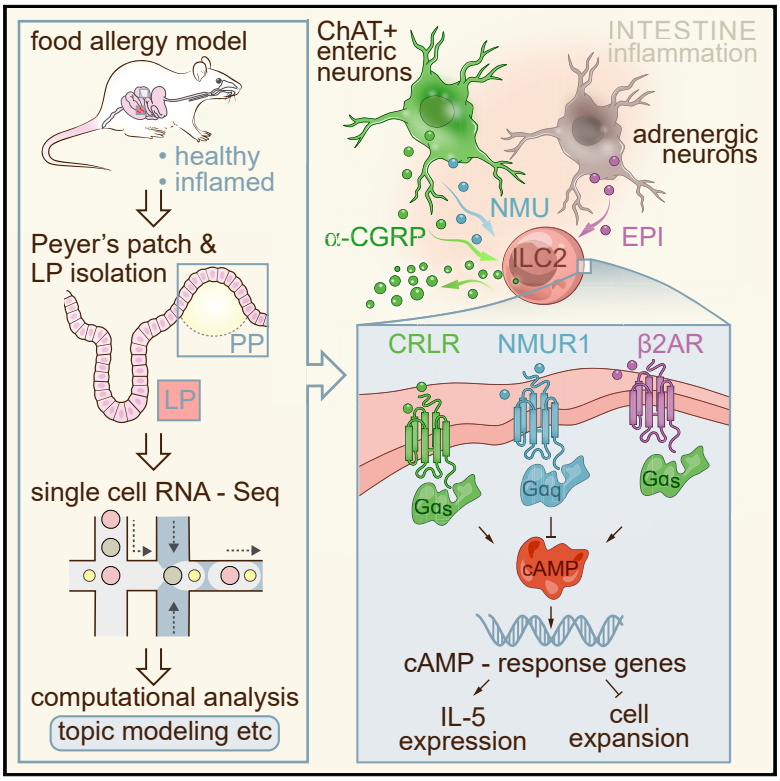
(**E**) α-CGRP deficiency affects ILC2 expansion in the inflammatory condition *in vivo*. Left: representative IF images of ILC2s (KLRG1$^+$CD3$^-$) in the small intestine of WT or *Calca*$^{\Delta exon5}$ mice challenged with intraperitoneal injection of IL-25 for 48 hours. Scale bars, 50 μm. Right: density of ILC2s (y axis, number per mm^2) in WT and *Calca*$^{\Delta exon5}$ mice. Points: individual section (n=33 from 4 mice). mean and SEM, ***p < 0.001, Student's *t* test. Data are two (D) independent experiments or representative of three mice (D).

Article

Immunity

Transcriptional Atlas of Intestinal Immune Cells Reveals that Neuropeptide α-CGRP Modulates Group 2 Innate Lymphoid Cell Responses

Graphical Abstract



Highlights

- scRNA-seq reveals intestinal immune cell programs in allergic inflammation
- Intestinal KLRG1$^+$ ILC2s express α-CGRP and its receptors
- α-CGRP regulates type 2 cytokine production of KLRG1$^+$ ILC2s
- α-CGRP maintains KLRG1$^+$ ILC2 homeostasis and the type 2 immune machinery

Authors

Heping Xu, Jiarui Ding, Caroline B.M. Porter, ..., Vijay K. Kuchroo, Aviv Regev, Ramnik J. Xavier

Correspondence

xuheping@westlake.edu.cn (H.X.), aregev@broadinstitute.org (A.R.), xavier@molbio.mgh.harvard.edu (R.J.X.)

In Brief

Allergic inflammation involves the interaction of multiple immune cell types, as well as their crosstalk with other physiological systems, such as neurons. By establishing intestinal immune cell atlas at different states, Xu et al. identify that neuropeptide α-CGRP modulates group 2 innate lymphoid cell responses and the allergic reaction.

Xu et al., 2019, Immunity *51*, 696–708
October 15, 2019 © 2019 Elsevier Inc.
https://doi.org/10.1016/j.immuni.2019.09.004

CellPress

CellPress

Immunity
Article

Transcriptional Atlas of Intestinal Immune Cells Reveals that Neuropeptide α-CGRP Modulates Group 2 Innate Lymphoid Cell Responses

Heping Xu,[1,2,3,11,12,*] Jiarui Ding,[1,11] Caroline B.M. Porter,[1] Antonia Wallrapp,[4] Marcin Tabaka,[1] Sai Ma,[1] Shujie Fu,[2,3] Xuanxuan Guo,[2,3] Samantha J. Riesenfeld,[1] Chienwen Su,[5] Danielle Dionne,[1] Lan T. Nguyen,[1] Ariel Lefkovith,[1] Orr Ashenberg,[1] Patrick R. Burkett,[4] Hai Ning Shi,[5] Orit Rozenblatt-Rosen,[1] Daniel B. Graham,[1,6,7,8] Vijay K. Kuchroo,[1,4] Aviv Regev,[1,9,12,*] and Ramnik J. Xavier[1,6,7,8,10,13,*]

[1]Broad Institute of MIT and Harvard, Cambridge, MA 02142, USA
[2]Key Laboratory of Structural Biology of Zhejiang Province, School of Life Sciences, Westlake University, Hangzhou 310024, Zhejiang Province, China
[3]Laboratory of Systems Immunology, Institute of Basic Medical Sciences, Westlake Institute for Advanced Study, Hangzhou 310024, Zhejiang Province, China
[4]Evergrande Center for Immunologic Diseases, Harvard Medical School and Brigham and Women's Hospital, Boston, MA 02114, USA
[5]Mucosal Immunology and Biology Research Center, Massachusetts General Hospital and Harvard Medical School, Charlestown, MA 02129, USA
[6]Department of Molecular Biology, Massachusetts General Hospital, Harvard Medical School, Boston, MA 02114, USA
[7]Gastrointestinal Unit and Center for the Study of Inflammatory Bowel Disease, Massachusetts General Hospital, Harvard Medical School, Boston, MA 02114, USA
[8]Center for Microbiome Informatics and Therapeutics, Massachusetts Institute of Technology, Cambridge, MA 02114, USA
[9]Howard Hughes Medical Institute and Koch Institute for Integrative Cancer Research, Department of Biology, Massachusetts Institute of Technology, Cambridge, MA 02142, USA
[10]Center for Computational and Integrative Biology, Massachusetts General Hospital, Harvard Medical School, Boston, MA 02114, USA
[11]These authors contributed equally
[12]Senior author
[13]Lead Contact
*Correspondence: xuheping@westlake.edu.cn (H.X.), aregev@broadinstitute.org (A.R.), xavier@molbio.mgh.harvard.edu (R.J.X.)
https://doi.org/10.1016/j.immuni.2019.09.004

SUMMARY

Signaling abnormalities in immune responses in the small intestine can trigger chronic type 2 inflammation involving interaction of multiple immune cell types. To systematically characterize this response, we analyzed 58,067 immune cells from the mouse small intestine by single-cell RNA sequencing (scRNA-seq) at steady state and after induction of a type 2 inflammatory reaction to ovalbumin (OVA). Computational analysis revealed broad shifts in both cell-type composition and cell programs in response to the inflammation, especially in group 2 innate lymphoid cells (ILC2s). Inflammation induced the expression of exon 5 of *Calca*, which encodes the alpha-calcitonin gene-related peptide (α-CGRP), in intestinal KLRG1$^+$ ILC2s. α-CGRP antagonized KLRG1$^+$ ILC2s proliferation but promoted IL-5 expression. Genetic perturbation of α-CGRP increased the proportion of intestinal KLRG1$^+$ ILC2s. Our work highlights a model where α-CGRP-mediated neuronal signaling is critical for suppressing ILC2 expansion and maintaining homeostasis of the type 2 immune machinery.

INTRODUCTION

The immune system in the small intestine is composed of a complex network of innate and adaptive components that sense and respond to antigens from the diet, commensal microbiota, and pathogens. Dysregulated immune reactions often lead to chronic inflammatory responses, including type 2 inflammation (Gieseck et al., 2018; Hammad and Lambrecht, 2015; Pulendran and Artis, 2012), which in turn plays a key underlying role in several unrelenting inflammatory diseases, including food allergy (Locksley, 2010; Tordesillas et al., 2017).

Several hallmarks of type 2 inflammation, including the production of immunoglobulin E (IgE) antibodies and type 2 cytokines, such as interleukin-13 (IL-13) and IL-5, rely on tightly regulated and coordinated immune responses across different cell types, such as T helper 2 (Th2) cells, mast cells, and group 2 innate lymphoid cells (ILC2s). In particular, ILC2s have emerged as key regulators of tissue homeostasis and type 2 inflammation (Artis and Spits, 2015; Kotas and Locksley, 2018) and form the prominent source of type 2 cytokines at the early stages of inflammatory responses (Molofsky et al., 2015; Neill et al., 2010; Price et al., 2010).

While the core transcriptional program of ILC2s maintains their cellular identity and homeostatic type 2 cytokine competence (Ricardo-Gonzalez et al., 2018), their activity in the intestines is shaped by tissue-specific signals, including activation by IL-25 produced by tuft cells (von Moltke et al., 2016) and suppression

by micronutrients (Spencer et al., 2014). Recent studies show that neuronal signals orchestrate intestinal ILC2 activity. For example, the neuropeptide neuromedin U (NMU), secreted from cholinergic neurons, amplifies ILC2 activation and proliferation, thereby promoting type 2 inflammation (Cardoso et al., 2017; Klose et al., 2017; Wallrapp et al., 2017). In contrast, β-adrenergic-receptor-mediated signaling suppresses ILC2 activity in intestinal infection models (Moriyama et al., 2018).

Despite these substantial advances, we still have an incomplete understanding of the cellular participants in type 2 inflammation, the mechanisms that maintain homeostasis, and which additional cell types besides immune cells may participate in this cellular circuit in the small intestine. Single-cell RNA sequencing (scRNA-seq) can dissect cellular diversity on a large scale (Tanay and Regev, 2017; Wagner et al., 2016) and identify cell states of individual cell types in response to different stimuli (Bielecki et al., 2018; Haber et al., 2017).

Here, we combine scRNA-seq with physiological and genetic perturbations to dissect the cellular circuit of type 2 intestinal inflammation. To uncover key responding cellular components, we profiled individual immune cells from the lamina propria (LP) and Peyer's patches (PPs) in homeostasis and in an intestinal type 2 inflammatory model. Computational analysis showed that both cell compositions and cell programs shifted in response to inflammation, and highlighted the prominent induction of alpha-calcitonin gene-related peptide (α-CGRP) transcription in ILC2s. In inflammatory conditions, α-CGRP suppressed activation of ILC2s, but induced IL-5 expression. α-CGRP stimulation *in vitro* increased the intracellular concentration of cyclic AMP (cAMP), induced the expression of a cAMP-response gene module and suppressed cell proliferation. At homeostasis *in vivo*, choline acetyltransferase ($ChAT^+$) enteric neurons were the predominant source of α-CGRP and constitutively interacted with ILC2s. Genetic perturbation of α-CGRP increased the proportion of intestinal $KLRG1^+$ ILC2s and the number of tuft cells. Our study reveals a neuro-immune cellular circuit that modulates type 2 inflammation, highlighting critical functions of α-CGRP-mediated neuronal signaling in maintaining homeostasis of ILC2s and the type 2 immune machinery.

RESULTS

A Mouse Immune Cell Atlas of the Small Intestine Provides a Reference Map of Homeostatic and Type 2 Inflammatory Conditions

To comprehensively characterize immune cells in the small intestine, we generated scRNA-seq profiles for 58,067 immune cells collected from LP and PP regions at steady state and after induction of a type 2 inflammatory reaction to ovalbumin (OVA) (Brandt et al., 2003; Figures 1A and S1A). To ensure sufficient representation of rare cell types, we combined two experimental normalization strategies (using flow sorting to remove either a portion of IgD^+ naive B cells—the most abundant cell type in PPs—or all $CD19^+$ B and $CD3^+$ T cells) (Figure S1B; STAR Methods) with profiling of a sufficiently large number of cells (probability >0.99 in recovering at least 15 cells from each of an expected 30 clusters, the rarest estimated at 0.1%; STAR Methods) by massively parallel scRNA-seq (Haber et al., 2017; STAR Methods). After combining cells from both normalization processes, we obtained 36,797 and 21,270 high-quality cells passing initial filtering (STAR Methods) from PP and LP regions, respectively.

Overall, we annotated 27 cell subsets across the two compartments, spanning T cells, B cells, ILCs, dendritic cells (DCs), myeloid cells, and stromal cells, in frequencies ranging from 0.07% to 14%. We corrected experimental batch effects via a robust reference-projection approach (STAR Methods) and visualized the data with scvis (Ding et al., 2018), a deep generative model-based method for modeling and visualizing scRNA-seq data (Figures 1B and S1C; STAR Methods). Our batch correction approach had equal or better concordance and mixing compared to three recently published methods (LIGER, Welch et al., 2019; Harmony, Korsunsky et al., 2018; and scVI, Lopez et al., 2018; Figures S1D and S1E; STAR Methods). Next, we elucidated identities of similar cell types based on genes that were differentially expressed between the cells in each cluster and the remaining cells (Table S1; STAR Methods), as well as between pairs of clusters (Table S2). We excluded from downstream analysis clusters mostly consisting of contaminants from epithelium, likely doublets, cells with a small number of unique molecular identifiers (UMIs) (Figure S1F), and cells lacking distinct markers (Figure S1G; STAR Methods). Altogether, we retained 27 clusters spanning 85% of the cells and each associated with distinct marker genes (Figures S1G and S1H; STAR Methods).

Importantly, known distinct cell types with highly similar expression profiles were correctly distinguished by our analysis. For example, $NKp46^+$ ILC3s and $CCR6^+$ lymphoid tissue inducer (LTi) cells were recovered as separate clusters, even though they both require RORγt-controlled expression programs for their fate determination (Robinette et al., 2015). Nevertheless, LTi cells were distinguished by significantly higher expression of major histocompatibility complex (MHC) class II antigen presentation modules (Figure S1I; $p < 0.05$, likelihood ratio test), whose expression on ILCs has been shown to regulate intestinal homeostasis (Hepworth et al., 2013).

The atlas highlighted expected differences in cellular composition between the LP and PP regions in the homeostatic state (Figures 1C, S1J, and S1K). We used a negative binomial regression model to account for cell counts from individual mice at the steady state (PBS, 6 PP and 4 LP) to address mouse-to-mouse differences in overall cell numbers that can impact the reliability of cell proportion estimates (Haber et al., 2017; STAR Methods). For example, resting and IgD^-GL7^+ germinal center (GC) B cells were exclusively found in PPs (Figure S1K). Conversely, although $CD138^+$ antibody-producing plasma cells differentiate from GC B cells, they were predominantly found in LP samples (Figure S1K) and confirmed in LP regions *in situ* (Figure S1L), highlighting their potential requirement for antibody secretion adjacent to microbes and other antigens in the intestinal mucosa. In another example, LTi cells were significantly enriched ($p = 4.5 \times 10^{-4}$, Wald test) in PP versus LP regions (Figure 1C), which we confirmed by flow cytometry (Figure 1D). The LTi cell distribution is consistent with their critical function in supporting lymphoid tissue development. ILC1s and natural killer (NK) cells were also significantly enriched in PP regions (Figure 1C; $p = 2.5 \times 10^{-9}$ and $p = 7.9 \times 10^{-24}$, respectively, Wald test), suggesting they have unique functions in PPs. Indeed, NK cells suppress affinity maturation of GC B cells (Rydyznski et al., 2018), which probably requires their localization in B cell follicles.

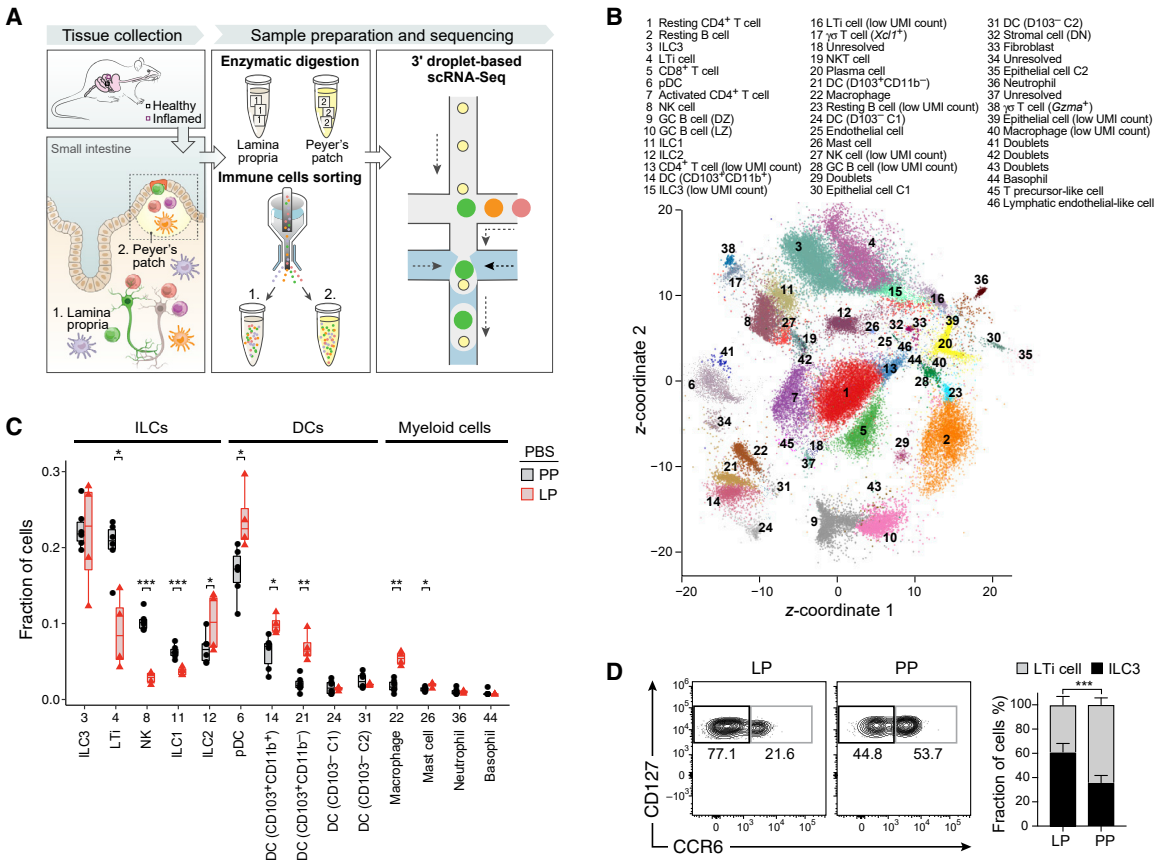


Figure 1. A Single-Cell Expression Atlas of Intestinal Immune Cells

(A) Experimental overview.

(B) Cell subsets in the intestinal immune cell atlas. scvis-learned two-dimensional (2D) representation of cell profiles (dots) from both PP and LP regions, colored and numbered by cluster membership. Clusters are rank ordered by size. DZ, dark zone; LZ, light zone; DN, double negative; C1, cluster 1; C2, cluster 2.

(C) Tissue distribution of non-T and non-B immune cells in homeostasis. Proportion (y axis) of each cell type in LP (red) and PP (black) regions of mice treated with PBS only. Points represent independent mice; boxplots show medians and interquartile ranges (IQRs). Whiskers show the lowest datum within 1.5 IQR of the lower quartile and the highest datum within 1.5 IQR of the upper quartile. *$p < 5 \times 10^{-2}$, **$p < 3 \times 10^{-8}$, and ***$p < 3 \times 10^{-9}$, Wald test.

(D) LTi cells are enriched in PP regions. Shown is flow cytometry analysis gated on $CD45^+Lin^-CD90.2^+IL7R^+ROR\gamma t^+$ cells. Data represent mean ± SEM; ***$p < 0.001$, Fisher's exact test.

Data are from seven (B), three (C), or two (D) independent experiments.

See also Figure S1 and Tables S1 and S2.

We further performed similar analyses to assess cell composition changes between the PP and LP regions using all data (Figure S1J), with the negative binomial regression model with both treatment (OVA or PBS) and location (PP or LP) as covariates. Generally, the results (Figure S1M) were consistent with the results in Figure 1C, with some minor exceptions; cluster 6 (plasmacytoid DCs [pDCs]) was not significantly different between regions, but cluster 24 ($CD103^-$ DCs) was significant. Thus, our comprehensive scRNA-seq dataset provides a reference map of immune cells in the small intestine, capturing rare immune cell types and their diversity across anatomical regions.

Increase in ILC2 Proportions and Changes in Their Expression Programs Are Prominent Features of OVA-Induced Type 2 Inflammation

Cell composition was remodeled in type 2 inflammation (Figures S1J, 2A, and 2B), when comparing inflammatory (OVA) and homeostatic (PBS) states, controlled for anatomical location by a negative binomial regression model when considering cells from all locations together, or when analyzing LP and PP data separately (Figure 2B; STAR Methods), highlighting both known and unique responses. In the combined analysis, mast cell expansion, a well-established feature of allergic reactions (Brandt et al., 2003), was observed in OVA-treated mice ($p = 4.9 \times 10^{-18}$, Wald test; Figure 2B) and validated by flow cytometry (Figure S2A). There was also an increase in ILC2 frequency in mice with type 2 immune reactions to OVA (Figure 2B; $p = 1.5 \times 10^{-2}$, Wald test), which we validated by flow cytometry (Figure S2B), highlighting their importance in this allergic inflammatory model (Burton et al., 2018). Macrophage and neutrophil frequencies also increased significantly in OVA-treated mice ($p = 2.6 \times 10^{-5}$ and $p = 9.5 \times 10^{-4}$, respectively, Wald test), reflecting immune cell infiltration. $CD11b^+CD103^+$ DCs, one of four different populations of DCs in the intestine (Mowat and Agace,

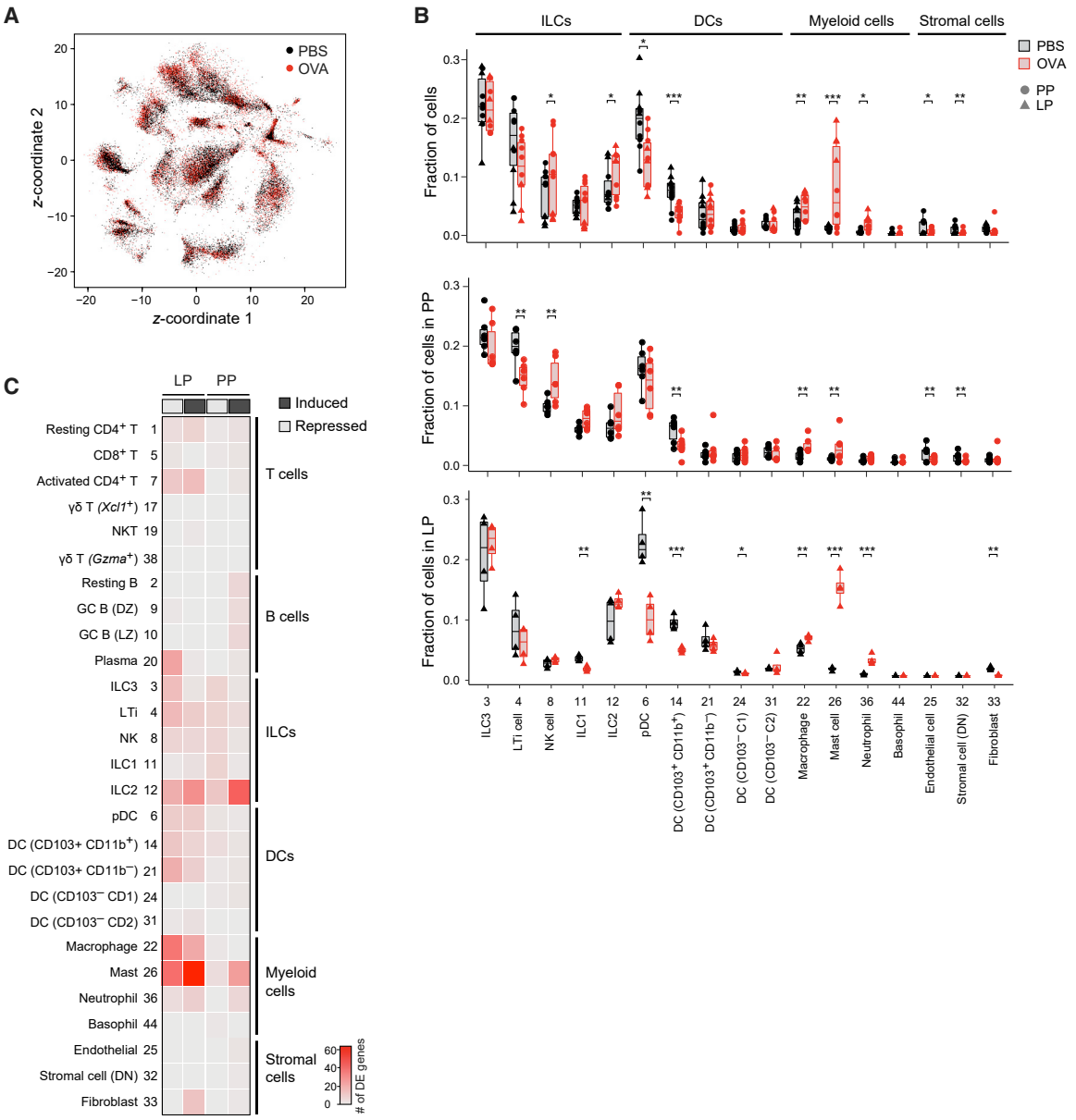


Figure 2. Increased ILC2 Proportions and Changes in ILC2 Programs Are Key Features in OVA-Induced Type 2 Inflammation

(A and B) Increased ILC2 and mast cell frequencies are prominent features in type 2 inflammation.

(A) A 2D embedding as in Figure 1B and colored by states (PBS or OVA).

(B) Distribution of cell type proportions (y axis) for each non-T and non-B cell subset (x axis) in the combined PP+LP dataset (top), PP (middle), or LP (bottom) in homeostatic (black) or OVA-induced inflammatory (red) conditions. Points represent independent mice; boxplots show IQR as in Figure 1C. *$p < 5 \times 10^{-2}$, **$p < 3 \times 10^{-5}$, and ***$p < 7 \times 10^{-11}$, Wald test (STAR Methods).

(C) ILC2s and mast cells show the most prominent changes in expression programs in type 2 inflammation. Number of genes significantly induced (black) or inhibited (gray) by OVA-induced type 2 inflammation in each cell subset (row) from the LP or PP regions.

Data are from seven independent experiments.

See also Figure S2 and Table S3.

2014), were the most significantly reduced by OVA-induced inflammation ($p = 6.4 \times 10^{-11}$, Wald test), suggesting that they are likely involved in the maintenance of gut homeostasis and suppressed during type 2 inflammation. The cellular compositions of T and B cell clusters were not significantly altered by the inflammation (data not shown).

Although most cell types changes (or lack thereof) were consistent between compartments and detected regardless of whether they were analyzed separately or jointly, there were some notable exceptions (Figure 2B). First, the proportion of ILC2s (cluster 12 cells) was significantly different between conditions only in the combined data ($p = 1.5 \times 10^{-2}$, Wald test) and

borderline otherwise, suggesting gained statistical power from analyzing the combined data. Conversely, the proportion of each of ILC1s (cluster 11) and fibroblasts (cluster 33) was changed in the two regions in opposite ways (enriched in one and depleted in the other), such that no significant change was detected when the two regions were considered together. The proportion of cells from several clusters was different in one region, but not the other (pDCs [cluster 6], neutrophils [cluster 36], endothelial cells [cluster 25], stromal cells [double negative (DN)] [cluster 32]), although this change was substantial enough to have been detected in the combined data. Thus, the negative binomial regression framework is a principled way of combining data from multiple regions (here, PP and LP) to quantify the significance of allergy on cell composition changes, simultaneously accounting for the influence of regions, and using raw count data instead of ratios.

The impact of type 2 inflammation on cell-intrinsic expression changes was most prominent in mast cells and ILC2s in both LP and PP regions (Figure 2C; Table S3). Genes associated with cell-type-specific activation were induced in mast cells (e.g., *Mcpt1* and *Mcpt4*) and ILC2s (e.g., *Il13* and *Il4*) (Figure S2C), suggesting an activation phenotype in both cell types. In addition, *Ighg1* and *Ighe* expression in plasma cells was significantly increased ($p = 1.45 \times 10^{-107}$ and 2.86×10^{-13}, respectively; likelihood ratio test) after the induction of allergic inflammation (Figure S2D), consistent with the fact that IL-4 induces class-switch recombination of the immunoglobulin heavy (Ig) chain toward IgG1 and IgE (Manis et al., 2002). Additionally, genes involved in the type 1 interferon pathway, such as *Irf1* and *Isg15* in macrophages and *Ifnar1* and *Ifitm3* in plasma cells, were suppressed during type 2 inflammation (Figure S2C), providing potential mechanistic explanations for the dampened antiviral immunity in allergic inflammation (Kloepfer et al., 2012; Rowe and Gill, 2015).

Topic Models Identify Cell-Type-Specific Programs that Are Increased with Inflammation in Mast Cells, ILC2s, Th2 Cells, and Fibroblast Subsets

To identify more nuanced changes in expression programs in response to type 2 inflammation, we relied on topic modeling using latent Dirichlet allocations (Blei et al., 2003), which has recently been applied to scRNA-seq data (Bielecki et al., 2018; duVerle et al., 2016). Originally developed to discover semantic topics reflected by words in documents (Dumais et al., 1990), topic modeling can be used to explore gene programs (“topics”) in each cell (“document”) based on the distribution of genes (“words”) expressed in the cell (STAR Methods). One gene can belong to multiple topics (programs) and its relative relevance in the topic is reflected by a weight. A cell is represented as a weighted mixture of topics, where the weights reflect the importance of the topic in the cell. We learned topic models for each cell lineage or group separately (Figures 3A-3E and S3A–S3F; Table S4), recovering both cell-type-specific programs (e.g., topic 1 of myeloid cells; Figure 3A) and ones that do not merely conform to cluster boundaries (e.g., topic 4 of B cells; Figure S3B). We focused on topics whose cell scores were differentially weighted between homeostasis and inflammation in a given cell lineage or group.

Topics characterizing activation programs had higher weights in mast cells and ILC2s from the inflammatory condition. In myeloid cells, topic 1 (“mast cell activation program”) was heavily weighted in the mast cell cluster, characterized by *Cpa3* and *Mcpt4* expression, and was significantly more prominent in mast cells from mice treated with OVA than controls ($p = 2.84 \times 10^{-67}$, Mann-Whitney *U* test; Figure 3A). In ILCs, topic 2 (“ILC2 activation program”) was heavily weighted in the ILC2 cluster, composed of type 2 genes such as *Il13* and *Il4*, and was significantly more prominent after induction of inflammation ($p = 8.01 \times 10^{-12}$, Mann-Whitney *U* test; Figure 3B).

Gene programs related to inflammatory responses were more heavily weighted in Th2 cells under inflammatory conditions, whereas those related to T regulatory cells were unchanged between inflammation and homeostasis. Specifically, in the topic model for T cells, topic 5 (“Th2 inflammatory program”) was heavily weighted in only the subset of cells from the activated $CD4^+$ T cell cluster that are likely Th2 cells (Figure 3C). This topic consisted of type 2 inflammatory genes (e.g., *Il13*, *Gata3*, *Il6*, *Areg*, and *Il1rl1*) and the cell weights were significantly higher in cells from OVA-treated mice than from controls ($p = 2.73 \times 10^{-5}$, Mann-Whitney *U* test; Figure 3C). Topic 9 (“T regulatory program”) included *Foxp3*, *Lag3*, *Il10*, and other Th cell regulatory genes and was present in a different subset of $CD4^+$ T cells (Figure 3D). The cell weights for this topic, however, showed only a minor change with inflammation ($p = 0.002$, Mann-Whitney *U* test; Figure 3D). Thus, activation of type 2 inflammation in the OVA allergy model may not have significantly interfered with the activity of regulatory T cells.

In stromal cells, topic 4, defined by the expression of the type 2 inflammatory cytokine *Il33* and key chemokines such as *Ccl21a*, was uniquely associated with the fibroblast cluster, and the cell weights were higher in the inflammatory condition (Figure 3E; $p = 2.69 \times 10^{-5}$, Mann-Whitney *U* test). We confirmed that IL-33 and CCL21 were co-expressed in $PDPN^+$ stromal cells by immunofluorescence (Figure S3G). Moreover, the number of $IL\text{-}33^+PDPN^+$ intestinal fibroblasts was significantly increased in mice under type 2 inflammation induced by OVA (Figure 3F), indicating that stromal-cell-derived IL-33 may play critical roles in promoting intestinal type 2 inflammation.

Calca-Encoded α-CGRP Expression Is a Key Feature of the ILC2 Activation Program Induced by Inflammation, but Its Receptor Is Repressed by Inflammation

Calca was the highest and most uniquely scoring gene in the ILC2 activation program (Figure 3B), and *Calca* transcript amounts were higher in ILC2s than in other cell types in our dataset (Figure 4A and S4A). Exons 4 and 5 of *Calca* encode the neuropeptides calcitonin (CT) and α-CGRP, respectively, via alternative splicing (Amara et al., 1982). qPCR revealed that while CT-encoding exon 4 was expressed in intestinal $KLRG1^+$ ILC2s at steady state (Figure S4B), α-CGRP-encoding exon 5 was detectable only following intragastric administration of OVA (Figures 4B and S4C). Conversely, the corresponding transcripts of α-CGRP receptor components (a G-protein-coupled receptor complex consisting of CRLR and RAMP1) was expressed in ILC2s at steady state (Figure 4B and S4A) but significantly repressed by intestinal type 2 inflammation (Figure 4B and S4C). The *Calcr* transcript, encoding the CT receptor, was not detectable by either scRNA-seq or qPCR (data not shown). Taken together, these results are consistent with a negative

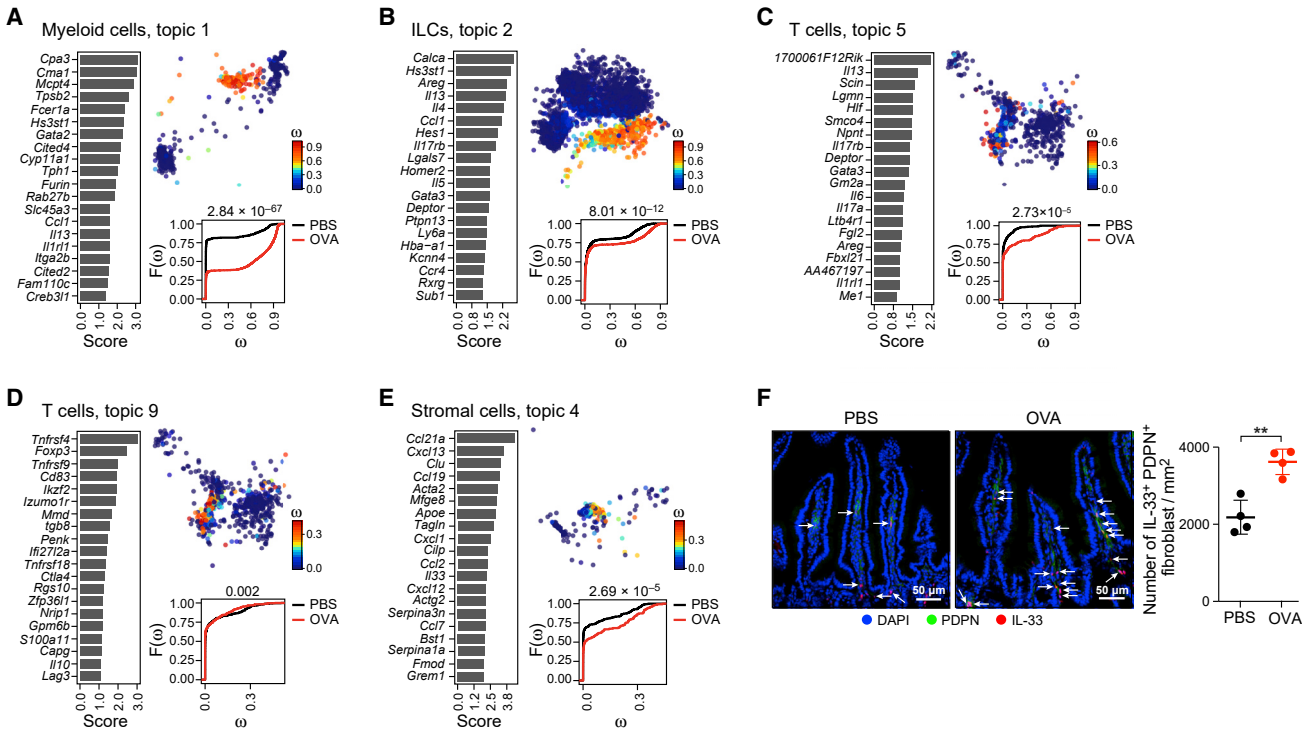


Figure 3. Topic Modeling of Cell-Type-Specific Programs in Response to Intestinal Type 2 Inflammation Predicts *Calca* as a Top Gene in ILC2s

(A–E) Inflammation associated programs in specific cell subsets. Shown are some of the topics that have differential scores between steady-state (PBS) and inflammatory conditions (OVA) for myeloid cells (A), ILCs (B) and T cells (C and D) in LP, or stromal cells (E) in PP. Left: bar plot showing the scores (x axis) of top ranked genes for this topic (y axis). Top right: a portion of the 2D embedding in Figure 1B, showing only cells from the noted subset cells, colored by the topic's weight in the cell (top right). Bottom right: empirical cumulative density function (y axis) of topic weights (x axis) for cells from mice treated with PBS (black curve) or OVA (red curve). p values were determined using a Mann-Whitney *U* test.

(F) Increased number of IL-33$^+$PDPN$^+$ fibroblasts in inflammation. Left: representative immunofluorescence (IF) images of the small intestines. Arrow shows IL-33$^+$PDPN$^+$ fibroblasts; scale bars, 50 μm. Points show individual mice. Data represent mean and SEM; **$p < 0.01$, Student's t test.

Data are from seven (A–E) or two (F) independent experiments. See also Figure S3 and Table S4.

feedback model where signaling through α-CGRP to ILC2s suppresses expression of its receptor in the cells and suggest that an α-CGRP-mediated signaling pathway may regulate intestinal ILC2 activity in type 2 immune responses.

α-CGRP Suppresses Type 2 Inflammation-Induced Activation and Expansion of ILC2s *In Vitro* and *In Vivo*

To determine if α-CGRP can directly trigger signaling in ILC2s and impact their transcriptional states under inflammatory conditions, we performed bulk RNA-seq of KLRG1$^+$ ILC2s isolated from the small intestine and stimulated *in vitro* with IL-25 alone or together with α-CGRP for 3 h. As expected, IL-25 alone induced the expected activation phenotype, including expression of key mitotic genes, such as *Myc*, and type 2 cytokines, such as *Il13* and *Il5* (Figure 4C). We confirmed IL-5 and IL-13 induction at the protein level (Figure 4D).

Continuous exposure to IL-25 was required for the induction of α-CGRP expression in intestinal ILC2s. While *in vitro* stimulation with IL-25 for 3 h did not alter expression of the α-CGRP exon (data now shown), extended stimulation for 24 h significantly induced the exon expression (>6-fold; Figure S4D), consistent with the *in vivo* chronic inflammation model (Figure 4B).

The IL-25-induced activation signature was significantly suppressed when cells were treated with both IL-25 and α-CGRP (Figures 4C and S4E), with the exception of a few genes, notably *Il5*, which was further significantly induced (Figures 4C and D). Moreover, α-CGRP co-treatment significantly suppressed IL-25-induced cell division (Figure 4E). Thus, α-CGRP inhibits proliferation and activation of intestinal KLRG1$^+$ ILC2s but induces expression of key genes, including *Il5* and *Areg* (Figure S4F), highlighting its dual regulatory roles in intestinal ILC2s in the context of IL-25-induced activation.

We next used an IL-25-induced *in vivo* activation model (Huang et al., 2015; Figure 5A) to show that α-CGRP suppresses expansion of ILC2s responding to inflammation. Intraperitoneal administration of α-CGRP into wild-type mice impaired IL-25-induced expansion of KLRG1$^+$ ILC2s (Figures 5B and S5A), consistent with our *in vitro* results. Recent work has shown that intestinal inflammatory ILC2s (KLRG1$^+$ST2$^-$) can migrate to mesenteric lymph nodes (mLNs) and other tissues during inflammation via sphingosine 1-phosphate (S1P)-mediated chemotaxis (Huang et al., 2018). To determine whether α-CGRP primarily impacts intestinal or mLN ILC2s, we relied on the fact that ~90% of intestinal KLRG1$^+$ ILC2s are phenotypically ST2$^-$ (Figure S5B), whereas mLN ILC2s are mainly ST2$^+$ at

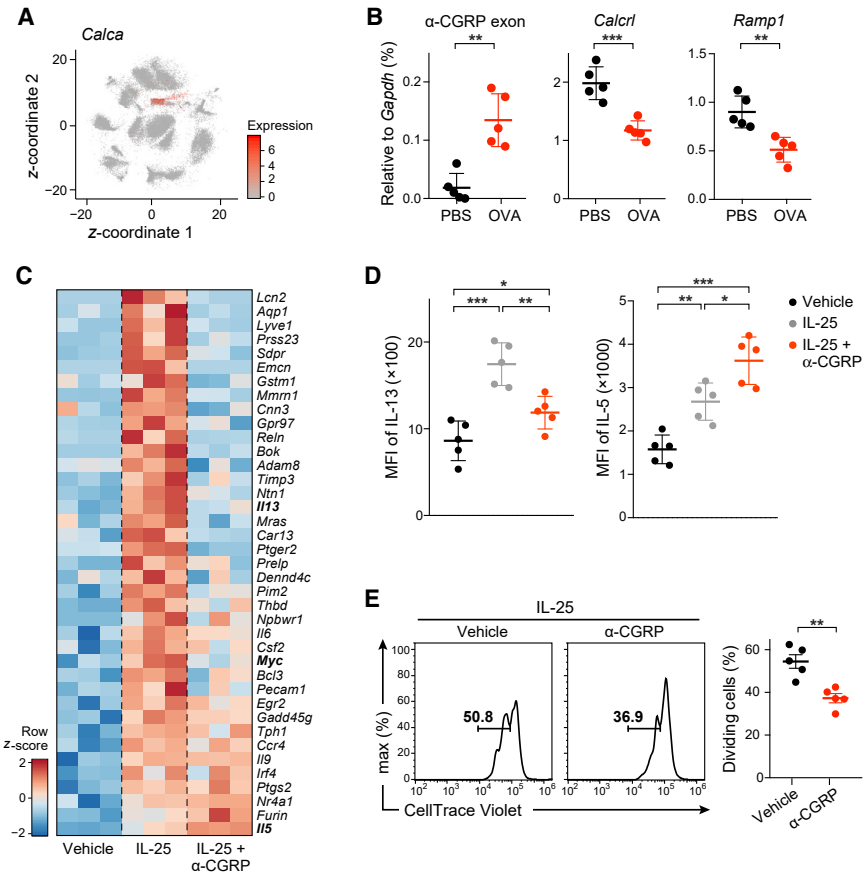


Figure 4. α-CGRP Suppresses IL-25-Induced Activation and Expansion of Intestinal KLRG1$^+$ ILC2s *In Vitro*

(A) Cells expressing the *Calca* gene. 2D embedding as in Figure 1B where cells (dots) are colored by relative expression of *Calca* (log_2(TP10K+1)), where TP10K represents transcripts per 10,000.

(B) α-CGRP exon specifically induced in inflammation. Expression amounts (y axis) of α-CGRP exon of *Calca*, *Calcrl*, and *Ramp1* in LP ILC2s isolated from control (black) or OVA-treated (red) mice on day 36 (Figure S1A). Points represent individual experiments.

(C and D) α-CGRP co-treatment abrogates most of the IL-25-induced response in LP ILC2s *in vitro*. (C) Expression (color bar, *Z* score) of genes (rows) significantly induced in ILC2s (fold change ≥2, $p < 0.05$) by IL-25 compared to control, across different conditions. (D) Intracellular amounts (mean fluorescence intensity [MFI], y axis) of IL-13 and IL-5 in ILC2s following indicated stimulations for 12 h. Points represent individual experiments.

(E) α-CGRP suppresses IL-25-indcued proliferation of LP ILC2s. Left: distribution of the number of cell divisions (y axis, percentage of maximum observed number) monitored by flow cytometry. Right: percentage of dividing cells (y axis) in each treatment (x axis). Points represent individual experiments. Data represent mean ± SEM; *$p < 0.05$, **$p < 0.01$, and ***$p < 0.001$, Student's t test (B, D, and E).

Data are from seven (A) or five (B, D, and E) independent experiments, or representative of two (C) independent experiments.

See also Figure S4.

steady state (Figure 5C). IL-25 administration increased the frequency of both KLRG1$^+$ST2$^-$ inflammatory ILC2s and ST2$^+$ ILC2s in mLNs (Figure 5C—5E and S5C), but co-administration with α-CGRP only reduced the frequency of KLRG1$^+$ST2$^-$ ILC2s (Figures 5C, 5D, and S5C), which are cells that migrated from the small intestine to the mLNs (Huang et al., 2018), but not of ST2$^+$ ILC2s (Figure 5E). Thus, α-CGRP preferentially regulates the response of intestinal KLRG1$^+$ST2$^-$ ILC2s. Furthermore, α-CGRP also significantly suppressed the expansion of intestinal ILC2s in a food allergy model (Figures 5F, 5G, and S5D), where we intragastrically administrated α-CGRP together with OVA into pre-sensitized mice. Importantly, mast cell expansion, the main phenotypic marker of allergic inflammation in this model (Brandt et al., 2003), was significantly suppressed in the presence of α-CGRP (Figure 5H), whereas the frequencies of other major immune cell types remained unchanged (Figure S5E). Taken together, α-CGRP antagonized expansion of intestinal KLRG1$^+$ ILC2s and type 2 inflammation *in vivo*.

At Homeostasis, α-CGRP Is Predominantly Expressed *In Vivo* in Two Subsets of ChAT$^+$ Enteric Neurons

Without inflammation, intestinal KLRG1$^+$ ILC2s expressed CGRP receptors (Figure 4B), but not CGRP, leading us to search for neighboring cell types that potentially produce CGRP at homeostasis. To this end, we analyzed *Calca* gene expression across multiple intestinal scRNA-seq datasets, including our previous epithelial atlas for the mouse small intestine epithelium (Haber et al., 2017; Figure S6A), our intestinal immune atlas here (Figure 1), and scRNA-seq of enteric neurons from Wnt1-Cre:R26Tomato mice (Zeisel et al., 2018; Figures 6A, S6B, and S6C). *Calca* expression was detected in two subsets of ChAT$^+$ enteric neurons (Figures 6B and S6C). These ChAT$^+$ enteric neurons also expressed (Figure 6B): (1) the CGRP receptor genes; (2) the *Calcb* gene, encoding β-CGRP peptide, which differs by two amino acids from α-CGRP but has not been substantially studied for its function in immune cells; and (3) the *Nmu* gene, which we and others have shown amplifies the activity of ILC2s under type 2 inflammation in the lung and small intestine (Cardoso et al., 2017; Klose et al., 2017; Wallrapp et al., 2017).

We confirmed by immunofluorescence staining that ChAT$^+$ enteric neurons expressed CGRP (Figure 6C), and that ILC2s contact with CGRP-expressing neurons at the steady state (Figure S6D), consistent with previous reports that ILC2s are closely associated with neurons in the intestine (Klose et al., 2017). Thus, CGRP from these ChAT$^+$ enteric neurons may regulate ILC2 homeostasis.

α-CGRP Suppresses ILC2 Proliferation through Activating a cAMP Response Module

The presence at homeostasis of α-CGRP receptors on ILC2s and α-CGRP's expression on ChAT$^+$ intestinal neurons led us to hypothesize that α-CGRP has an effect on ILC2s during homeostasis. To test this hypothesis, we next measured the expression profiles of intestinal KLRG1$^+$ ILC2s stimulated

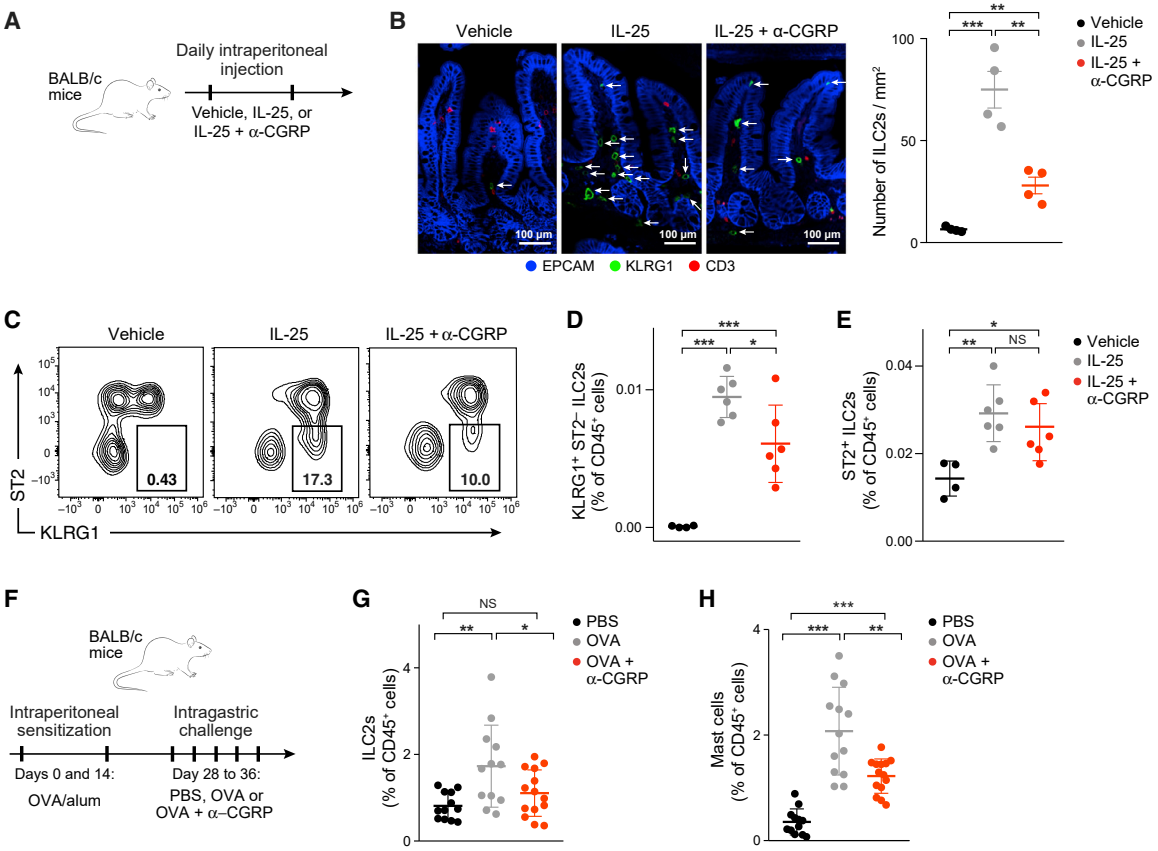


Figure 5. α-CGRP Antagonizes Expansion of Intestinal KLRG1⁺ ILC2s *In Vivo*

(A) Experimental design.

(B) α-CGRP co-treatment antagonizes ILC2 expansion *in vivo*. Representative IF images (left, scale bars, 100 μm) and cell densities (number of cells/mm^2) of CD3$^-$KLRG1$^+$ ILC2 (left, arrows) in the small intestines of mice treated as in (A). Points represent individual mice.

(C–E) α-CGRP antagonizes the expansion of ST2$^-$KLRG1$^+$ ILC2s specifically. (C) Flow cytometry analysis of ILC2s in mLNs gated on CD45$^+$Lin$^-$CD90.2$^+$IL7R$^+$ from mice treated as in (A). (D) Frequency (y axis) of ST2$^-$KLRG1$^+$ ILC2s in total CD45$^+$ cells in mLNs of mice treated as in (A). Points represent individual mice. (E) Frequency (y axis) of ST2$^+$ ILC2s in total CD45$^+$ cells in mLNs of mice treated as in (A). Points represent individual mice.

(F and G) α-CGRP treatment antagonizes LP ILC2 expansion in OVA-induced type 2 inflammatory model. (F) Experimental overview. (G) Percentage of ILC2s (y axis) in total CD45$^+$ cells in mice treated as in (F) on day 36. Points represent individual mice.

(H) α-CGRP treatment suppresses expansion of mast cells in LP in OVA-induced type 2 inflammatory model. Percentage of FceRIa$^+$SiglecF$^{low/-}$Lin^{low} mast cells (y axis) in total CD45$^+$ cells in mice treated as in (F) on day 36. Data represent mean ± SEM; *p < 0.05, **p < 0.01, ***p < 0.001, and NS, p > 0.05, Student's t test (B, D, E, G, and H).

Data are from two (B), three (C–E), or four (G and H) independent experiments.

See also Figure S5.

in vitro by α-CGRP alone and identified genes differentially expressed under this signal (Figure 6D; STAR Methods).

Analyzing the gene expression suggested that α-CGRP activated a cAMP response module. First, α-CGRP stimulation induced expression of key genes involved in adenylate-cyclase-mediated GPCR signaling, including *Adrb2*, *Adora2a*, and *Pde4b* (Figure 6D), as well as cAMP response genes, including *Areg* (Shao and Sheng, 2010), *Crem*, and *Il5* (Figure 6D). Previous studies showed that cAMP directly induces IL-5 expression in ILC2s (Nussbaum et al., 2013). Moreover, assay for transposase-accessible chromatin using sequencing (ATAC-seq) profiling of ILC2s revealed that regions of increased chromatin accessibility following α-CGRP stimulation were enriched for gene loci involved in the adenylate cyclase pathway (Figure 6E; Table S5). Consistently, α-CGRP stimulation alone induced the accumulation of intracellular cAMP in ILC2s (Figure 6F).

α-CGRP stimulation *in vitro* negatively regulated ILC2 proliferation, and this effect may be mediated by induction of genes involved in cell-cycle arrest in the cAMP response module. In our KLRG1$^+$ ILC2 cells, α-CGRP induced expression of genes involved in cell-cycle arrest, such as *Cdkn1a*, *Gadd45a*, and *Akap12*, as well as key negative regulators of ILC2 expansion, *Adrb2* and *Pdcd1* (Moriyama et al., 2018; Taylor et al., 2017; Figure 6D). cAMP and its principal target, cAMP-dependent protein kinase (PKA), have been previously shown to suppress proliferation via negatively regulating mitogen-activated protein (MAP) kinase cascade in a cell-context-dependent manner (Stork and Schmitt, 2002). Indeed, the adenylate cyclase activator forskolin, which increases intracellular cAMP concentrations (Rodriguez

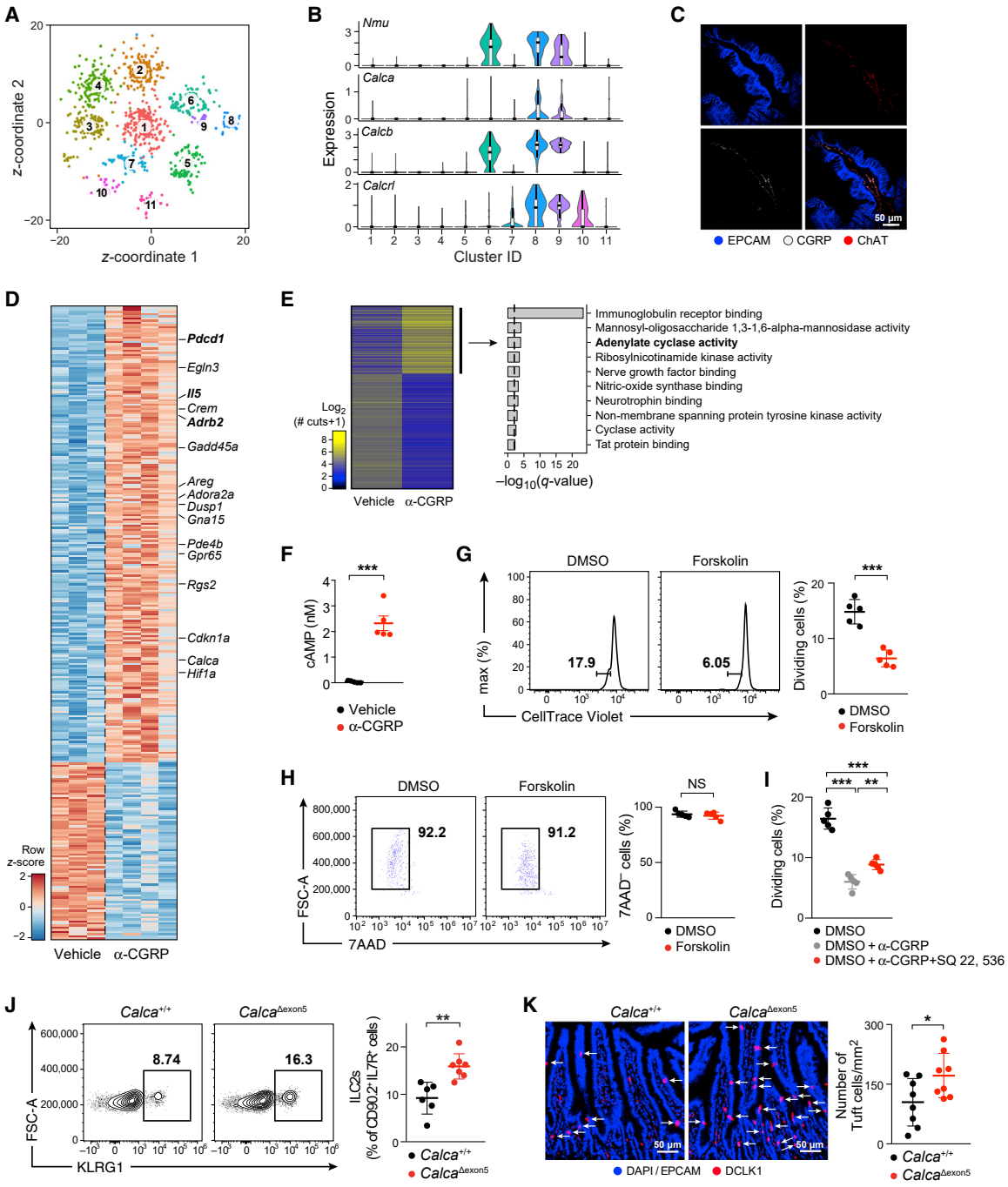


Figure 6. α-CGRP Is Produced by ChAT$^+$ Enteric Neurons in Steady States and Maintains Intestinal KLRG1$^+$ ILC2 Homeostasis *In Vivo*

(A and B) ChAT$^+$ enteric neurons express α-CGRP. (A) t-SNE plot of 1,105 enteric neuron profiles from Wnt1-Cre:R26Tomato mice (Zeisel et al., 2018), where each neuron (dot) is colored by cluster assignment. (B) Distribution of expression amounts (y axis, $\log_2$(TP10K+1)) of *Nmu*, *Calca*, *Calcb*, and *Calcrl* gene in the enteric neurons in each cluster in (A; x axis).

(C) Co-localization of ChAT and CGRP in the small intestines of WT mice. Scale bar, 50 μm.

(D) Expression program induced by α-CGRP in LP ILC2s. Relative expression (row-wise *Z* score of $\log_2$(TPM + 1)) of genes (rows) significantly induced or suppressed by α-CGRP stimulation for 3 h. Key genes are highlighted.

(E) α-CGRP stimulation in ILC2s *in vitro* reprograms chromatin accessibility especially at loci of a cAMP response module. Left: chromatin accessibility ($\log_2$(#cuts+1); STAR Methods) of loci (rows) with differential accessibility in LP ILC2s treated by α-CGRP versus control *in vitro* for 3 h. Right: statistical significance (x axis, $-\log_{10}$(q-value)) of molecular functions (y axis) whose associated genes are enriched in proximity to these differentially accessible ATAC-seq peaks. Dashed line, q value = 0.01.

(legend continued on next page)

et al., 2013), suppressed the proliferation of ILC2s (Figure 6G), but not their viability (Figure 6H). Furthermore, short treatment of ILC2s with a low concentration of adenylate cyclase inhibitor (Klein et al., 2012) preserved cell viability and partially rescued the cell proliferation defect mediated by α-CGRP (Figure 6I). Taken together, our data demonstrate that increased concentration of intracellular cAMP, potentially cooperating with other additional pathways, supports the inhibitory role of α-CGRP in intestinal ILC2 proliferation.

At Homeostasis, α-CGRP Maintains ILC2 and Type 2 Responses *In Vivo*

Finally, we used *Calca*$^{\Delta exon5}$ mice, in which the α-CGRP exon is deficient but the CT exon remains intact (Oh-hashi et al., 2001), as a loss-of-function model to demonstrate α-CGRP-mediated signaling constrains intestinal KLRG1$^+$ ILC2s. The frequency of intestinal ILC2s in *Calca*$^{\Delta exon5}$ mice was increased in the IL-25 induced inflammatory condition (Figure S6E), in line with our observations in gain-of-function models (Figures 5A and 5B). Moreover, the absence of α-CGRP already significantly increased the frequency of intestinal KLRG1$^+$ ILC2s at steady state (Figure 6J). Type 2 cytokines promote differentiation of tuft cells (Biton et al., 2018; Gerbe et al., 2016; Howitt et al., 2016; von Moltke et al., 2016), and consistently, the number of tuft cells, which lack detectable transcription of CGRP receptors (Figure S6A), was significantly increased in *Calca*$^{\Delta exon5}$ mice (Figure 6K). Thus, α-CGRP-mediated signaling helped maintain the homeostasis of KLRG1$^+$ ILC2s and type 2 immunity in the small intestine.

DISCUSSION

Our atlas and analysis revealed a role for α-CGRP in suppressing the expansion of intestinal ILC2s in both IL-25-induced acute inflammation and OVA-induced allergic inflammation models. In acute inflammation, ILC2s are still robustly expanded under co-administration of α-CGRP, likely due to IL-25's exceptional potency as an activator. Previous studies showed that CGRP signaling can generate both pro- and anti-inflammatory immune responses, depending on cell type, tissue, and model (Assas et al., 2014). α-CGRP increases IL-5 expression in lung ILC2s co-stimulated with IL-33 (Sui et al., 2018). Mice with deficiency in CRLR in IL-5-expressing cells manifest a normal frequency of ST2$^+$ ILC2s in lungs exposed to house dust mite (HDM) (Sui et al., 2018), consistent with our finding that ST2$^+$ ILC2s in mLNs are not significantly affected by α-CGRP administration. However, we further revealed that α-CGRP reduced the expansion of intestinal KLRG1$^+$ ILC2s. Thus, our work highlights dual regulatory roles of α-CGRP, which promotes IL-5 production but inhibits expansion of intestinal KLRG1$^+$ ILC2s. Although differences in cell states between lung ST2$^+$ and intestinal ST2$^-$ KLRG1$^+$ ILC2s (Ricardo-Gonzalez et al., 2018) might contribute to their differential reactions to CGRP signaling, additional studies in animal models where CRLR is specifically deleted in intestinal KLRG1$^+$ ILC2s will be needed to elucidate the full molecular mechanism. In addition, it will be important to compare the effects of α-CGRP versus β-CGRP binding to CRLR in ILC2s.

We revealed that two subsets of ChAT$^+$ enteric neurons are the predominant source of CGRP in the small intestine at steady state. In addition to multiple neuropeptides, these ChAT$^+$ neurons expressed *Il13ra1* and *Il4ra* (Figure S6C), which encode the components of the receptor complex for the type 2 cytokine IL-13. Thus, these ChAT$^+$ neurons may be specialized for cross-talk with the immune system. Future studies are needed to determine if cytokine signaling from immune cells during inflammation further boosts the secretion of neuropeptides.

CGRP signaling is an additional key axis of neuro-immune interaction with implications for inflammation, including food allergy. The nervous system exercises dual functions to either activate or inhibit ILC2s via different GPCRs (Cardoso et al., 2017; Klose et al., 2017; Moriyama et al., 2018; Wallrapp et al., 2017). We propose a model for how ILC2s integrate and balance such diverse neural signaling cues, involving different Gα proteins and their downstream signaling. The amplifier NMUR1 mainly signals through $G\alpha_{q/11}$ and inhibits cAMP concentrations (Martinez and O'Driscoll, 2015), whereas the negative regulators CRLR and β_2AR are both coupled with $G\alpha_s$ proteins that activate adenylate cyclase and the cAMP pathway (Chatterjee et al., 1993; Madamanchi, 2007). Intracellular cAMP accumulation induced expression of the cAMP response module, including IL-5, but suppressed ILC2 proliferation. Thus, selective activation of different subgroups of α subunits of G proteins coupled with variable downstream effects, including the concentration of cAMP, might be utilized by ILC2s to fine-tune the response to neuronal signaling.

Our work underscores the importance of α-CGRP modulating ILC2 activity, which may serve as a therapeutic target for treating diseases like food allergy. Since monoclonal antibodies against CGRP have been recently approved to treat migraine

(F) α-CGRP induces intracellular cAMP accumulation in ILC2s. cAMP concentration (μM, y axis) in LP ILC2s stimulated *in vitro* for 30 min as measured by ELISA. Points represent individual mice.

(G and H) Forskolin suppresses ILC2 proliferation but does not impact cell viability.

(G) Left: the number of cell divisions (y axis, percentage of maximum observed number) monitored by flow cytometry in LP ILC2s. Points represent individual experiments.

(H) Cell viability monitored by flow cytometry in cells in (G) stained with 7AAD. Points represent individual experiments.

(I) Adenylate cyclase inhibitor (SQ22, 536) treatment partially rescues α-CGRP inhibition of ILC2 proliferation. Percentage of divided cells (y axis) as assayed as in (F). LP ILC2s treated *in vivo* for 40 h. Points represent individual experiments.

(J and K) The deficiency of α-CGRP affects ILC2 expansion *in vivo*. (J) Left: flow cytometry analysis of LP ILC2s in WT and *Calca*$^{\Delta exon5}$ mice in homeostasis. Points represent individual mice. (K) Left: representative IF images of tuft cells (arrows) in the small intestine of WT or *Calca*$^{\Delta exon5}$ mice. Scale bars, 50 μm. Right: density of tuft cells (y axis, number per mm^2) in WT and *Calca*$^{\Delta exon5}$ mice. Points represent individual mice.

Data represent mean ± SEM; *$p < 0.05$, **$p < 0.01$, ***$p < 0.001$, and NS, $p > 0.05$, Student's t test (F–K). Data are representative of three (C) or two (D) independent experiments or are from one (E), three (F, J, and K), or five (G–I) independent experiments.

See also Figure S6 and Table S5.

(Edvinsson, 2018), it will be important to monitor the incidence of allergic diseases in treated patients. More broadly, our work provides a resource for understanding the intestinal immune system in response to type 2 inflammation in the context of each specific cell type. Further exploration of the atlas can lead to additional hypotheses on circuits within and between additional cell types that contribute to type 2 immune responses.

STAR★METHODS

Detailed methods are provided in the online version of this paper and include the following:

- KEY RESOURCES TABLE
- LEAD CONTACT AND MATERIALS AVAILABILITY
- METHOD DETAILS
  - Mice
  - Isolation of cells from Peyer's patches (PPs)
  - Isolation of cells from the lamina propria (LP)
  - Flow cytometry and cell sorting
  - Droplet-based scRNA-seq
  - Quantitative real-time PCR
  - ILC2 culture
  - Immunofluorescence staining and imaging
  - Bulk RNA-seq
  - Overall Expression analysis
  - Bulk ATAC-seq
  - scRNA-seq data QC and pre-processing
  - Benchmarking different batch correction approaches
  - scRNA-seq clustering of PP cells
  - Clustering cross-validation of PP cells
  - Cluster annotation and filtering of PP cells
  - Clustering LP cells
  - Cellular composition changes
  - Cell sampling frequencies
  - Topic modeling
  - Statistical analysis
- DATA AND CODE AVAILABILITY

SUPPLEMENTAL INFORMATION

Supplemental Information can be found online at https://doi.org/10.1016/j.immuni.2019.09.004.

ACKNOWLEDGMENTS

We thank Leslie Gaffney and Anna Hupalowska for help with figures, Tim Tickle for help with the Single Cell Portal, Miao Xu and Chao Huang for help with tissue harvest, Yan Wang for help with qPCR, Hans Oettgen for discussions, Hiroki Kurihara for donating the B6.129S6-Calca < tm1Hku > strain to a publicly available repository, the Broad Flow Cytometry Facility, and the Flow Cytometry Core and Laboratory Animal Resources Center in Westlake University. Work was supported by the Food Allergy Science Initiative, NIH grant DK114784 (A.R. and R.J.X.), NIH grant DK 043351, the Crohn's & Colitis Foundation (R.J.X.), the National Natural Science Foundation of China (grant 31970842; H.X.), the Westlake Education Foundation of Westlake University (H.X.), and the Klarman Cell Observatory and HHMI (A.R.).

AUTHOR CONTRIBUTIONS

H.X., R.J.X., and A.R. conceived and supervised this study. H.X. designed and performed all experiments. J.D. performed computational analysis with contributions from C.B.M.P., H.X., O.A., M.T., and R.J.X. and guidance from A.R.. A.W., X.G., S.F., C.S., P.R.B., H.N.S., and V.K.K. helped with animal work. S.M. assisted with ATAC-seq. D.D., L.T.N., and O.R.-R. assisted with scRNA-seq. A.L. assisted with bulk RNA-seq. H.X., J.D., A.R., and R.J.X. wrote the manuscript with input from all authors.

DECLARATION OF INTERESTS

A.R. is a scientific advisory board member of ThermoFisher Scientific, Neogene Therapeutics, and Syros Pharmaceuticals. A.R. and R.J.X. are co-founders of and equity holders in Celsius Therapeutics. H.X., R.J.X., and A.R. are co-inventors on US provisional patent application no. 62/667,381 filed by The Broad Institute relating to the subject matter of this manuscript. A.R., H.X., J.D., and R.J.X. are co-inventors on US provisional patent application no 62/818,404 filed by the Broad Institute relating to CGRP signaling modulation.

Received: May 29, 2019
Revised: August 6, 2019
Accepted: September 6, 2019
Published: October 15, 2019

REFERENCES

Amara, S.G., Jonas, V., Rosenfeld, M.G., Ong, E.S., and Evans, R.M. (1982). Alternative RNA processing in calcitonin gene expression generates mRNAs encoding different polypeptide products. Nature *298*, 240–244.

Artis, D., and Spits, H. (2015). The biology of innate lymphoid cells. Nature *517*, 293–301.

Assas, B.M., Pennock, J.I., and Miyan, J.A. (2014). Calcitonin gene-related peptide is a key neurotransmitter in the neuro-immune axis. Front. Neurosci. *8*, 23.

Bielecki, P., Riesenfeld, S.J., Kowalczyk, M.S., Amezcua Vesely, M.C., Kroehling, L., Yaghoubi, P., Dionne, D., Jarret, A., Steach, H.R., McGee, H.M., et al. (2018). Skin inflammation driven by differentiation of quiescent tissue-resident ILCs into a spectrum of pathogenic effectors. bioRxiv. bioRxiv. https://doi.org/10.1101/461228.

Biton, M., Haber, A.L., Rogel, N., Burgin, G., Beyaz, S., Schnell, A., Ashenberg, O., Su, C.W., Smillie, C., Shekhar, K., et al. (2018). T helper cell cytokines modulate intestinal stem cell renewal and differentiation. Cell *175*, 1307–1320.e1322.

Blei, D.M., Ng, A.Y., and Jordan, M.I. (2003). Latent Dirichlet allocation. J. Mach. Learn. Res. *3*, 993–1022.

Blondel, V.D., Guillaume, T.J., Lambiotte, R., and Lefebvre, E. (2008). Fast unfolding of communities in large networks. J. Stat. Mech. *2008*, 10008.

Brandt, E.B., Strait, R.T., Hershko, D., Wang, Q., Muntel, E.E., Scribner, T.A., Zimmermann, N., Finkelman, F.D., and Rothenberg, M.E. (2003). Mast cells are required for experimental oral allergen-induced diarrhea. J. Clin. Invest. *112*, 1666–1677.

Buenrostro, J.D., Giresi, P.G., Zaba, L.C., Chang, H.Y., and Greenleaf, W.J. (2013). Transposition of native chromatin for fast and sensitive epigenomic profiling of open chromatin, DNA-binding proteins and nucleosome position. Nat. Methods *10*, 1213–1218.

Burton, O.T., Medina Tamayo, J., Stranks, A.J., Miller, S., Koleoglou, K.J., Weinberg, E.O., and Oettgen, H.C. (2018). IgE promotes type 2 innate lymphoid cells in murine food allergy. Clin. Exp. Allergy *48*, 288–296.

Butler, A., Hoffman, P., Smibert, P., Papalexi, E., and Satija, R. (2018). Integrating single-cell transcriptomic data across different conditions, technologies, and species. Nat. Biotechnol. *36*, 411–420.

Cardoso, V., Chesné, J., Ribeiro, H., García-Cassani, B., Carvalho, T., Bouchery, T., Shah, K., Barbosa-Morais, N.L., Harris, N., and Veiga-Fernandes, H. (2017). Neuronal regulation of type 2 innate lymphoid cells via neuromedin U. Nature *549*, 277–281.

Chatterjee, T.K., Moy, J.A., Cai, J.J., Lee, H.C., and Fisher, R.A. (1993). Solubilization and characterization of a guanine nucleotide-sensitive form of the calcitonin gene-related peptide receptor. Mol. Pharmacol. *43*, 167–175.

Chen, C., Grennan, K., Badner, J., Zhang, D., Gershon, E., Jin, L., and Liu, C. (2011). Removing batch effects in analysis of expression microarray data: an evaluation of six batch adjustment methods. PLoS ONE *6*, e17238.

Dey, K.K., Hsiao, C.J., and Stephens, M. (2017). Visualizing the structure of RNA-seq expression data using grade of membership models. PLoS Genet. *13*, e1006599.

Ding, J., Condon, A., and Shah, S.P. (2018). Interpretable dimensionality reduction of single cell transcriptome data with deep generative models. Nat. Commun. *9*, 2002.

Ding, J., Shah, S., and Condon, A. (2016). densityCut: an efficient and versatile topological approach for automatic clustering of biological data. Bioinformatics *32*, 2567–2576.

Dobin, A., Davis, C.A., Schlesinger, F., Drenkow, J., Zaleski, C., Jha, S., Batut, P., Chaisson, M., and Gingeras, T.R. (2013). STAR: ultrafast universal RNA-seq aligner. Bioinformatics *29*, 15–21.

Dumais, S.T., Furnas, G.W., Landauer, T.K., and Harshman, R. (1990). Indexing by latent semantic analysis. J. Am. Soc. Inf. Sci. *41*, 391–407.

duVerle, D.A., Yotsukura, S., Nomura, S., Aburatani, H., and Tsuda, K. (2016). CellTree: an R/bioconductor package to infer the hierarchical structure of cell populations from single-cell RNA-seq data. BMC Bioinformatics *17*, 363.

Edvinsson, L. (2018). CGRP antibodies as prophylaxis in migraine. Cell *175*, 1719.

Finak, G., McDavid, A., Yajima, M., Deng, J., Gersuk, V., Shalek, A.K., Slichter, C.K., Miller, H.W., McElrath, M.J., Prlic, M., et al. (2015). MAST: a flexible statistical framework for assessing transcriptional changes and characterizing heterogeneity in single-cell RNA sequencing data. Genome Biol. *16*, 278.

Gerbe, F., Sidot, E., Smyth, D.J., Ohmoto, M., Matsumoto, I., Dardalhon, V., Cesses, P., Garnier, L., Pouzolles, M., Brulin, B., et al. (2016). Intestinal epithelial tuft cells initiate type 2 mucosal immunity to helminth parasites. Nature *529*, 226–230.

Gieseck, R.L., 3rd, Wilson, M.S., and Wynn, T.A. (2018). Type 2 immunity in tissue repair and fibrosis. Nat. Rev. Immunol. *18*, 62–76.

Haber, A.L., Biton, M., Rogel, N., Herbst, R.H., Shekhar, K., Smillie, C., Burgin, G., Delorey, T.M., Howitt, M.R., Katz, Y., et al. (2017). A single-cell survey of the small intestinal epithelium. Nature *551*, 333–339.

Haghverdi, L., Lun, A.T.L., Morgan, M.D., and Marioni, J.C. (2018). Batch effects in single-cell RNA-sequencing data are corrected by matching mutual nearest neighbors. Nat. Biotechnol. *36*, 421–427.

Hammad, H., and Lambrecht, B.N. (2015). Barrier epithelial cells and the control of Type 2 immunity. Immunity *43*, 29–40.

Heng, T.S., and Painter, M.W.; Immunological Genome Project Consortium (2008). The Immunological Genome Project: networks of gene expression in immune cells. Nat. Immunol. *9*, 1091–1094.

Hepworth, M.R., Monticelli, L.A., Fung, T.C., Ziegler, C.G., Grunberg, S., Sinha, R., Mantegazza, A.R., Ma, H.L., Crawford, A., Angelosanto, J.M., et al. (2013). Innate lymphoid cells regulate CD4+ T-cell responses to intestinal commensal bacteria. Nature *498*, 113–117.

Howitt, M.R., Lavoie, S., Michaud, M., Blum, A.M., Tran, S.V., Weinstock, J.V., Gallini, C.A., Redding, K., Margolskee, R.F., Osborne, L.C., et al. (2016). Tuft cells, taste-chemosensory cells, orchestrate parasite type 2 immunity in the gut. Science *351*, 1329–1333.

Huang, Y., Guo, L., Qiu, J., Chen, X., Hu-Li, J., Siebenlist, U., Williamson, P.R., Urban, J.F., Jr., and Paul, W.E. (2015). IL-25-responsive, lineage-negative KLRG1(hi) cells are multipotential 'inflammatory' type 2 innate lymphoid cells. Nat. Immunol. *16*, 161–169.

Huang, Y., Mao, K., Chen, X., Sun, M.A., Kawabe, T., Li, W., Usher, N., Zhu, J., Urban, J.F., Jr., Paul, W.E., and Germain, R.N. (2018). S1P-dependent interorgan trafficking of group 2 innate lymphoid cells supports host defense. Science *359*, 114–119.

Jerby-Arnon, L., Shah, P., Cuoco, M.S., Rodman, C., Su, M.J., Melms, J.C., Leeson, R., Kanodia, A., Mei, S., Lin, J.R., et al. (2018). A cancer cell program promotes T cell exclusion and resistance to checkpoint blockade. Cell *175*, 984–997.e924.

Klein, M., Vaeth, M., Scheel, T., Grabbe, S., Baumgrass, R., Berberich-Siebelt, F., Bopp, T., Schmitt, E., and Becker, C. (2012). Repression of cyclic adenosine monophosphate upregulation disarms and expands human regulatory T cells. J. Immunol. *188*, 1091–1097.

Kloepfer, K.M., Olenec, J.P., Lee, W.M., Liu, G., Vrtis, R.F., Roberg, K.A., Evans, M.D., Gangnon, R.E., Lemanske, R.F., Jr., and Gern, J.E. (2012). Increased H1N1 infection rate in children with asthma. Am. J. Respir. Crit. Care Med. *185*, 1275–1279.

Klose, C.S.N., Mahlakõiv, T., Moeller, J.B., Rankin, L.C., Flamar, A.L., Kabata, H., Monticelli, L.A., Moriyama, S., Putzel, G.G., Rakhilin, N., et al. (2017). The neuropeptide neuromedin U stimulates innate lymphoid cells and type 2 inflammation. Nature *549*, 282–286.

Korsunsky, I., Fan, J., Slowikowski, K., Zhang, F., Wei, K., Baglaenko, Y., Brenner, M., Loh, P.-R., and Raychaudhuri, S. (2018). Fast, sensitive, and accurate integration of single cell data with Harmony. bioRxiv. https://doi.org/10.1101/461954.

Kotas, M.E., and Locksley, R.M. (2018). Why innate lymphoid cells? Immunity *48*, 1081–1090.

Langmead, B., and Salzberg, S.L. (2012). Fast gapped-read alignment with Bowtie 2. Nat. Methods *9*, 357–359.

Levine, J.H., Simonds, E.F., Bendall, S.C., Davis, K.L., Amir, A.D., Tadmor, M.D., Litvin, O., Fienberg, H.G., Jager, A., Zunder, E.R., et al. (2015). Data-driven phenotypic dissection of AML reveals progenitor-like cells that correlate with prognosis. Cell *162*, 184–197.

Li, B., and Dewey, C.N. (2011). RSEM: accurate transcript quantification from RNA-seq data with or without a reference genome. BMC Bioinformatics *12*, 323.

Liao, Y., Smyth, G.K., and Shi, W. (2014). featureCounts: an efficient general purpose program for assigning sequence reads to genomic features. Bioinformatics *30*, 923–930.

Locksley, R.M. (2010). Asthma and allergic inflammation. Cell *140*, 777–783.

Lopez, R., Regier, J., Cole, M.B., Jordan, M.I., and Yosef, N. (2018). Deep generative modeling for single-cell transcriptomics. Nat. Methods *15*, 1053–1058.

Madamanchi, A. (2007). Beta-adrenergic receptor signaling in cardiac function and heart failure. McGill J. Med. *10*, 99–104.

Manis, J.P., Tian, M., and Alt, F.W. (2002). Mechanism and control of class-switch recombination. Trends Immunol. *23*, 31–39.

Martinez, V.G., and O'Driscoll, L. (2015). Neuromedin U: a multifunctional neuropeptide with pleiotropic roles. Clin. Chem. *61*, 471–482.

McLean, C.Y., Bristor, D., Hiller, M., Clarke, S.L., Schaar, B.T., Lowe, C.B., Wenger, A.M., and Bejerano, G. (2010). GREAT improves functional interpretation of cis-regulatory regions. Nat. Biotechnol. *28*, 495–501.

Molofsky, A.B., Savage, A.K., and Locksley, R.M. (2015). Interleukin-33 in tissue homeostasis, injury, and inflammation. Immunity *42*, 1005–1019.

Moriyama, S., Brestoff, J.R., Flamar, A.L., Moeller, J.B., Klose, C.S.N., Rankin, L.C., Yudanin, N.A., Monticelli, L.A., Putzel, G.G., Rodewald, H.R., and Artis, D. (2018). β_2-adrenergic receptor-mediated negative regulation of group 2 innate lymphoid cell responses. Science *359*, 1056–1061.

Mowat, A.M., and Agace, W.W. (2014). Regional specialization within the intestinal immune system. Nat. Rev. Immunol. *14*, 667–685.

Neill, D.R., Wong, S.H., Bellosi, A., Flynn, R.J., Daly, M., Langford, T.K., Bucks, C., Kane, C.M., Fallon, P.G., Pannell, R., et al. (2010). Nuocytes represent a new innate effector leukocyte that mediates type-2 immunity. Nature *464*, 1367–1370.

Nussbaum, J.C., Van Dyken, S.J., von Moltke, J., Cheng, L.E., Mohapatra, A., Molofsky, A.B., Thornton, E.E., Krummel, M.F., Chawla, A., Liang, H.E., and Locksley, R.M. (2013). Type 2 innate lymphoid cells control eosinophil homeostasis. Nature *502*, 245–248.

Oh-hashi, Y., Shindo, T., Kurihara, Y., Imai, T., Wang, Y., Morita, H., Imai, Y., Kayaba, Y., Nishimatsu, H., Suematsu, Y., et al. (2001). Elevated sympathetic nervous activity in mice deficient in alphaCGRP. Circ. Res. *89*, 983–990.

Painter, M.W., Davis, S., Hardy, R.R., Mathis, D., and Benoist, C.; Immunological Genome Project Consortium (2011). Transcriptomes of the

B and T lineages compared by multiplatform microarray profiling. J. Immunol. *186*, 3047–3057.

Picelli, S., Björklund, A.K., Faridani, O.R., Sagasser, S., Winberg, G., and Sandberg, R. (2013). Smart-seq2 for sensitive full-length transcriptome profiling in single cells. Nat. Methods *10*, 1096–1098.

Price, A.E., Liang, H.E., Sullivan, B.M., Reinhardt, R.L., Eisley, C.J., Erle, D.J., and Locksley, R.M. (2010). Systemically dispersed innate IL-13-expressing cells in type 2 immunity. Proc. Natl. Acad. Sci. USA *107*, 11489–11494.

Pulendran, B., and Artis, D. (2012). New paradigms in type 2 immunity. Science *337*, 431–435.

Ricardo-Gonzalez, R.R., Van Dyken, S.J., Schneider, C., Lee, J., Nussbaum, J.C., Liang, H.E., Vaka, D., Eckalbar, W.L., Molofsky, A.B., Erle, D.J., and Locksley, R.M. (2018). Tissue signals imprint ILC2 identity with anticipatory function. Nat. Immunol. *19*, 1093–1099.

Robinette, M.L., Fuchs, A., Cortez, V.S., Lee, J.S., Wang, Y., Durum, S.K., Gilfillan, S., and Colonna, M.; Immunological Genome Consortium (2015). Transcriptional programs define molecular characteristics of innate lymphoid cell classes and subsets. Nat. Immunol. *16*, 306–317.

Robinson, M.D., McCarthy, D.J., and Smyth, G.K. (2010). edgeR: a Bioconductor package for differential expression analysis of digital gene expression data. Bioinformatics *26*, 139–140.

Rodriguez, G., Ross, J.A., Nagy, Z.S., and Kirken, R.A. (2013). Forskolin-inducible cAMP pathway negatively regulates T-cell proliferation by uncoupling the interleukin-2 receptor complex. J. Biol. Chem. *288*, 7137–7146.

Rowe, R.K., and Gill, M.A. (2015). Asthma: the interplay between viral infections and allergic diseases. Immunol. Allergy Clin. North Am. *35*, 115–127.

Rydyznski, C.E., Cranert, S.A., Zhou, J.Q., Xu, H., Kleinstein, S.H., Singh, H., and Waggoner, S.N. (2018). Affinity maturation is impaired by natural killer cell suppression of germinal centers. Cell Rep. *24*, 3367–3373.e3364.

Schep, A.N., Wu, B., Buenrostro, J.D., and Greenleaf, W.J. (2017). chromVAR: inferring transcription-factor-associated accessibility from single-cell epigenomic data. Nat. Methods *14*, 975–978.

Schneider, C.A., Rasband, W.S., and Eliceiri, K.W. (2012). NIH Image to ImageJ: 25 years of image analysis. Nat. Methods *9*, 671–675.

Shao, J., and Sheng, H. (2010). Amphiregulin promotes intestinal epithelial regeneration: roles of intestinal subepithelial myofibroblasts. Endocrinology *151*, 3728–3737.

Soneson, C., and Robinson, M.D. (2018). Bias, robustness and scalability in single-cell differential expression analysis. Nat. Methods *15*, 255–261.

Spencer, S.P., Wilhelm, C., Yang, Q., Hall, J.A., Bouladoux, N., Boyd, A., Nutman, T.B., Urban, J.F., Jr., Wang, J., Ramalingam, T.R., et al. (2014). Adaptation of innate lymphoid cells to a micronutrient deficiency promotes type 2 barrier immunity. Science *343*, 432–437.

Stork, P.J., and Schmitt, J.M. (2002). Crosstalk between cAMP and MAP kinase signaling in the regulation of cell proliferation. Trends Cell Biol. *12*, 258–266.

Sui, P., Wiesner, D.L., Xu, J., Zhang, Y., Lee, J., Van Dyken, S., Lashua, A., Yu, C., Klein, B.S., Locksley, R.M., et al. (2018). Pulmonary neuroendocrine cells amplify allergic asthma responses. Science *360*, eaan8546.

Tanay, A., and Regev, A. (2017). Scaling single-cell genomics from phenomenology to mechanism. Nature *541*, 331–338.

Taylor, S., Huang, Y., Mallett, G., Stathopoulou, C., Felizardo, T.C., Sun, M.A., Martin, E.L., Zhu, N., Woodward, E.L., Elias, M.S., et al. (2017). PD-1 regulates KLRG1^{+} group 2 innate lymphoid cells. J. Exp. Med. *214*, 1663–1678.

Tordesillas, L., Berin, M.C., and Sampson, H.A. (2017). Immunology of food allergy. Immunity *47*, 32–50.

von Moltke, J., Ji, M., Liang, H.E., and Locksley, R.M. (2016). Tuft-cell-derived IL-25 regulates an intestinal ILC2-epithelial response circuit. Nature *529*, 221–225.

Wagner, A., Regev, A., and Yosef, N. (2016). Revealing the vectors of cellular identity with single-cell genomics. Nat. Biotechnol. *34*, 1145–1160.

Wallrapp, A., Riesenfeld, S.J., Burkett, P.R., Abdulnour, R.E., Nyman, J., Dionne, D., Hofree, M., Cuoco, M.S., Rodman, C., Farouq, D., et al. (2017). The neuropeptide NMU amplifies ILC2-driven allergic lung inflammation. Nature *549*, 351–356.

Welch, J.D., Kozareva, V., Ferreira, A., Vanderburg, C., Martin, C., and Macosko, E.Z. (2019). Single-cell multi-omic integration compares and contrasts features of brain cell identity. Cell *177*, 1873–1887.e1817.

Wolock, S.L., Lopez, R., and Klein, A.M. (2019). Scrublet: computational identification of cell doublets in single-cell transcriptomic data. Cell Syst. *8*, 281–291.e289.

Zeisel, A., Hochgerner, H., Lonnerberg, P., Johnsson, A., Memic, F., van der Zwan, J., Haring, M., Braun, E., Borm, L.E., La Manno, G., et al. (2018). Molecular architecture of the mouse nervous system. Cell *174*, 999–1014.e1022.

Zhang, Y., Liu, T., Meyer, C.A., Eeckhoute, J., Johnson, D.S., Bernstein, B.E., Nusbaum, C., Myers, R.M., Brown, M., Li, W., and Liu, X.S. (2008). Model-based analysis of ChIP-Seq (MACS). Genome Biol. *9*, R137.

STAR★METHODS

KEY RESOURCES TABLE

REAGENT or RESOURCE	SOURCE	IDENTIFIER
Antibodies		
rat anti-CD16/CD32 (2.4G2)	BD Biosciences	Cat# 553141; RRID: AB_394656
armenian hamster anti-CD3ε (145-2C11), APC	BioLegend	Cat# 100312; RRID: AB_312677
rat anti-CD5 (53-7.3), APC	BioLegend	Cat# 100626; RRID: AB_2563929
rat anti-CD19 (6D5), APC	BioLegend	Cat# 115512; RRID: AB_313647
rat anti-CD11b (M1/70), APC	BioLegend	Cat# 101212; RRID: AB_312795
rat anti-CD8 (53-6.7), APC	BioLegend	Cat# 100712; RRID: AB_312751
armenian hamster anti-CD11c (N418), APC	BioLegend	Cat# 117310; RRID: AB_313779
rat anti-Gr-1 (RB6-8C5), APC	BioLegend	Cat# 108412; RRID: AB_313377
armenian hamster anti-TCRγδ (eBioGL3), APC	Thermo Fisher Scientific	Cat# 17-5711-82; RRID: AB_842756
rat anti-CD170 (1RNM44N), eFluor 660	Thermo Fisher Scientific	Cat# 50-1702-80; RRID: AB_2574186
syrian hamster anti-KLRG1 (2F1), FITC	BioLegend	Cat# 138410; RRID: AB_10643582
rat anti-CD45 (30-F11), Alexa Fluor 594	BioLegend	Cat# 103128; RRID: AB_493715
rat anti-CD127 (A7R34), PE/CY7	BioLegend	Cat# 135014; RRID: AB_1937265
rat anti-CCR6 (29-2L17), BV421	BD Biosciences	Cat# 564736; RRID: AB_2738926
armenian hamster anti-TCRβ (H57-597), APC	Thermo Fisher Scientific	Cat# 17-5961-82; RRID: AB_469481
rat anti-NKp46 (29A1.4), PerCP/Cyanine5.5	BioLegend	Cat# 137609; RRID: AB_10642684
rat anti-CD90.2 (53-2.1), Brilliant Violet 605	BioLegend	Cat# 105343; RRID: AB_2632889
armenian hamster anti-FcεRI (Mar-1), Alexa Fluor 488	BioLegend	Cat# 134330; RRID: AB_2687239
rat anti-IgD (11-26c.2a), Alexa Fluor 594	BioLegend	Cat# 405740; RRID: AB_2565572
rat anti-GATA-3 (TWAJ), Alexa Fluor 488	Thermo Fisher Scientific	Cat# 53-9966-42; RRID: AB_2574493
rat anti-RORγt (B2D), PE	Thermo Fisher Scientific	Cat# 12-6981-82; RRID: AB_10807092
rat anti-IgD (11-26c.2a), Alexa Fluor 647	BioLegend	Cat# 405708; RRID: AB_893528
rat anti-IgD (11-26.2a), Alexa Fluor 594	BioLegend	Cat# 405740; RRID: AB_2565572
rat anti-CD138 (281-2), Alexa Fluor 647	BioLegend	Cat# 142525; RRID: AB_2566238
rat anti-GL7 (GL7), Alexa Fluor 488	Thermo Fisher Scientific	Cat# 53-5902-82; RRID: AB_2016717
rat anti-CD326 (EpCAM), eFluor 450	Thermo Fisher Scientific	Cat# 48-5791-82; RRID: AB_10717090
rat anti-CD3ε (17A2), Alexa Fluor 594	BioLegend	Cat# 152317; RRID: AB_2715809
rat anti-Podoplanin (eBio8.1.1), Alexa Fluor 488	BioLegend	Cat# 337005; RRID: AB_2161952
rat anti-CCL21/6Ckine (59106)	R&D Systems	Cat# MAB457; RRID: AB_2259799
rat anti-IL-13 (eBio13A), eFuor450	Thermo Fisher Scientific	Cat# 12-7133-41; RRID: AB_10852712
rat anti-IL-5 (TRFK5), eFuor450	BioLegend	Cat# 504311; RRID: AB_2563161
goat anti-IL-33	R&D Systems	Cat# AF3626; RRID: AB_884269
syrian hamster anti-KLRG1 (2F1)	BD Biosciences	Cat# 562190; RRID: AB_11154418
rat anti-CGRP	Sigma-Aldrich	Cat# C8198; RRID: AB_259091
rabbit anti-DCAMKL1	Abcam	Cat# ab31704; RRID: AB_873537
donkey anti-goat IgG, Alexa Fluor 647	Thermo Fisher Scientific	Cat# A-21447; RRID: AB_2535864
donkey Anti-Rat IgG, Cy3	Jackson ImmunoResearch	Cat# 712-166-153; RRID: AB_2340669
goat anti-syrian hamster IgG, Alexa Fluor 488	Jackson ImmunoResearch	Cat# 107-546-142; RRID: AB_2337479
goat anti-rabbit IgG, Alexa Fluor 647	Jackson ImmunoResearch	Cat# 111-606-144; RRID: AB_2338083
rat anti-T1/ST2 (DJ8), PE	mdbioproducts	Cat# 101001PE
goat anti-ChAT	Sigma-Aldrich	Cat# AB144P
Chemicals, Peptides, and Recombinant Proteins		
DAPI	Sigma-Aldrich	Cat# D9542
7-AAD	BD Biosciences	Cat# 559925

(*Continued on next page*)

Continued

REAGENT or RESOURCE	SOURCE	IDENTIFIER
Fixable Viability Dye eFluor 780	Thermo Fisher Scientific	Cat# 65-0865-14
UltraPure 0.5M EDTA, pH 8.0	Thermo Fisher Scientific	Cat# 15575020
Ovalbumin	Sigma-Aldrich	Cat# A5503
aluminum potassium sulfate dodecahydrate	Sigma-Aldrich	Cat# A7210-500G
α-CGRP	AnaSpec	Cat# AS-20681
Recombinant Mouse IL-17E Protein	R&D Systems	Cat# 1399-IL-025
DNase I, grade II, from bovine pancreas	Sigma-Aldrich	Cat# 10104159001
RPMI-1640	Thermo Fisher Scientific	Cat# 72400-047
Liberase TM	Sigma-Aldrich	Cat# 5401127001
Percoll Plus	Sigma-Aldrich	Cat# GE17-5445-01
10X Chromium Single Cell 3′ Kit	10X Genomics	Cat#120237
PicoPure RNA Isolation Kit	Thermo Fisher Scientific	Cat# KIT0204
iScript cDNA Synthesis Kit	Bio-Rad	Cat# 1708891
iTaq Universal SYBR® Green Supermix	Bio-Rad	Cat# 1725121
Recombinant Mouse IL-2 Protein	R&D Systems	Cat# 402-ML-020
Recombinant Mouse IL-7 Protein	R&D Systems	Cat# 407-ML-025
CellTrace Violet Cell Proliferation Kit	Thermo Fisher Scientific	Cat# C34557
O.C.T. Compound	Electron Microscopy Sciences	Cat# 62550-01
Triton X-100	Sigma-Aldrich	Cat# T8787
Normal Donkey Serum	Jackson ImmunoResearch	Cat# 017-000-001; RRID: AB_2337254
ProlongGold Antifade reagent	Thermo Fisher Scientific	Cat# P36930
TCL buffer (QIAGEN)	QIAGEN	Cat# 1031576
2-Mercaptoethanol	Sigma-Aldrich	Cat# M6250
GIBCO 2-Mercaptoethanol	Thermo Fisher Scientific	Cat# 21985023
Penicillin Streptomycin	Thermo Fisher Scientific	Cat# 15070063
Sodium Pyruvate	Thermo Fisher Scientific	Cat# 11360070
Nextera XT Sample Preparation Kit	Illumina	Cat#FC-131-1096
forskolin	STEMCELL technologies	Cat#72112
SQ22,536	TOCRIS	Cat# 1435
Cyclic AMP XP® Chemiluminescent Assay Kit	Cell Signaling technology	#8019
Deposited Data		
RNA-seq data	This paper	GEO: GSE124880
Experimental Models: Strains		
Mouse: BALB/cJ	Jackson Laboratory	Cat# JAX:000651; RRID: IMSR_JAX:000651
Mouse: B6.129S6-Calca < tm1Hku >	Brigham and Women's Hospital	Cat# RBRC04109; RRID: IMSR_RBRC04109
Oligonucleotides		
Reverse Transcription DNA oligonucleotide primer (RNase-free, 100 mM)	IDT	5′-AAGCAGTGGTATCAACGCAGAGTACT(30)VN-3′
SMARTER TSO (with LNA)	Exiqon	5′-AAGCAGTGGTATCAACGCAGAGTACrGrG+G-3′
PCR oligonucleotide primer	IDT	5′-AAGCAGTGGTATCAACGCAGAGT-3′
Calcrl-F	Sigma-Aldrich	5′-GCGTGAACCAAACAGACTTG-3′
Calcrl-R	Sigma-Aldrich	5′-TCATTCCAGCATAGCCATCC-3′
Ramp1-F	Sigma-Aldrich	5′-GGCTCTGCTTGCCATGG-3′
Ramp1-R	Sigma-Aldrich	5′-CCTTGAAGCGGCTGAGG-3′
Calca-F	Sigma-Aldrich	5′-TGCAGATGAAAGCCAGGG-3′
Calca-R-exon 5	Sigma-Aldrich	5′-CTTCACCACACCTCCTGATC-3′
Calca-R-exon 4	Sigma-Aldrich	5′-TGTTGAGGTCTTGTGTGTACG-3′
Calcr-F	Sigma-Aldrich	5′-CTACTTCTGGATGCTCTGCG-3′
Calcr-R	Sigma-Aldrich	5′-AGTGATGGCGTGGATAATGG-3′

(*Continued on next page*)

Continued

REAGENT or RESOURCE	SOURCE	IDENTIFIER
Gapdh-F	Sigma-Aldrich	5′-CTTTGTCAAGCTCATTTCCTGG-3′
Gapdh-R	Sigma-Aldrich	5′-TCTTGCTCAGTGTCCTTGC-3′
Software and Algorithms		
ImageJ	(Schneider et al., 2012)	https://imagej.nih.gov/ij/
GraphPad Prism	GraphPad Software	https://www.graphpad.com/scientific-software/prism/
FlowJo	TreeStar	https://www.flowjo.com/solutions/flowjo
STAR v2.6.0c	(Dobin et al., 2013)	https://github.com/alexdobin/STAR
10x Cell Ranger v2.1.1	10X Genomics	https://support.10xgenomics.com/single-cell/software/overview/welcome
RSEM v1.2.8	(Li and Dewey, 2011)	http://deweylab.github.io/RSEM/
edgeR v3.5.2	(Robinson et al., 2010)	https://gist.github.com/jdblischak/11384914
scvis v0.1.0	(Ding et al., 2018)	https://bitbucket.org/jerry00/scvis-dev/src/master/
LIGER v1.0	(Welch et al., 2019)	https://github.com/MacoskoLab/liger
Harmony v0.1.0	(Korsunsky et al., 2018)	https://github.com/immunogenomics/harmony
scVI v0.3.0	(Lopez et al., 2018)	https://github.com/YosefLab/scVI
Seurat v2.3.3	(Butler et al., 2018)	https://github.com/satijalab/seurat
Phenograph v0.99.1	(Levine et al., 2015)	https://github.com/JinmiaoChenLab/Rphenograph
densityCut v0.0.1	(Ding et al., 2016)	https://bitbucket.org/jerry00/densitycut_dev/src/master/
code for single-cell RNA-seq analysis	This paper	https://bitbucket.org/jerry00/mouse_small_intestine_immune_cell_atlas/src/master/

LEAD CONTACT AND MATERIALS AVAILABILITY

Further information and requests for resources and reagents should be directed to and will be fulfilled by the Lead Contact: Ramnik J. Xavier (xavier@molbio.mgh.harvard.edu).

This study did not generate new unique reagents.

METHOD DETAILS

Mice

BALB/cJ mice (Jax 000651) were obtained from the Jackson Laboratory. *Calca*$^{\Delta exon5}$ mice (B6.129S6-Calca < tm1Hku >) were kindly provided by Dr. Vijay K. Kuchroo (Brigham and Women's Hospital, Boston, Massachusetts, USA). Mice were housed in specific pathogen-free conditions and were used and maintained in accordance with the Institutional Animal Care and Use Committee (IACUC) protocol # 0055-05-15 (Broad Institute) and #18-001-XHP (Westlake University).

To induce allergic reaction to OVA, 6 to 7 weeks old mice were sensitized twice, two weeks apart, with 50 μg of OVA plus 1 mg of aluminum potassium sulfate adjuvant via intraperitoneal injection. Two weeks later, mice were orally administered with 50 mg of OVA on every other day for a total of five times. 1 μg of α-CGRP peptide was administered simultaneously when indicated. Mice were deprived of food for 3–4 hours in cages with wood chip bedding for limiting antigen degradation in the stomach before each intragastric challenge.

To activate ILC2s *in vivo*, 200 ng of IL-25 was intraperitoneally injected into 6-10 weeks old mice daily for two days. 1 μg α-CGRP was injected together as noted.

Isolation of cells from Peyer's patches (PPs)

Peyer's patches (PPs) were carefully dissected from the small intestine under a stereo microscope using a fine scissor, pierced once with a fine forcep. Tissues were digested in freshly made digestion buffer (RPMI-1640 containing 100 μg/ml Liberase TM and 50 μg/ml DNase I at 37°C on a roto-mixer. After 15 min, tissues were very gently mixed using a 1 mL pipette. The supernatant was collected and added to ice-cold MACS buffer (pH 7.4; PBS plus 2% FCS and 2mM EDTA). Pre-warmed (37°C) fresh digestion buffer was added to the remaining tissues. After rotation at 37°C for 15 min, the mixture was vigorously mixed using a 1ml pipette for 1 min. Supernatants from the two steps were combined and passed through 70 μm filters and stained for FACS (below).

Isolation of cells from the lamina propria (LP)

The small intestines were opened longitudinally and washed in ice-cold PBS. For scRNA-seq, roughly 0.5 cm of fragments from each of the distal, middle and proximal regions without visible PPs were collected. Epithelial cells were dissociated by tissue rotation in

pre-warmed (37°C) PBS containing 10 mM EDTA at 37°C for 15 min, followed by additional incubation on ice for 15 min. Tissues were then shaken vigorously. After washing twice with PBS containing 2% FCS, tissues were digested in pre-warned (37°C) digestion buffer at 37°C on a roto-mixer for 25 min. The supernatants were then passed through 70 μm filters and stained for FACS.

For experiments other than scRNA-seq, the entire small intestine was cut into 1 cm pieces after eliminating PPs. Epithelial cells dissociation was performed by stirring tissues in flasks containing PBS and 10 mM EDTA on a magnetic stirrer at 37°C two times for 15 min. After vortex, the tissue was stirred in pre-warmed (37°C) digestion buffer for 25 min at 37°C. The supernatant was passed through 100 μm filter. Leukocytes were further enriched by a 40%/70% Percoll gradient centrifugation before flow staining.

Flow cytometry and cell sorting

Cells were washed and suspended in MACS buffer (pH 7.4; PBS plus 2% FCS and 2 mM EDTA). Nonspecific antibody binding was blocked with CD16/CD32 (2.4G2) antibody for 15 min on ice. Cells were then stained with antibody cocktails for 30 min at 4°C. Lineage-positive cells were excluded for analyzing ILCs by staining for CD3ε (145-2C11), CD5 (53-7.3), CD19 (6D5), CD11b (M1/70), CD8 (53-6.7), CD11c (N418), Gr-1 (RB6-8C5), TCRγδ (eBioGL3 (GL-3, GL3)) and TCRβ (H57-597). To analyze mast cells, lineage-positive cells were excluded by staining for CD3ε, CD5, CD19, CD11c and SiglecF (E50-2440). For surface staining, antibodies for KLRG1 (2F1), CD45 (30-F11), CD127 (A7R34), CCR6 (29-2L17), NKp46 (29A1.4), CD90.2 (53-2.1), FcεRI (Mar-1), IgD (11-26c.2a) and ST2 (DJ8) were used. For intracellular staining, cells were fixed and permeabilized using the Foxp3 transcription factor staining buffer set, followed by staining with anti-GATA-3 (TWAJ) or anti-RORγt (B2D) antibodies. Dead cells were excluded with 7-AAD or Fixable Viability Dye eFluor 780. Flow cytometry was performed on Cytoflex (Beckman Coulter) and analyzed with FlowJo software. Sorting was performed with the SH800S Cell Sorter (Sony Biotechnology).

Droplet-based scRNA-seq

Single cells were captured via the GemCode Single Cell Platform using the GemCode Gel Bead, Chip and Library Kits (10X Genomics), according to the manufacturer's protocol. Briefly, flow-sorted cells were suspended in PBS containing 0.4% BSA, and loaded at 7,000 cells per channel. The cells were then partitioned into GemCode instrument, where individual cells were lysed and mixed with beads carrying unique barcodes in individual oil droplets. The products were subjected to reverse transcription, emulsion breaking, cDNA amplification, shearing, 5′ adaptor and sample index attachment. Libraries were sequenced on a HiSeq 2500 (Illumina).

Quantitative real-time PCR

RNA was isolated from 10,000 cells per sample using PicoPure RNA Isolation Kit, according to the manufacturer's protocol and reverse transcribed to cDNA with iScript cDNA Synthesis Kit. Gene expression was analyzed by quantitative real-time PCR on a ViiA7 System (Thermo Fisher Scientific) using iTaq Universal SYBR® Green Supermix with the primers listed in the Key Resources Table. Expression values were calculated relative to *Gapdh* detected in the same sample by qPCR.

ILC2 culture

Sort-purified intestinal KLRG1$^+$ ILC2s were incubated in complete RPMI medium (10% FCS, 10mM HEPES, 1mM sodium pyruvate, 10% FBS, 80 μm 2-mercaptoethanol, 2mM glutamine, 100U/ml penicillin, 100 μg/ml streptomycin), supplemented with 100 ng/ml IL-2 and 100 ng/ml IL-7 in 96-well round bottom plate at 37°C and 5% CO_2. If indicated, the culture was supplemented with 100 ng/ml IL-25. For the *in vitro* proliferation assay, cells from different mice were pooled and labeled with CellTrace Violet, and then cultured at 1,000-1,500 cells per well with 10 μg/ml α-CGRP for 60 hours. When indicated, 10 μM forskolin in DMSO was supplied and cells were cultured for 40 hours, or 1 μM SQ 22, 536 was added to cells for 1 hour before adding IL-25 for another 40 hours. For bulk RNA-seq, cells from individual mice were stimulated at 200 cells per well with 0.4 μg/ml α-CGRP for 3 hours. For bulk ATAC-seq, cells were stimulated with 0.4 μg/ml α-CGRP for 2 hours.

For assays that require large numbers of cells, intestinal ILC2s sorted from each of two mice were cultured in each well of 96-well plates with complete RPMI medium supplemented with 100 ng/ml IL-2 and 100 ng/ml IL-7 for 2 weeks. The cells were washed and rested in fresh cRPMI for 3 hours before adding stimuli.

To determine intracellular concentration of cAMP, 100,000 cells were stimulated with 100 ng/ml IL-25 or vehicle for 30 minutes and lysed with 50 μL lysis buffer (20mM Tris-HCl (pH 7.5), 100mM NaCl, 1mM Na2EDTA, 1mM EGTA, 0.8% Triton, 2mM sodium pyrophosphate, 1mM β-glycerophosphate, 1mM Na3VO4 and 1 μg/ml leupeptin). The concentrations of cAMP were determined via a chemiluminescent assay kit according to the manufacturer's protocol (Cell Signaling Technology).

To measure intracellular concentration of cytokines, 50,000 cells were stimulated with 10 ng/ml IL-25 for 8 hours before adding protein transport inhibitor cocktail for another 4 hours. The cells were then fixed and analyzed according to the intracellular flow staining protocol above.

Immunofluorescence staining and imaging

The small intestines were fixed in 2% PFA, embedded in O.C.T. Compound and sliced into 10 μm by frozen section. The slides were blocked with 0.1% Triton X-100, 2% FCS and donkey serum. The staining reagents incudes Alexa Fluor 594 anti-IgD (11-26.2a), Alexa Fluor 647 anti-CD138 (281-2), eFluor 450 anti EPCAM (G8.8), Alexa Fluor 594 anti-CD3ε (17A2), Alexa Fluor 488 anti-Podoplanin (eBio8.1.1 (8.1.1)), rat anti-CCL21/6 (59106), goat anti-IL-33 (polyclonal), hamster anti-KLRG1 (2F1), rat anti-CGRP (polyclonal), goat anti-ChAT (polyclonal), rabbit anti-DCAMKL1 (polyclonal), Alexa Fluor 647-donkey anti-goat IgG, Alexa Fluor 647 donkey

anti-goat IgG, Cy3 donkey anti-rat IgG, Alexa Fluor 488 goat anti-syrian hamster IgG (H+L), Alexa Fluor 647 goat anti-rabbit IgG (H+L) and DAPI. Slides were mounted with the ProlongGold Antifade reagent and examined with a ZEISS LSM 710 upright microscope using × 10, × 20 air or × 60 oil immersion lens. The images were analyzed with ImageJ.

Bulk RNA-seq

200 ILC2s from each condition were lysed in 10 ul TCL buffer plus 0.5% 2-Mercaptoethanol. Libraries were processed with SMART-Seq2 (Picelli et al., 2013) with at least three replicates per condition, and paired-end sequenced (38 bp × 2) with a 75 cycle Nextseq 500 high output V2 kit.

Reads were aligned to the mouse reference genome (NCBI 38, mm10) using STAR v2.6.0c (Dobin et al., 2013) with parameter '–twopassMode Basic' and otherwise default parameters, the number of reads mapped to each gene were calculated using featureCounts (Liao et al., 2014) from the Subread package, v1.6.2, and expression abundances were estimated using RSEM v1.2.8 (Li and Dewey, 2011). Differential gene expression analysis was performed on the count matrices output from featureCounts with edgeR R package v3.5.2 (Robinson et al., 2010) with default parameters.

Overall Expression analysis

We computed the Overall Expression (OE) of gene signatures in each sample as previously described (Jerby-Arnon et al., 2018). The procedure is based on the notion that the measured expression of a specific gene is correlated with its true expression (signal), but also contains a technical (noise) component. The latter may be due to various stochastic processes in the capture and amplification of the gene's transcripts, sample quality, as well as variation in sequencing depth. The OE of a gene signature is computed in a way that accounts for the variation in the signal-to-noise ratio across genes and cells.

Given a gene signature and a gene expression matrix E, where $E_{i,j} = \log2(TPM_{i,j}+1)$ and $TPM_{i,j}$ denotes the transcripts per million value of gene i in sample j, we first binned the genes into 50 expression bins according to their average expression across the samples. The average expression of a gene across a set of N samples was defined as: $\mathbb{E}_j[E_{ij}] = \sum_j(E_{ij}/N)$. Given a gene signature S that consists of K genes, with k_b genes in bin b, we sample 100 random S-compatible signatures for normalization. A random signature is S-compatible with a signature S if it consists of overall K genes, such that in each bin b it has exactly k_b genes. The OE of signature S in cell or sample j is then defined as:

$$OE_j = \frac{\sum_{i\in S} C_{ij}}{\mathbb{E}_{\tilde{S}}\left[\sum_{i\in \tilde{S}} C_{ij}\right]}$$

Where $\tilde{S}$ is a random S-compatible signature, and C_{ij} is the centered expression of gene i in sample j, defined as $C_{ij} = E_{ij} - \mathbb{E}[E_{ij}]$. Because the computation is based on the centered gene expression matrix C, genes that generally have a higher expression compared to other genes will not skew or dominate the signal. We used the software in https://github.com/livnatje/ImmuneResistance to compute the OE of gene signatures of interest.

Bulk ATAC-seq

ATAC-seq experiment was performed using a published protocol (Buenrostro et al., 2013) with minor modifications. Briefly, 2, 000 cells in 5 μL PBS, 17.3 μL H_2O and 25 μL of transposition buffer (66 mM Tris-acetate, 132 mM K-acetate, 20 mM Mg-acetate, 32% DMF, and 0.2% NP-40) were mixed and incubated at room temperature for 10 min. After adding 2.5 μL of Tn5 transposase to the reaction, the transposition was carried out at 37°C for 30 min with gentle shaking at 300 rpm and then purified with Zymo DNA Clean and Concentrator (Zymo Research). The library was amplified for 11 cycles, purified with Zymo DNA clean (Zymo Research), and sequenced on an Illumina Next-seq platform using 75 cycle Nextseq 500 high output V2 kit (Read 1: 38 cycles, Index 1: 8 cycles, Index 2: 8 cycles, Read 2: 38 cycles).

The reads were trimmed and aligned to the mouse reference genome (mm9) with Bowtie2 aligner (Langmead and Salzberg, 2012) using the option -X2000. Then, we discarded reads with alignment quality < Q30, improperly paired, mapped to the unmapped contigs, chrY, and mitochondria. Duplicates were removed using Picard tools (function MarkDuplicates, http://broadinstitute.github.io/picard/). MACSv2 peak caller (Zhang et al., 2008) (version: 2.1.1) was used to call accessible regions of open chromatin regions (ATAC-Seq peaks) with the following parameters (–nomodel –nolambda –keep-dup -call-summits). Peaks overlapping with ENCODE blacklisted regions were filtered out using BEDtools (function itersectBed). Peak summits were extended by ± 250 bp, and fragment counts in peaks were calculated using chromVAR (Schep et al., 2017) (version: 1.1.1). Peaks were allocated to genes using GREAT (McLean et al., 2010) (version: 3.0.0) with ''basal plus extension'' association rule with default parameters. Functional enrichment analysis was performed using GREAT (version: 3.0.0).

scRNA-seq data QC and pre-processing

Reads demultiplexing, alignment to the mm10 genome, unique molecular identifier (UMI) counting and collapsing were performed using Cell Ranger v2.1.1 (10x Genomics) to generate cell by gene UMI count matrices. After removing cells with less than 500 UMIs and high mitochondrial RNA UMIs (more than four times of the median number of mitochondrial UMIs across cells), we

obtained 36,797 cells from PP regions (15,939 cells from OVA-allergic mice and 20,858 cells from controls), and 21,270 cells from LP (11,405 cells from OVA-allergic mice and 9,865 cells from controls). 19,221 genes were retained after filtering genes expressed in less than five cells.

We expected batch effects in the data, because libraries were prepared and sequenced at different times, and because we used two sorting strategies to remove either IgD^+ Naive B cells or $CD19^+CD3^+$ cells. Moreover, the number of recovered cells varied across experiments; for example, we recovered 10,567, 6,439, 5,016, 4,571, and 10,204 cells from each of the five experiments for cells from PPs. We explored several possibilities to address these confounders. Two recent methods have been developed to align scRNA-seq data from different batches (Butler et al., 2018; Haghverdi et al., 2018). However, a cell type must be shared by all datasets for Seurat's CCA approach to correctly align cells (Butler et al., 2018), which is not appropriate for our case. mnnCorrect (Haghverdi et al., 2018) can merge datasets with private (distinct) cell types, but in our datasets where there were dozens of cell types, mnnCorrect successfully merged only some of these clusters, and failed to align cells from other clusters.

Principal Component Analysis (PCA) is typically used to extract a small number of features (principal components (PCs)) from a normalized gene-cell count matrix. These feature vectors were used for clustering analysis or as inputs for visualization. Unfortunately, in the presence of batch effects, some of the top features typically captured batch effects (Chen et al., 2011). Therefore, batch effects could not be removed by discarding the features with small eigenvalues in PCA.

To help address these batch effects, we took an alternative approach, where we projected the scRNA-seq data to a reference dataset consisting of microarray measurements of immune cells from 276 samples (Heng et al., 2008). Specifically, we first did PCA on the microarray data and extracted the first 101 eigenvectors. We discarded the first eigenvector as the corresponding first PC was correlated with batch information in the microarray data. We next projected the scRNA-seq data to the 100-dimensional space spanned by the eigenvectors (PCs 2-101) from the microarray data. The coordinates of cells in the 100-dimensional space were used for clustering and as inputs of scvis. We named our batch-correction method reference-projection.

Benchmarking different batch correction approaches

We benchmarked reference-projection to three other recent proposed batch-correlation methods: LIGER (Welch et al., 2019), Harmony (Korsunsky et al., 2018), and scVI (Lopez et al., 2018). For LIGER, we followed the standard pipeline and choose 20 factors. For Harmony, we used a theta of four and 50 principal components. For scVI, we used ten dimensional latent variables and three hidden layers (each with 512 units) for both the encoders and decoders. Phenograph (Levine et al., 2015) clustering the batch-corrected data from each method produced 44, 34, and 28 clusters, respectively. We next quantitively and qualitatively compared the results produced by each method.

We assessed the performance of the methods by two criteria. **First**, for the data from a specific batch, we asked if the partitions from clustering this dataset in isolation and from clustering the merged dataset after batch-correction were similar, with similarity measured by normalized mutual information (NMI), with the maximum NMI = 1 if the two partitions are identical, and NMI = 0 if the two partitions were independent. **Second**, we asked if cells in each cluster were well-mixed across different datasets and batches. To measure the mixture, for each dataset from a batch, we first computed the fractions of cells in each cluster, and then computed the Pearson correlation coefficient between the cell fraction vectors from each dataset (batch). Here, we interpreted the results in the context of our experimental design, where the gating strategies and tissue sources (LP or PP) were chosen to alter cell compositions of obtained cells between some batches. Specifically, cells from experiment 1-3 were obtained using the same gating strategy (removing naive B cells) and cells from experiment 4-5 were obtained from removing $CD19^+$ B cells and $CD3^+$ T cells. Experiment 1-5 cells were from Payer's patches and experiment 6-7 cells were from lamina propria.

Based on the first clustering concordance measure, our reference-projection method consistently outperformed LIGER (Figure S1D), and outperformed Harmony and scVI for the first five datasets and performed slightly worse for the last two datasets. Based on the second mixing measure, the Pearson correlations between cell composition vectors from datasets of the same gating strategy were high (Figure S1E). Although the correlations between cell composition vectors from clustering the merged datasets using Harmony (Figure S1E) were generally the highest, these included those between datasets of different gating strategies, suggesting higher background noise in the Harmony results. The other three methods performed comparably on data from experiments 6 and 7 (Pearson correlation coefficients of 0.93), LIGER performed slightly worse on experiment 4 and 5 (Pearson correlation coefficients of 0.94), and for experiments 1-3, LIGER performs the best, followed by reference-projection, and scVI performed the worst.

Finally, we visually inspected the clustering results on the batch-corrected datasets. LIGER and Harmony tends to split big clusters, e.g., naive T cells (cluster 1 in Figure 1B) and naive B cells (cluster 2 in Figure 1B), while merging some small clusters (e.g., gamma-delta T cells, cluster 17 and 38 in Figure 1B) to other clusters. The results of scVI and reference-projection are more consistent with each other. We also compared the NMIs between the partitions from clustering datasets that were batch-corrected in different ways. scVI and reference-projection had the highest concordance (NMI = 0.8). However, as the clustering algorithm divided the scVI results into only 28 clusters, some similar clusters such as the two germinal cell B cells (cluster 9 and 10 in Figure 1B) were in the cell cluster, similarly for other cells such as ILC1 and NK cells (cluster 11 and 8 in Figure 1B).

In summary, compared to other state-of-the-art batch-correction methods, the reference-projection method retained the structures in individual datasets (with high concordance between the partitions from clustering the merged dataset and the partitions from clustering individual datasets independently) and ensured that cells from different datasets were well mixed (with high Pearson correlations). It helped us identify different types of cells from mouse small intestines for down-stream analyses.

scRNA-seq clustering of PP cells

We used the Louvain community detection algorithm (Blondel et al., 2008; Levine et al., 2015) to cluster cells from Peyer's patch regions. As the Louvain clustering algorithm tends to miss some small clusters, we used densityCut (Ding et al., 2016) to find the likely cluster centers. For each center, we changed the edge weights (w′) connecting the cluster center to its neighbors to (w′) = 2*kw*, where *k* is the number of nearest neighbors in the *k*-nearest neighbor (*k*-NN) graph, and *w* is the original edge weight of an edge. Louvain clustering on this edge re-weighed graph produced 46 clusters.

Next, we assessed the robustness of the cell to cluster assignment. For each cluster and each batch, we computed the 'bulk' gene expression profile of the cells from a given batch in the cluster. The 'bulk' gene expression profile for a set of cells is computed by first taking the sum of the gene expression vectors from these cells, where the gene expression vector of a cell was the raw UMI count vector, one element for a gene. The dimensionality of a gene expression vector was the number of genes. To make the bulk gene expression vectors from different sets of cells comparable, a bulk gene expression vector was normalized by dividing the total number of UMIs from all the cells used in computing that bulk gene expression vector, and further multiplying by 10^4 and finally taking the log transform (adding one before the log transformation to make all the elements of the bulk vector positive). Then, for each cell, we computed its Pearson correlation coefficient with the "bulk" profile for each cluster. We denote the maximum correlation between a cell *x* and the bulk profiles of cluster *i* (from different batches) as c_i. If cell *x* is originally assigned to cluster *j*, and $c_j < 0.9c_k$, then we reassign cell *x* to cluster *k*. Only ~0.26% (97 of 36,797) cells were re-assigned to clusters different from their original assignment. We also tested whether two clusters should be merged, if there are no more than 10 significantly differentially expressed genes between them (with differential expression estimated with the Wilcoxon rank-sum test in the package Seurat (Butler et al., 2018)). However, none of the 46 clusters required merging by this criterion.

Clustering cross-validation of PP cells

We performed a 10-fold cross validation analysis on the PP data to evaluate the quality of the clustering. We partitioned the PP data into ten approximately equal size sets, and trained a *k*-nearest neighbor (*k*-NN) classifier (we used a small $k = 11$ as some clusters are small, e.g., 17 cells in cluster 46) on nine folds of data, leaving one-fold of data for testing. We repeated this training and testing scheme ten times such that all the data points were used for testing only once.

The *k*-NN classifiers had a high overall accuracy of 97.2%. Classification accuracy varied for cells from different clusters, with those from cluster 39 having the lowest accuracy of 65.6%. Cluster 39 consisted of a mixture of low-quality plasma B cells and cell doublets (macrophage and epithelial cell doublets). A subgroup of cells expressed plasma B cell marker genes, such as *Jchain* and *Mzb1*, but had a relatively small number of UMIs per cell compared to the cells from the plasma cell Cluster 20 (Figure S1F). Some of these low-quality plasma B cells also had high mitochondrial UMI ratios. Another subset of cells in Cluster 39 expressed both epithelial cell markers (e.g., *Epcam* and *Krt8*) and macrophage marker genes (e.g., Lyz1 and Lyz2). These cells had a very large number of UMIs per cell (Figure S1F) and likely represented potential macrophage and epithelial cell doublets. Notably, although the number of cells in each cluster was extremely unbalanced (e.g., 6,948 cells in cluster 1 but only 17 cells in cluster 46), the classification accuracies were largely uncorrelated with the number of cells in each cluster.

Cluster annotation and filtering of PP cells

We next used MAST (Finak et al., 2015) to identify significantly upregulated marker genes for each of the 46 clusters, accounting for batch (experimental dates) and the scaled number of detected genes in each cell as covariants (Soneson and Robinson, 2018). Based on known function of the marker genes, we annotated 6 major cell lineages and groups: T cells, B cells, dendritic cells, ILCs, myeloid cells, and stromal cells.

We conservatively excluded from further analyses the smallest clusters (< 0.05% of all cells) and several ambiguous clusters that we could not confidently assign with cell identities. We note that the small clusters may be biologically valid, but the small number of cells limits our ability to further study them here. For example, the top markers of cluster 45 (18 cells) included *Dntt*, *Rag1, Chrna9*, *Tctex1d1*, *Arpp21*, which are highly expressed in progenitors of T cells at the double-positive stage in Immgen (Heng et al., 2008; Painter et al., 2011). Cluster 46 (17 cells) may consist of lymph node lymphatic endothelial cells, as they expressed their known marker genes such as *Lyve1*, *Prox1*, and *Cp*. Experimental validations are required for confidently including them in the downstream analyses. Cells in Cluster 34 (100 cells) from PP, expressed both pDC and myeloid gene markers. Only two marker genes (*Gtf2a1* and *2310001H17Rik*) overlapped between Cluster 34, and either of its adjacent clusters in scvis, clusters 6 and 22 (Figure 1B). *Gtf2a1* was expressed lowly in about 25% of the cluster 34 cells and *2310001H17Rik* was expressed in several other cell types, such as T cells and neutrophils. We annotated cluster 34 as 'Unresolved'. Cluster 18 and cluster 37 were also annotated as 'Unresolved' based on similar analysis. Cluster 40 cells expressed macrophages marker gene like *Lyz2*. Compared to the macrophage cluster (cluster 22), cluster 40 cells expressed higher amounts of *C1qa, C1qb*, and *C1qc*. However, Cluster 40 cells had less UMIs per cells (Figure S1F) than Cluster 22 cells. We also labeled Cluster 40 as 'Unresolved'.

We further removed clusters enriched for doublets. To this end, we analyzed PP cells with Scrublet (Wolock et al., 2019), identifying clusters 29, 41, and 43 cells with high doublet scores, together accounting for 0.63% (232 of 36,797) of the PP cells. Cluster 42 cells also had high doublet scores, albeit lower than these other three clusters, and may be further potential doublets.

Clustering LP cells

We used the 35,691 PP cells that were both confidently assigned to clusters in the cross-validation above and had a *k*-NN probability greater than 0.5, to train a *k*-NN classifier ($k = 11$), and used it to classify the 21,270 LP cells. The vast majority of LP cells (97.4%, 20,724 / 21,270) were assigned to 42 of the 46 clusters with *k*-NN probability greater than 0.5. We refined the clustering as done for the Peyer's patch data but only for the cells with *k*-NN probabilities less than 0.5. This reassigned only 0.12% (26 / 21,270) cells. 34 of the 42 clusters had > 15 cells. To find potential LP-specific clusters (cell types that were only observed in LP), we concatenated the data from PPs and LP and then clustered the merged data. Of the clusters enriched in cells from LP (more than three times the number of cells from LP than PPs), two consisted of mast cells and three of plasma B cells. One of these clusters had cells with a low number of UMIs per cell without apparent marker genes. One LP-enriched cluster consisted of fibroblasts that expressed marker genes, such as *Col15a1*, *Ecm1*, and *Col6a5*.

Ten-fold cross validation of the 21,223 LP cells in 34 clusters with > 15 cells showed 94.59% accuracy for all cells. Cells from three small clusters 5, 19, and 42 (32, 41, and 19 cells, respectively) had relatively low cross-validation accuracies of 0.41, 0.56, and 0.53, respectively. Overall, ~93.70% (19,886 / 21,223) were assigned robustly (correctly classified in cross-validation and with *k*-NN probabilities greater than 0.5).

Cellular composition changes

As different gating strategies (IgD^{low} or $CD3^{-}CD19^{-}$) directly influenced the frequencies of T and B cells, which subsequently affected the proportions of all other cell types, we separately quantified cell compositions in B cells, T cells, and other non-TB cell types. In addition, for analyzing changes in the composition of B cell subsets, we did not include cells from the experiments with $CD3^{-}CD19^{-}$ sorting.

Moreover, because of random sampling and unevenness of recovery of cells across mice, considering the number of cells (and not only fractions) is a critical part of the testing framework. The accuracy of estimating a cell type's proportion in the population increases as we have more cells. For mice with relatively few cells recovered overall, the estimates could be poor, and we want our test to be aware of these overall lower counts. Statistical tests based on ratios alone (proportions), discard the information about the total number of cells used in calculating the ratios and as a result treat the ratio from each mouse equally, irrespective of the underlying cell numbers. We thus used a framework based on the negative binomial regression model and the Wald test.

We used the negative binomial regression model to assess cell composition changes between PPs and LP using cells in homeostasis (Figure 1C). We used spatial information (PP or LP) as a covariate and the total number of analyzed cells from each mouse as an offset variable. The P value for the significance of location information (LP) on a cell type was also assessed using the Wald test on the regression coefficient.

We performed similar analyses to assess cell composition changes between PPs and LP using all data, with the negative binomial regression model with treatment (OVA or PBS) and location (PP or LP) as covariates (Figure S1M). The total number of analyzed cells (e.g., the total number of B cells when quantifying B cells variations) from each mouse was used as an offset variable. The P value for the significance of location (LP) on a cell type was assessed using the Wald test on the regression coefficient. Generally, the results for differences between LP and PP were consistent with those obtained for homeostasis data, with two minor exceptions: cluster 6 (pDCs) was not significantly different between regions when considering both OVA and PBS treated mice, but cluster 24 (DC ($CD103^{-}$ C1)) was significant.

To assess differences in composition due to treatment (Figure 2B, top), we used the same framework with treatment (OVA or PBS) and location information (PP or LP) as covariates. The total number of analyzed cells (e.g., the total number of T cells when quantifying T cells variations) from each mouse was used as an offset variable. The P value for the significance of treatment (OVA) on a cell type was assessed using the Wald test on the regression coefficient.

Finally, we also tested cell composition changes between PBS and OVA treated mice for each of the PP and LP datasets separately, using the negative binomial regression model with only treatment as the covariate (Figure 2B, middle and bottom).

Cell sampling frequencies

To estimate the number of required cells such that we have the power to recover rare cell types, we used the online tool: http://satijalab.org/howmanycells. The method assumes that the probability of observing at least N cells of a cell type in a sample of size K can be modeled by the cumulative distribution function of a negative binomial NBcdf(K; N, p), where p is the relative abundance of this cell type.

Topic modeling

In the topic modeling analysis, one gene can belong to multiple topics (programs), and its relative relevance in the topic is reflected by a weight. A cell is represented as a weighted mixture of topics, where the weights reflect the importance of the corresponding topic (program) in the cell. A single gene from a topic may not be sufficient to highlight the identified cellular program nor may its entire expression signal be relevant to the program. Thus, unlike the simple averaging or aggregation of expression for genes in an expression signature, in topic models we learn how different genes contribute differently to the topic, how a topic can contribute to cells to different extents, and (in contrast to cell type specific markers), how a topic can be relevant across cells of different types. As a result, topic modeling is more nuanced in how it handles both cells and genes.

To help guide LDA to find the informative topics, we learned multiple topic models for each subgroup of cells separately. (We had found that topic modeling of all subsets together mostly identifies cell type programs; data not shown.) Specifically, we used the FitGoM() function from the CountClust R package (Dey et al., 2017) to fit LDA topic models to the UMI counts (Bielecki et al., 2018) for cells belonging to each major identified cell type from the LP and PP regions. This resulted in 12 models, two for each of the following cell types: T cells (583 LP cells, 12,187 PP cells), DC cells (3,738 LP cells, 3,530 PP cells), B cells (5,648 LP cells, 7,376 cells), ILC cells (5,484 LP cells, 9,396 PP cells), myeloid cells (1,825 LP cells, 579 PP cells), and stromal cells (90 LP cells, 443 PP cells). Genes starting with 'Rpl' or 'Rps' were removed from the counts matrix prior to fitting the topic models, leaving a total of 19,108 genes included in each count matrix. The number of topics to fit and the tolerance value are required to run FitGoM() function. Thus, for each cell type and region, we fit a range of K and then used compGoM() to compute the Bayesian Information Criterion (BIC) the estimated likelihood, from which we calculated the Akaike Information Criterion (AIC). Our final choice of K value was primarily guided by the BIC curve; we aimed to choose a K at which the BIC was minimal, or decreasing less quickly. We set the tolerance value to 0.1. The top genes to highlight for each topic were selected using the ExtractTopFeatures() function.

Statistical analysis

Mice from which we failed to isolate a sufficient number of live cells for downstream analysis were excluded. Prism 7 (GraphPad Software) was used to perform two-tailed t test and Fisher's exact test as indicated (except for RNA-seq data for which we use R for statistical analysis). P values from multiple comparisons were FDR-adjusted in R.

DATA AND CODE AVAILABILITY

The scRNA-seq data and bulk RNA-Seq data generated during this study are available at NCBI Gene Expression Omnibus through accession number GEO: GSE124880. Processed scRNA-seq data are also available from Single Cell Portal: https://portals.broadinstitute.org/single_cell/study/fasi-immune-mouse-small-intestine

Custom code and software packages are available freely from Bitbucket: https://bitbucket.org/jerry00/mouse_small_intestine_immune_cell_atlas/src/master/

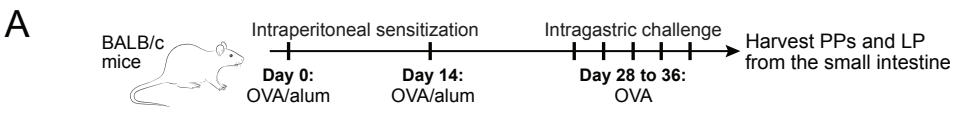
Immunity, Volume *51*

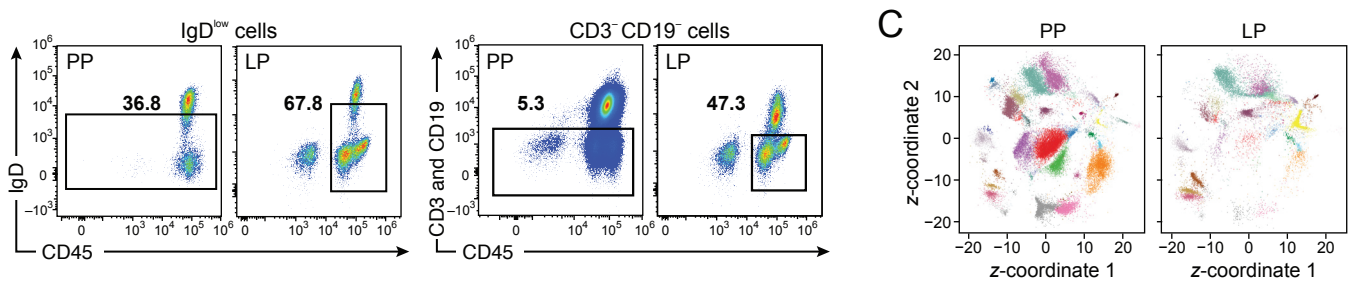
Supplemental Information

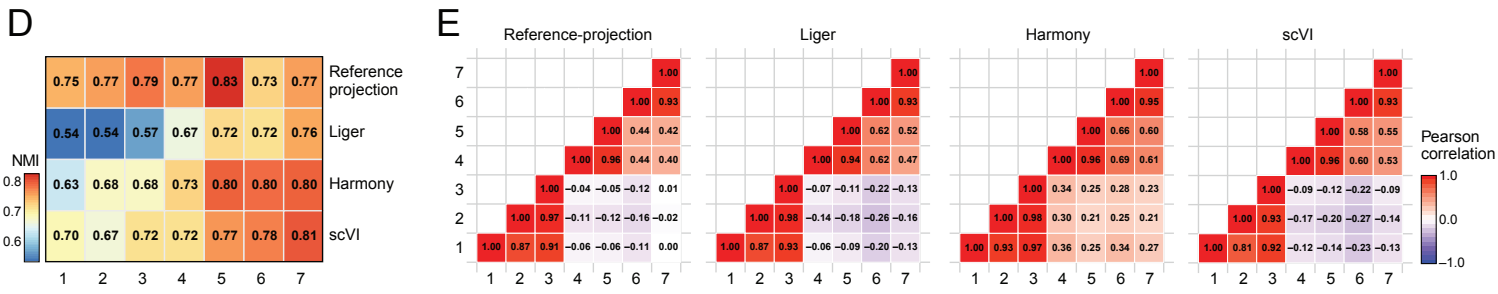
Transcriptional Atlas of Intestinal Immune Cells Reveals that Neuropeptide α-CGRP Modulates Group 2 Innate Lymphoid Cell Responses

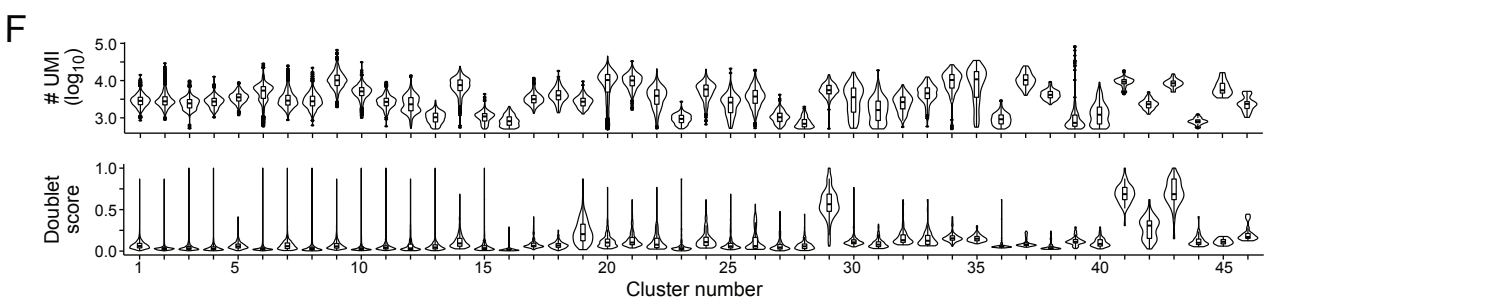
Heping Xu, Jiarui Ding, Caroline B.M. Porter, Antonia Wallrapp, Marcin Tabaka, Sai Ma, Shujie Fu, Xuanxuan Guo, Samantha J. Riesenfeld, Chienwen Su, Danielle Dionne, Lan T. Nguyen, Ariel Lefkovith, Orr Ashenberg, Patrick R. Burkett, Hai Ning Shi, Orit Rozenblatt-Rosen, Daniel B. Graham, Vijay K. Kuchroo, Aviv Regev, and Ramnik J. Xavier

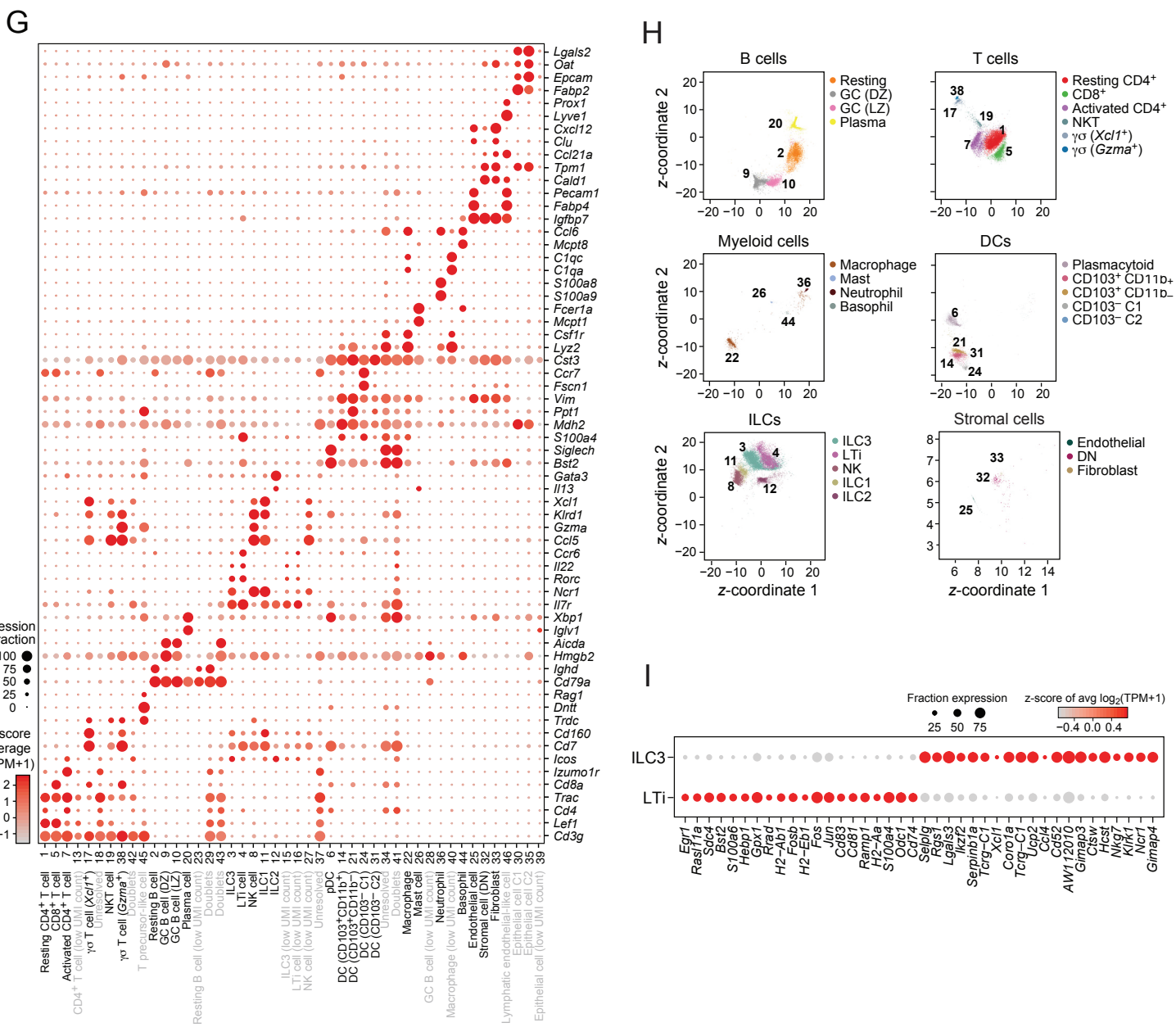
Figure S1

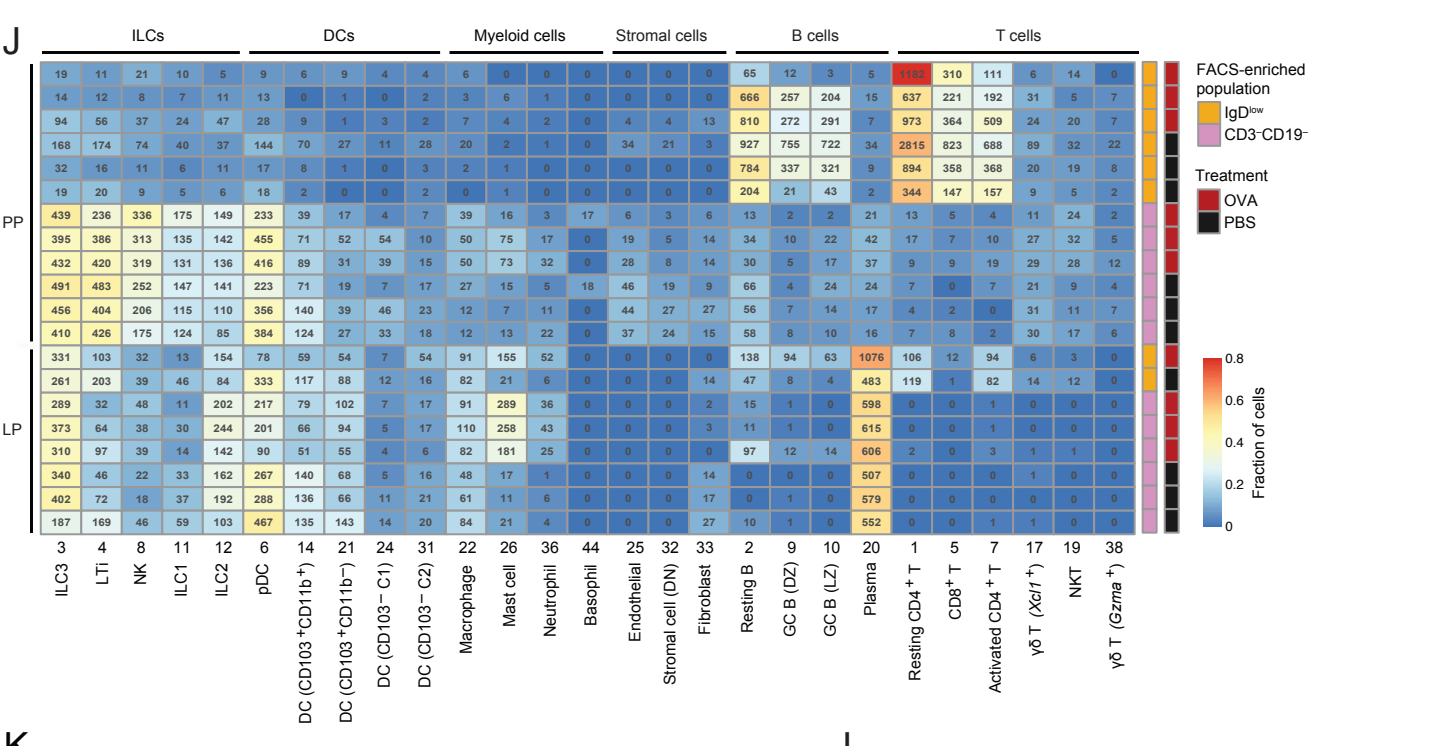

A
BALB/c mice
Intraperitoneal sensitization
Day 0: OVA/alum
Day 14: OVA/alum
Intragastric challenge
Day 28 to 36: OVA
Harvest PPs and LP from the small intestine

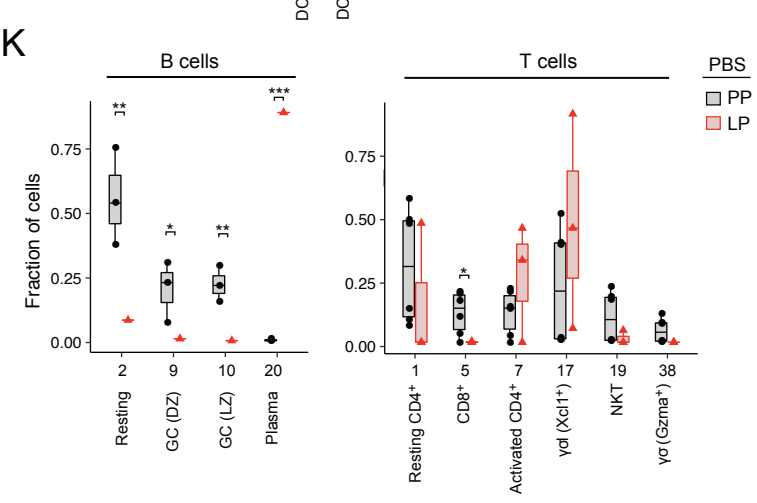

B
IgD^low cells
CD3⁻CD19⁻ cells
PP
LP
36.8
67.8
5.3
47.3
IgD
CD3 and CD19
CD45
C
PP
LP
z-coordinate 2
z-coordinate 1

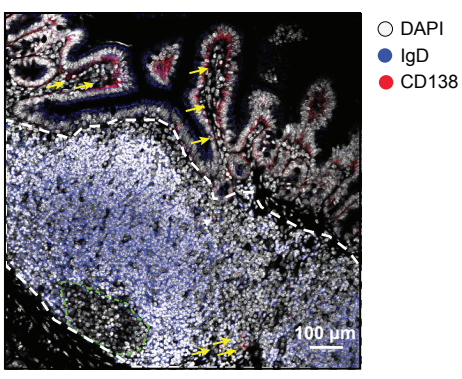

D
NMI
Reference projection
Liger
Harmony
scVI
E
Reference-projection
Liger
Harmony
scVI
Pearson correlation


F
UMI (log10)
Doublet score
Cluster number


G
H
B cells
Resting
GC (DZ)
GC (LZ)
Plasma
T cells
Resting CD4+
CD8+
Activated CD4+
NKT
γσ (Xcl1+)
γσ (Gzma+)
Myeloid cells
Macrophage
Mast
Neutrophil
Basophil
DCs
Plasmacytoid
CD103+ CD11b+
CD103+ CD11b−
CD103− C1
CD103− C2
ILCs
ILC3
LTi
NK
ILC1
ILC2
Stromal cells
Endothelial
DN
Fibroblast
Expression fraction
Z-score of average log2(TPM+1)
I
Fraction expression
z-score of avg log2(TPM+1)
ILC3
LTi


J
ILCs
DCs
Myeloid cells
Stromal cells
B cells
T cells
PP
LP
FACS-enriched population
IgD^low
CD3⁻CD19⁻
Treatment
OVA
PBS
Fraction of cells


K
B cells
T cells
PBS
PP
LP
Fraction of cells
Resting
GC (DZ)
GC (LZ)
Plasma
Resting CD4+
CD8+
Activated CD4+
γδ (Xcl1+)
NKT
γσ (Gzma+)


L
DAPI
IgD
CD138
100 μm

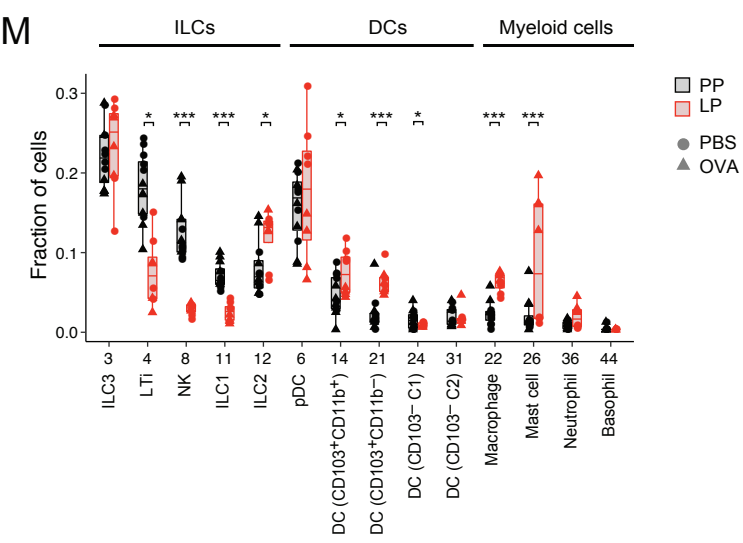

M
ILCs
DCs
Myeloid cells
PP
LP
PBS
OVA
Fraction of cells

Figure S1. FACS, single-cell expression and IF staining analysis of intestinal immune cells, related to Figure 1

(**A**) Experimental overview.

(**B**) Depletion of common cell types by FACS. Shown are representative FACS plots for sorting lgD^{low} cells (left) or $CD3^{-}CD19^{-}$ cells (right) from PP and LP regions. $CD45^{-}$ cells were not included in LP.

(**C**) An LP and PP cell atlas. A 2D embedding as in **Figure 1B**, but showing separately only the 36,797 cells from PP regions (left) or the 21,270 cells from LP (right).

(**D,E**) Comparison of batch correction methods. (D) Normalized mutual information (NMI, color bar) between clustering results from each dataset (columns) analyzed independently and the merged dataset generated using different batch-correction methods (rows) (**STAR Methods**). (E) Pearson correlation coefficients between the cell fraction vectors of the proportion of cells in clusters from two dataset (rows, columns, **STAR Methods**). Experiment 1-3: naive B cells were removed; Experiment 4-5: $CD19^{+}$ B cells and $CD3^{+}$ T cells were removed. The cells were collected from Peyer's patches (experiment 1–5) or lamina propria (experiment 6–7).

(**F**) Cluster quality measures. Top: distribution of number of UMIs (*y* axis, $\log_{10}$-transformed) in both LP and PP cells in each cluster from **Figure 1B** (x axis). Bottom: distribution of doublet scores (y axis, **STAR Methods**) of PP cells in each cluster from **Figure 1B** (x axis).

(**G**) Differentially expressed genes. For representative differentially expressed genes (rows) across clusters (columns), shown is the fraction of cells in the cluster that express a gene (dot size) and the z-score of the mean expression of that gene in the cluster (color; z-score of average $\log_2$(TPM+1)). The inferred identities were labeled at the bottom with those excluded from the downstream analyses are in grey.

(**H**) Clusters of specific cell types in the atlas. A 2D embedding as in **Figure 1B**, but showing separately only the cells in each cell lineage or group as labeled.

(**I**) Differentially expressed genes between ILC3 and LTi. Fraction of cells in the cluster that express a gene (dot size) and the z-score of the mean expression of that gene in those cells that express it in the cluster (color; z-score of average $\log_2$(TPM+1)).

(**J**) Number and proportion of cells detected in each mouse in the study. Fraction (color bar, out of all cells from that mouse) and number of cells from each of the 27 cell clusters (columns) in each individual mouse (rows), along with its treatment (Black/red: OVA/PBS) and enrichment strategy (purple/orange: IgD^{low}/$CD3^{-}CD19^{-}$).

(**K**) Tissue distribution of B (left) and T (right) cells between LP and PP in homeostasis. Proportion (*y* axis) of each cell type (*x* axis) in LP (red) and PP (black) regions of mice treated with PBS. Points: independent mice (n=3 for B cells, n=6 for T cells); Boxplots denote IQR as in **Figure 1C**.

(**L**) Differential distribution of plasma cells and GC B cells. Representative IF image of the small intestines of wild type mice. White dashed line: PP region; Green dashed line: GC area; arrow: $CD138^{+}$ plasma cell; scale bar, 100 μm.

(**M**) Tissue distribution of non-T and non-B immune cells in both homeostatic and inflammatory conditions. Proportion (*y* axis) of each cell type in LP (red, n=8 mice) and PP (black, n=12 mice) regions of mice treated with PBS (dots) or OVA (triangles). Points: independent mice; Boxplots: medians and interquartile ranges (IQR). Whiskers: lowest datum within 1.5 IQR of the lower quartile and the highest datum within 1.5 IQR of the upper quartile. *$p < 5\times10^{-2}$, **$p < 3\times10^{-8}$, ***$p < 3\times10^{-9}$, Wald test (K, M) for difference in cell composition accounting for cell counts (counts shown in **Figure S1J**). Data are representative of seven (B) or two (L) independent experiments, or are from seven (C, D, E, F, G, H, J, M) or three (I, K) independent experiments.

Figure S2

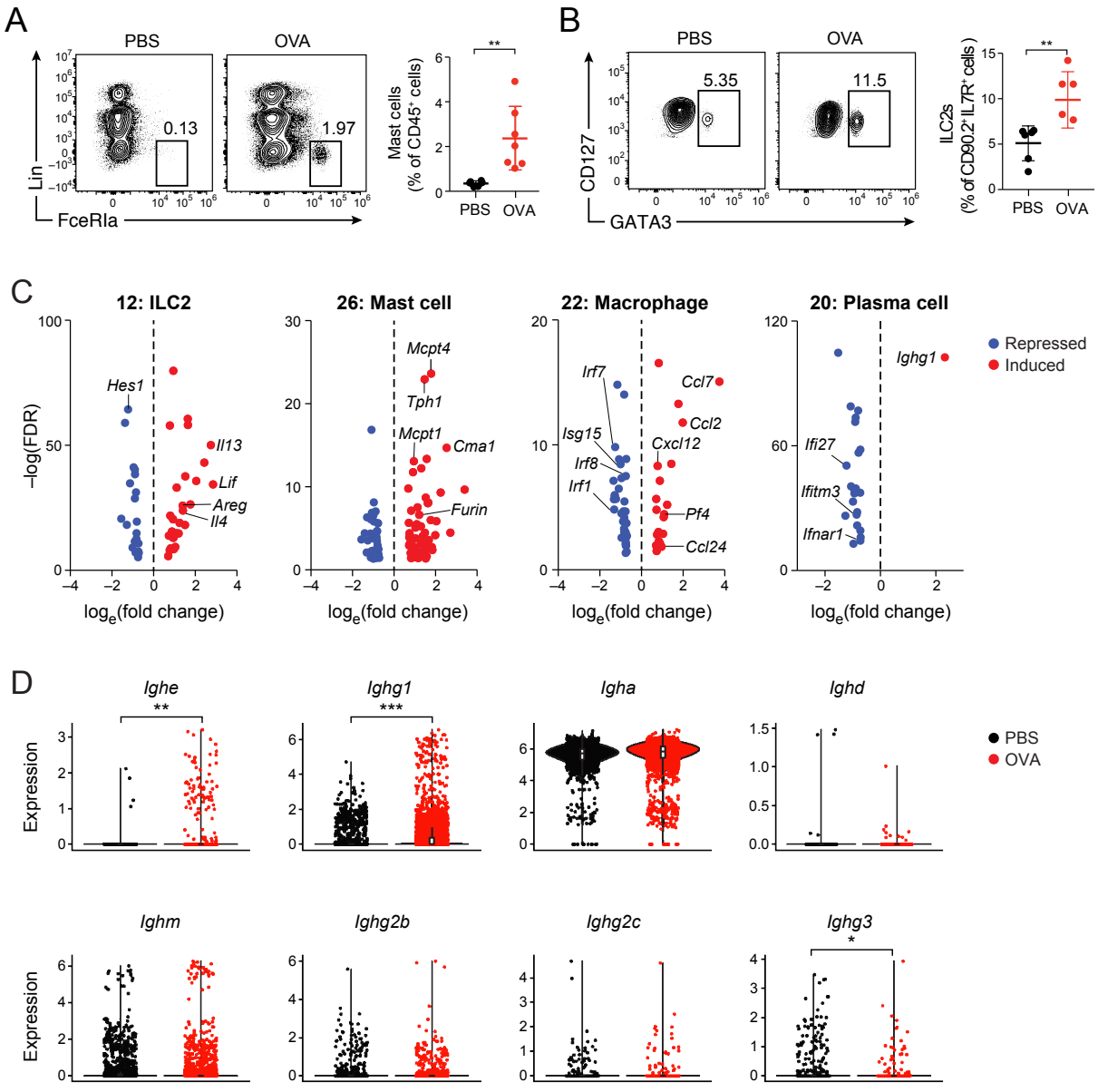

A
PBS
OVA
0.13
1.97
Lin
FceRIa
Mast cells (% of CD45+ cells)
**
PBS
OVA
B
PBS
OVA
5.35
11.5
CD127
GATA3
ILC2s (% of CD90.2+ IL7R+ cells)
**
PBS
OVA
C
12: ILC2
26: Mast cell
22: Macrophage
20: Plasma cell
–log(FDR)
Hes1
Il13
Lif
Areg
Il4
Mcpt4
Tph1
Mcpt1
Cma1
Furin
Irf7
Ccl7
Ccl2
Isg15
Cxcl12
Irf8
Irf1
Pf4
Ccl24
Ighg1
Ifi27
Ifitm3
Ifnar1
log_e(fold change)
Repressed
Induced
D
Ighe
Ighg1
Igha
Ighd
Ighm
Ighg2b
Ighg2c
Ighg3
Expression
**
***
*
PBS
OVA

Figure S2. Cell proportions in T, B, mast cells and ILC2s, and gene expression in mast cells, ILC2s, macrophages and plasma cells in OVA-induced type 2 inflammation, related to Figure 2

(**A,B**) Flow cytometry analysis of frequencies of mast cells (B) and ILC2s (C) in the LP of mice treated with PBS (black) or OVA (red). Left: representative FACS plots; Right: summary of results. Points: individual mice mean±SEM; **$p < 0.01$, *t* test.

(**C**) Differentially expressed genes in ILC2s, mast cells, macrophages and plasma cells in the LP. Shown are genes repressed (blue) or induced (red) ($|\text{fold change}| \geq 2$, $p < 0.05$, likelihood ratio test, frequency of expressing cells ≥ 25% at the up-regulation side) by OVA-induced inflammation in each labeled cell type. Dots: genes, with key ones labeled.

(**D**) Distribution of expression amounts (y axis, $\log_2(\text{TPM}+1)$) of *Igh* genes (labeled) in plasma cells in homeostatic (black) or OVA-induced inflammatory (red) conditions. *$p < 3\times10^{-5}$, **$p < 3\times10^{-13}$, ***$p < 2\times10^{-107}$, likelihood ratio test. Data are from two (A, B) or seven (C, D) independent experiments.

Figure S3

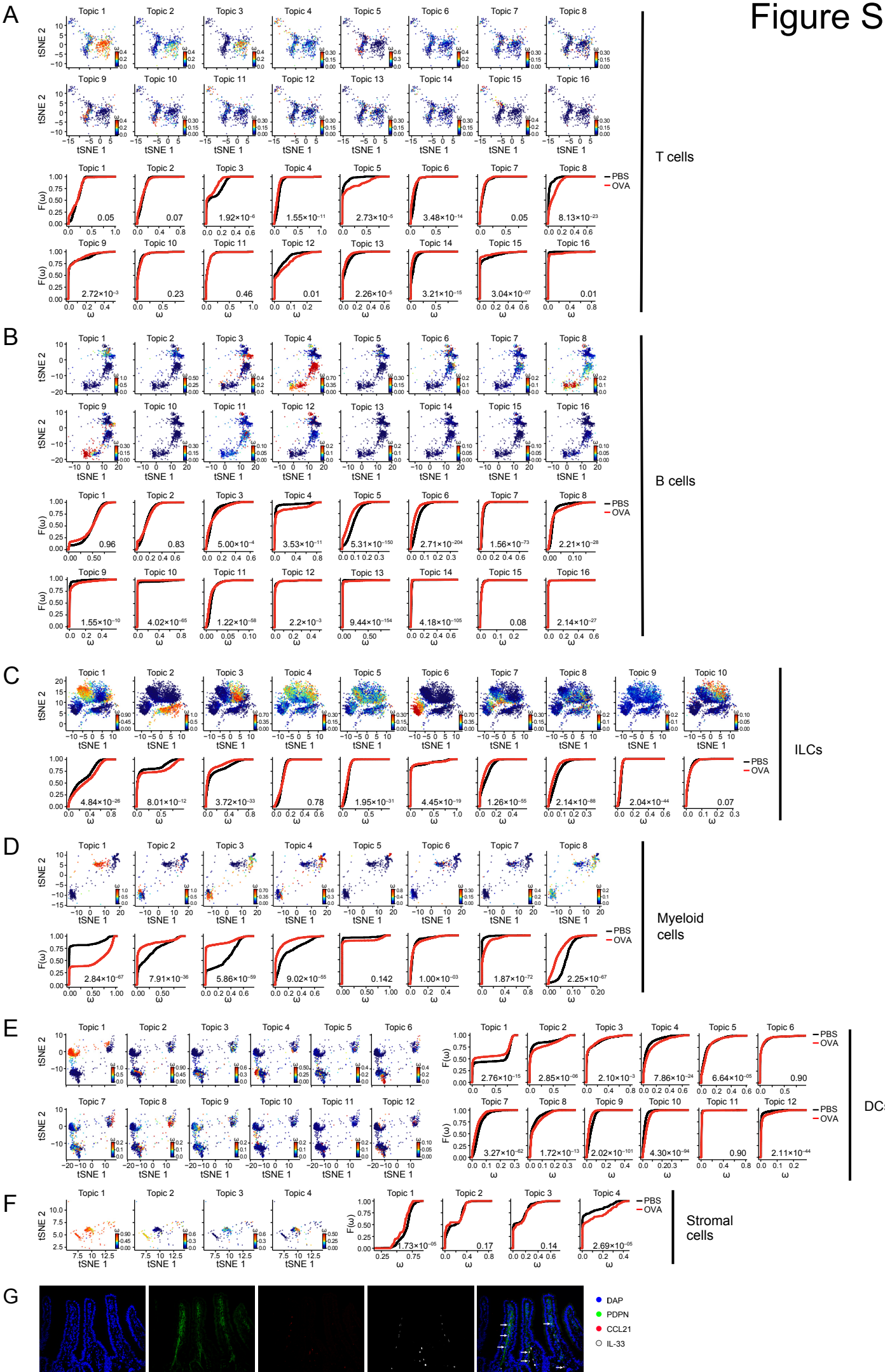
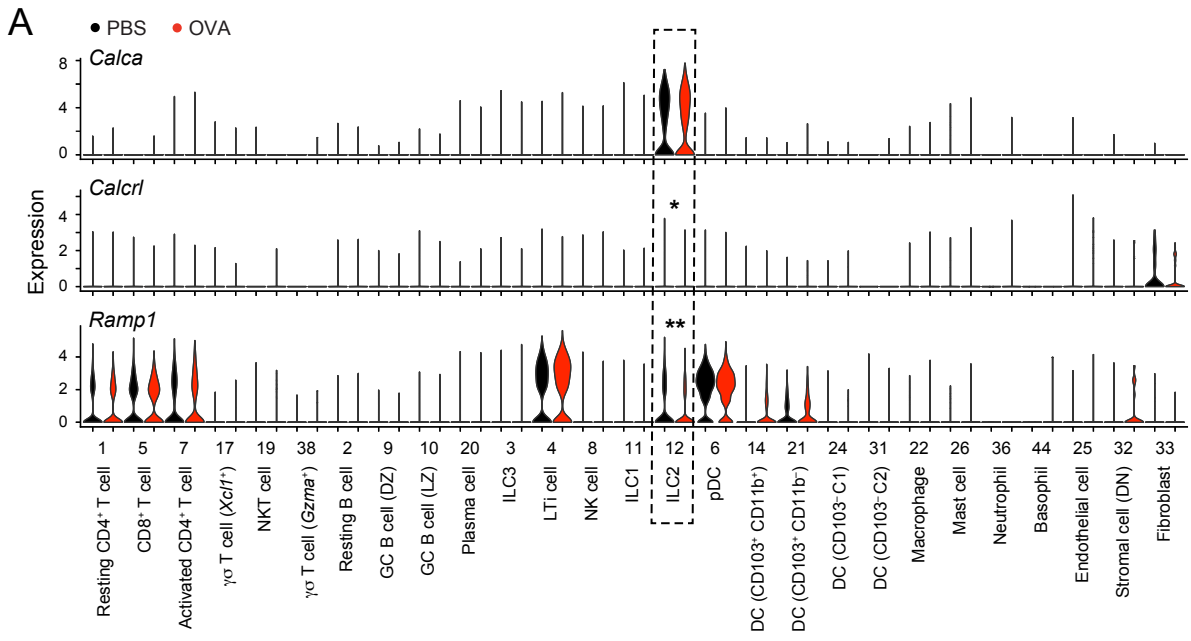

A
Topic 1
Topic 2
Topic 3
Topic 4
Topic 5
Topic 6
Topic 7
Topic 8
Topic 9
Topic 10
Topic 11
Topic 12
Topic 13
Topic 14
Topic 15
Topic 16
tSNE 1
tSNE 2
F(ω)
ω
PBS
OVA
0.05
0.07
1.92×10⁻⁶
1.55×10⁻¹¹
2.73×10⁻⁵
3.48×10⁻¹⁴
0.05
8.13×10⁻²³
2.72×10⁻³
0.23
0.46
0.01
2.26×10⁻⁵
3.21×10⁻¹⁵
3.04×10⁻⁰⁷
0.01
T cells
B
0.96
0.83
5.00×10⁻⁴
3.53×10⁻¹¹
5.31×10⁻¹⁵⁰
2.71×10⁻²⁰⁴
1.56×10⁻⁷³
2.21×10⁻²⁸
1.55×10⁻¹⁰
4.02×10⁻⁶⁵
1.22×10⁻⁵⁸
2.2×10⁻³
9.44×10⁻¹⁵⁴
4.18×10⁻¹⁰⁵
0.08
2.14×10⁻²⁷
B cells
C
Topic 10
4.84×10⁻²⁶
8.01×10⁻¹²
3.72×10⁻³³
0.78
1.95×10⁻³¹
4.45×10⁻¹⁹
1.26×10⁻⁵⁵
2.14×10⁻⁸⁸
2.04×10⁻⁴⁴
0.07
ILCs
D
2.84×10⁻⁶⁷
7.91×10⁻³⁶
5.86×10⁻⁵⁹
9.02×10⁻⁵⁵
0.142
1.00×10⁻⁰³
1.87×10⁻⁷²
2.25×10⁻⁶⁷
Myeloid cells
E
Topic 11
Topic 12
2.76×10⁻¹⁵
2.85×10⁻⁰⁶
2.10×10⁻³
7.86×10⁻²⁴
6.64×10⁻⁰⁵
0.90
3.27×10⁻⁶²
1.72×10⁻¹³
2.02×10⁻¹⁰¹
4.30×10⁻⁹⁴
0.90
2.11×10⁻⁴⁴
DCs
F
1.73×10⁻⁰⁵
0.17
0.14
2.69×10⁻⁰⁵
Stromal cells
G
DAP
PDPN
CCL21
IL-33
50 μm

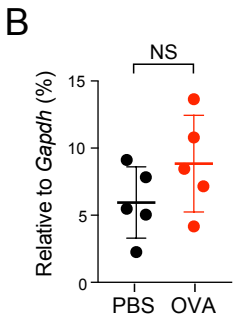
Figure S3. Topic modeling on T cells, B cells, DCs, ILCs, myeloid cells and stromal cells, and co-expression of CCL21 and IL-33 in PDPN$^+$ stromal cells in the small intestine, related to Figure 3

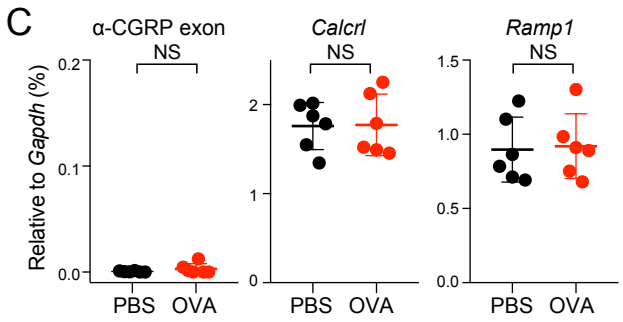
(**A-F**) Biological programs in each cell subset revealed by topic modeling. Shown are topics in T cells (A), B cells (B), ILCs (C), myeloid cells (D), DCs (E) and stromal cells (F). Top (A-D) and left (E and F): a portion of the 2D embedding in **Figure 1B**, only cells from the noted subset cells were shown, colored by the topic's weight in the cell. Bottom (A-D) and right (E and F): empirical cumulative density function (y axis) of topic weights (x axis) for cells from mice treated with PBS (black curve) or OVA (red curve). p values: Mann–Whitney U test.

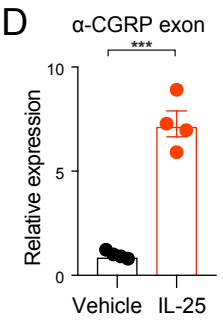
(**G**) co-localization of CCL21 and IL-33 in subsets of PDPN$^+$ stromal cells (arrow) in the small intestines of WT mice. Representative IF images of the small intestines of wild type mice. Scale bars, 50 μm. Data are from seven (A-F) independent experiments or are representative of three independent experiments.

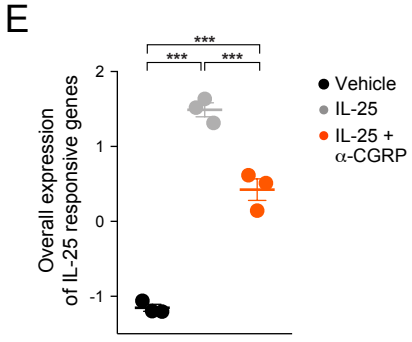
Figure S4


A
PBS
OVA
Calca
Calcrl
Ramp1
Expression
*
**
1 Resting CD4+ T cell
5 CD8+ T cell
7 Activated CD4+ T cell
17 γσ T cell (Xcl1+)
19 NKT cell
38 γσ T cell (Gzma+)
2 Resting B cell
9 GC B cell (DZ)
10 GC B cell (LZ)
20 Plasma cell
3 ILC3
4 LTi cell
8 NK cell
11 ILC1
12 ILC2
6 pDC
14 DC (CD103+ CD11b+)
21 DC (CD103+ CD11b-)
24 DC (CD103- C1)
31 DC (CD103- C2)
22 Macrophage
26 Mast cell
36 Neutrophil
44 Basophil
25 Endothelial cell
32 Stromal cell (DN)
33 Fibroblast


B
Relative to Gapdh (%)
NS
PBS
OVA


C
α-CGRP exon
Calcrl
Ramp1
Relative to Gapdh (%)
NS
PBS
OVA


D
α-CGRP exon
***
Relative expression
Vehicle
IL-25


E
***
Overall expression of IL-25 responsive genes
Vehicle
IL-25
IL-25 + α-CGRP

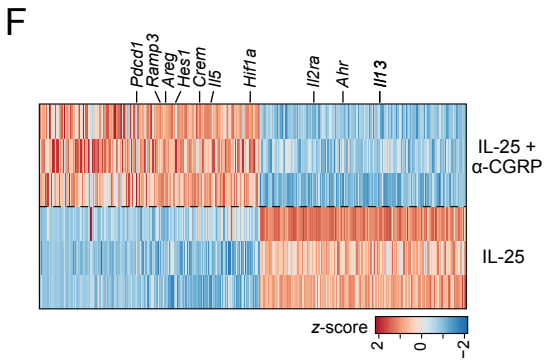

F
Pdcd1
Ramp3
Areg
Hes1
Crem
Il5
Hif1a
Il2ra
Ahr
Il13
IL-25 + α-CGRP
IL-25
z-score

Figure S4. Expression of *Calca*, *Calcrl*, *Ramp1* and *Il5* genes in intestinal KLRG1$^+$ ILC2s in homeostatic and inflammatory conditions, related to Figure 4

(**A**) Distribution of expression amounts (y axis, $\log_2$(TPM+1)) of *Calca* (top), *Calcrl* (middle), *Ramp1* (bottom) in each cell type (*x* axis) in mice treated with PBS (black) or OVA (red) as in **Figure S1A** on day 36. ILC2s are highlighted. *p < 0.05, **p < 2.3×10^{-06}, likelihood ratio test.

(**B**) Expression amounts (y axis, quantitative PCR normalized to *Gapdh*) of CT exon of *Calca* gene in LP ILC2s isolated from PBS or OVA-treated mice as in **Figure S1A** on day 36. Points: individual experiments (n=5); mean and SEM, NS: p > 0.05, *t* test.

(**C**) Expression amount (y axis, quantitative PCR normalized to *Gapdh*) of α-CGRP exon of *Calca*, *Calcrl,* and *Ramp1* in LP ILC2s isolated from control (black) or OVA-treated (red) mice as in **Figure S1A** on day 27. Points: individual experiments (n=6); mean and SEM, NS: p > 0.05, *t* test.

(**D**) The fold change of relative expression (y axis, quantitative PCR normalized to *Gapdh*) of α-CGRP exon in LP ILC2s stimulated with IL-25 or vehicle control for 24 hours *in vitro*. Points: individual experiments (n=4); mean and SEM, ***P < 0.001, *t* test.

(**E**) Overall Expression (OE) scores (**STAR Methods**) of the IL-25-induced genes in **Figure 4C**. Points: individual samples (n=3); mean and SEM, ***FDR < 0.001, *t* test.

(**F**) Expression (color bar, Z score) of genes (columns) significantly induced in LP ILC2s (Fold change ≥ 2, p < 0.05) by α-CGRP compared to control for 3 hours in the presence of IL-25. Key genes are highlighted. mean±SEM, ***p < 0.001, NS: p > 0.05, *t* test (B, C, D, E). Data are from seven (A), five (B), six (C), four (D) independent experiments, or are representative of two (E, F) independent experiments.

Figure S5

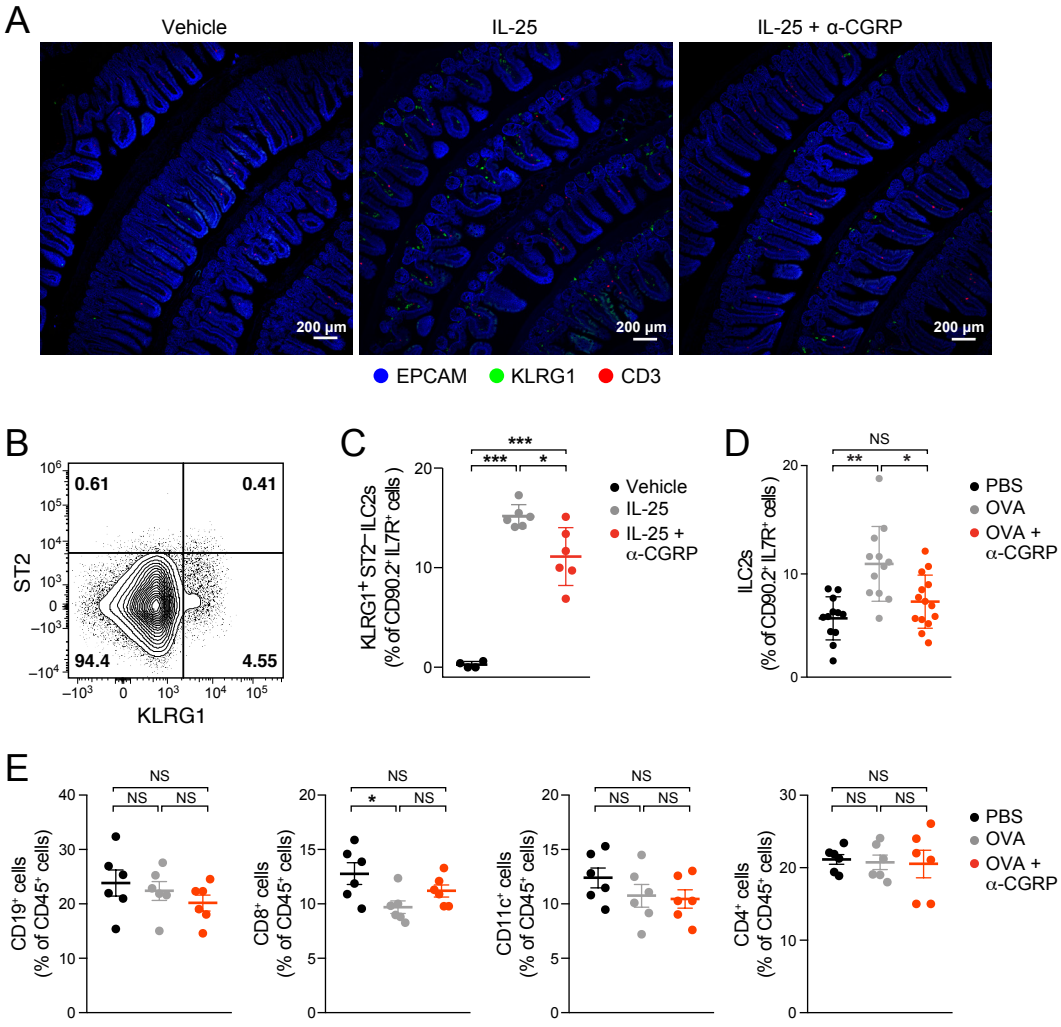

A
Vehicle
IL-25
IL-25 + α-CGRP
200 μm
EPCAM KLRG1 CD3
B
0.61
0.41
94.4
4.55
ST2
KLRG1
C
KLRG1+ ST2− ILC2s (% of CD90.2+ IL7R+ cells)
Vehicle
IL-25
IL-25 + α-CGRP
D
ILC2s (% of CD90.2+ IL7R+ cells)
PBS
OVA
OVA + α-CGRP
E
CD19+ cells (% of CD45+ cells)
CD8+ cells (% of CD45+ cells)
CD11c+ cells (% of CD45+ cells)
CD4+ cells (% of CD45+ cells)
NS

Figure S5. α-CGRP suppress expansion of intestinal KLRG1$^+$ ILC2s *in vivo* but does not affect other major immune cell types, related to Figure 5

(**A**) α-CGRP co-treatment antagonizes CD3$^-$KLRG1$^+$ ILC2 expansion *in vivo*. Representative IF images of CD3$^-$KLRG1$^+$ ILC2 in the small intestines of mice treated as in **Figure 5A**. Scale bars, 200 μm.

(**B**) Flow cytometry analysis of ST2 expression on LP ILCs (gated on CD45$^+$Lin$^-$ CD90.2$^+$IL7R$^+$) isolated from WT mice.

(**C**) Frequency (*y* axis) of KLRG1$^+$ ST2$^-$ cells in total ILCs in mLNs of mice treated as in **Figure 5A**. Points: individual mice (n=6).

(**D**) Frequency (*y* axis) of ILC2s in total ILCs in LP of the small intestines of mice treated as in **Figure 5F** on day 36. Point: individual mice (n=12).

(**E**) Frequency (*y* axis) of CD19$^+$, CD8$^+$, CD11c$^+$ or CD4$^+$ cells in total CD45$^+$ cells in LP of the small intestines of mice treated as in **Figure 5F** on day 36. Point: individual mice (n=6). mean±SEM, *p < 0.05, **p < 0.01, ***p < 0.001, NS: p > 0.05, *t* test (C, D, E). Data are representative of two (A, B) independent experiments, or are from three (C, D) or two (E) independent experiments.

Figure S6

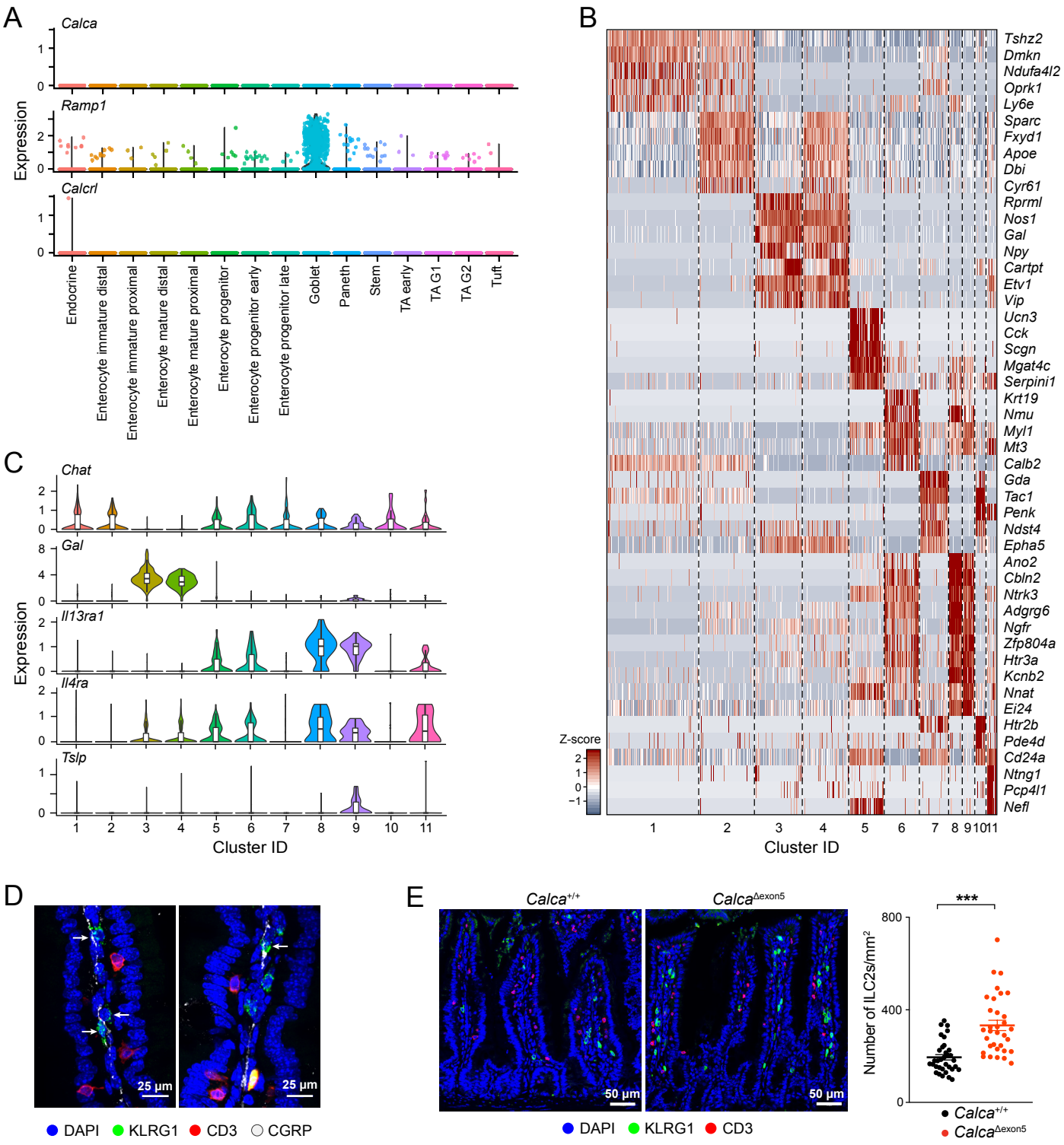

A
Calca
Ramp1
Calcrl
Expression
Endocrine
Enterocyte immature distal
Enterocyte immature proximal
Enterocyte mature distal
Enterocyte mature proximal
Enterocyte progenitor
Enterocyte progenitor early
Enterocyte progenitor late
Goblet
Paneth
Stem
TA early
TA G1
TA G2
Tuft
B
Tshz2
Dmkn
Ndufa4l2
Oprk1
Ly6e
Sparc
Fxyd1
Apoe
Dbi
Cyr61
Rprml
Nos1
Gal
Npy
Cartpt
Etv1
Vip
Ucn3
Cck
Scgn
Mgat4c
Serpini1
Krt19
Nmu
Myl1
Mt3
Calb2
Gda
Tac1
Penk
Ndst4
Epha5
Ano2
Cbln2
Ntrk3
Adgrg6
Ngfr
Zfp804a
Htr3a
Kcnb2
Nnat
Ei24
Htr2b
Pde4d
Cd24a
Ntng1
Pcp4l1
Nefl
Z-score
Cluster ID
C
Chat
Gal
Il13ra1
Il4ra
Tslp
Expression
Cluster ID
D
25 μm
DAPI KLRG1 CD3 CGRP
E
Calca+/+
CalcaΔexon5
50 μm
DAPI KLRG1 CD3
***
Number of ILC2s/mm2
Calca+/+
CalcaΔexon5

Figure S6. scRNA-seq analysis of intestinal epithelium and enteric neurons, ATAC-seq analysis of intestinal ILC2s and immunofluorescence staining analysis of the small intestine of *Calca*$^{\Delta exon5}$ mice, related to Figure 6

(**A**) Undetectable expression of *Calca* and *Calcrl* in epithelium of wild type mice (Haber et al, 2017). Distribution of expression amounts (y axis, log_2(TPM+1)) of *Calca* (top), *Ramp1* (middle), *Calcrl* (bottom) in each epithelial cell type as labeled.

(**B**) Marker genes of each enteric neuron clusters. Heatmap showing relative expression (Z score of log_2(TPM+1)) of top 5 marker genes (row) of each cluster (column) in **Figure 6A**.

(**C**) Distribution of expression amounts (y axis, log_2(TPM+1)) of *Chat*, *Gal*, *Il13ra1*, *Il4ra* and *Tslp* gene in each cluster (*x* axis) in **Figure 6A.**

(**D**) Interaction between ChAT-expressing neuron fibers and CD3$^-$KLRG1$^+$ ILC2s (arrow) in the small intestines of WT mice. Representative IF images of the small intestines of wild type mice. Scale bar, 25 μm.

(**E**) α-CGRP deficiency affects ILC2 expansion in the inflammatory condition *in vivo*. Left: representative IF images of ILC2s (KLRG1$^+$CD3$^-$) in the small intestine of WT or *Calca*$^{\Delta exon5}$ mice challenged with intraperitoneal injection of IL-25 for 48 hours. Scale bars, 50 μm. Right: density of ILC2s (y axis, number per mm^2) in WT and *Calca*$^{\Delta exon5}$ mice. Points: individual section (n=33 from 4 mice). mean and SEM, ***p < 0.001, Student's *t* test. Data are two (D) independent experiments or representative of three mice (D).